

Single Atom Spin Qubits in Silicon

Jarryd James Pla



UNSW
AUSTRALIA

A thesis submitted in fulfilment of the requirements for the degree
Doctor of Philosophy

April 5, 2013

Typeset by L^AT_EX using the SRSTHESIS class
Copyright © Jarryd James Pla 2013 and
The University of New South Wales

Originality Statement

'I hereby declare that this submission is my own work and to the best of my knowledge it contains no materials previously published or written by another person, or substantial proportions of material which have been accepted for the award of any other degree or diploma at UNSW or any other educational institution, except where due acknowledgement is made in the thesis. Any contribution made to the research by others, with whom I have worked at UNSW or elsewhere, is explicitly acknowledged in the thesis. I also declare that the intellectual content of this thesis is the product of my own work, except to the extent that assistance from others in the project's design and conception or in style, presentation and linguistic expression is acknowledged.'

A handwritten signature in black ink, appearing to be a stylized 'R' or a similar character.

Signed

Date 05/04/2013

Abstract

Spin is a quantum mechanical property that describes the magnetic orientation of elementary and composite particles such as electrons and nuclei. For “spin-half” particles placed in a magnetic field, two states with differing energies are defined. Proposals exist for developing a revolutionary kind of computer that encodes bits of information on the states of a simple quantum two-level system – like those of a spin in a magnetic field. These “quantum computers” exploit the fundamental principles of quantum mechanics in order to perform certain calculations exponentially faster than their classical counterparts. Key to the development of such a device is the identification of potential systems that are suitable for employment as a quantum bit (qubit).

This thesis explores quantum bits constructed from the spin states of single atoms hosted in silicon semiconductor devices. Silicon (Si) is an exceptional platform for spin-based quantum computing – in addition to being the dominant material in the microelectronic industry, it is also predominantly composed of nuclear spin-zero isotopes, providing very little background magnetic disturbance. The donor-atom phosphorus (^{31}P) is investigated here. It possesses a nucleus that binds an additional electron to its positive charge, providing two distinct spin qubits.

Here, several world-first experimental milestones in spin-based quantum information processing are reported. First, the readout of the electron spin is demonstrated in single-shot, using a silicon device which combines implanted phosphorus donors with a sensitive nanoscale electrometer. Then, the electron spin is coherently operated as a qubit by delivering on-chip microwave excitations. Combining the electron spin detection and control capabilities enables a quantum non-demolition measurement of the single ^{31}P nuclear spin. Experiments yield exceptional nuclear readout fidelities – the highest for any solid-state qubit. Through an application of nuclear magnetic resonance, high-fidelity quantum control of the nuclear spin qubit is demonstrated. Finally, a single spin-bearing silicon nucleus (^{29}Si) coupled to the electron spin is detected in single-shot and operated as a qubit.

These results, along with the clear pathways identified for improving device performance, illustrate that single-atom electron and nuclear spin qubits in silicon

constitute an excellent basis on which to construct a quantum computer.

Acknowledgements

It seems like only yesterday that I was sitting in a lecture hall, listening to an extremely enthusiastic lecturer speak of the wondrous possibilities that Quantum Mechanics brings to the world of modern electronics. At the start of the course I would never have dreamed of pursuing a PhD in such a field, and by the end of it I was sure I would. Working at the Centre for Quantum Computation and Communication Technology over the past four years has been an incredible experience. Not only have I met some extraordinary people, but I have also been exposed to some amazing research. I feel humbled to have been a part of the ambitious and exciting donor qubit project within the Centre. To the enthusiastic young lecturer, now my supervisor Andrea Morello, thank you. Thank you for entrusting me with such a crucial part of this project for my PhD. Thank you for your “hands-on” approach in showing me the workings of a low-temperature laboratory. Thank you for the countless hours spent reading and editing papers and for creating an environment that fostered our invigorating discussions on both physics and non-physics related topics. I’m not sure which I found more interesting. Not least of all, thank you for your positive outlook and infectious optimism – some of which may just have managed to rub off on me. To my co-supervisor Andrew Dzurak, thank you for your efforts in polishing off the manuscripts, for your over-the-top reactions to exciting new results and for taking me to fancy wine bars and restaurants that I could certainly not afford on my own.

None of this work would have been possible without the tiring efforts of my fellow PhD’s and postdoctoral researchers. Kuan Yen-Tan, Wee-Han Lim, Kok-Wai Chan and Nai-Shyan Lai, or in short, the “fab four” – you all have my greatest respect and gratitude for the many hours spent fabricating such beautiful devices, and for teaching me the clean room basics. To Floris Zwanenburg, thank you for taking me under your wing and demonstrating to me the art of quantum transport. I enjoyed our tag-team shifts in the lab and our daily coffee gossip sessions. John Morton, I am extremely fortunate for having had the opportunity to perform some of these measurements with you. What we achieved together in the lab over that short period of time was amazing. Thank you for the spin resonance knowledge that you passed on during those late night measurement

sessions. To the members of the Quantum Spin Control group: Juan Pablo, Fahd Mohiyaddin, Rachpon Kalra, Arne Laucht, Sol Freer and Juha Muhonen, thank you. I relished all of the discussing, explaining, listening and laughing that went on during my time. It was a pleasure working with you all, and I wish you the best of success in the years to come. My sincerest thanks goes to Bob Starrett and Dave Barber for sharing their vast expertise in electronics and cryogenics, your contributions to my work were invaluable. Bob, I hope you are thoroughly enjoying your well-earned retirement.

Finally, to my family and friends, thank you. Thank you Steve for carrying far more than your fair share when I was M.I.A. in the lab for days on end. I am forever grateful for your patience and strength. To my parents, thank you for always being there for me, despite being so far away. Your constant love and support has been a great source of comfort.

To all my loved ones.

Publications

Peer reviewed journal articles

Morello, A., **Pla, J. J.**, Zwanenburg, F. A., Chan, K. W., Tan, K. Y., Dehollain, J. P., Huebl, Möttönen, M., Nugroho, C. D., Yang, C., van Donkelaar, J. A., Alves, A. D. C., Jamieson, D. N., Escott, C. C., Hollenberg, L. C. L., Clark, R. G. and Dzurak, A. S. *Nature* **467**, 687-691 (2010).

Pla, J. J., Tan, K. Y., Dehollain, J. P., Lim, W. H., Morton, J. J. L., Jamieson, D. N., Dzurak, A. S. and Morello, A. *Nature* **489**, 541-545 (2012).

Dehollain, J. P., **Pla, J. J.**, Siew, E., Tan, K. Y., Dzurak, A. S. and Morello, A. *Nanotechnology* **24**, 015202 (2013).

Pla, J. J., Tan, K. Y., Dehollain, J. P., Lim, W. H., Morton, J. J. L., Zwanenburg, F. A., Jamieson, D. N., Dzurak, A. S. and Morello, A. *Nature*, in the press (2013).

Mohiyaddin, F. A., Rahman, R., Kalra, R., Klimeck, G., Hollenberg, L. C. L., **Pla, J. J.**, Dzurak, A. S. and Morello, A. *Nano Letters*, in the press (2013).

Selected conference presentations

J. J. Pla, A. Morello, F. A. Zwanenburg, K. W. Chan, C. Yang, J. A. van Donkelaar, D. N. Jamieson and A. S. Dzurak, *Single-shot readout of an electron spin in silicon*, presented at International Conference On Nanoscience and Nanotechnology, Sydney (NSW), Australia, February 2010 (Contributed Talk).

J. J. Pla, A. Morello, F. A. Zwanenburg, K. W. Chan, H. Huebl, M. Mottonen, C. D. Nugroho, C. Yang, J. A. van Donkelaar, A. Alves, D. N. Jamieson, C. C. Escott, L. C. L. Hollenberg, R. G. Clark and A. S. Dzurak, *Single-shot readout of an electron spin in silicon*, presented at International Conference on Quantum Communication, Measurement and Computation, Brisbane (QLD), Australia, July 2010 (Contributed Talk).

J. J. Pla, K. Y. Tan, F. A. Zwanenburg, J. P. Dehollain, C. Yang, D. N. Jamieson, A. Morello, and A. S. Dzurak, *Microwave control of a single elec-*

tron spin in silicon, presented at International Workshop on Silicon Quantum Electronics, Albuquerque (NM), USA, August 2010 (Poster).

J. J. Pla, K. Y. Tan, F. A. Zwanenburg, C. Yang, D. N. Jamieson, A. Morello, and A. S. Dzurak, *Microwave control of a single electron spin in silicon*, presented at 19th Australian Institute of Physics Congress, Melbourne (VIC), Australia, December 2010 (Poster).

J. J. Pla, K. Y. Tan, J. P. Dehollain, J. J. L. Morton, W. H. Lim, C. Yang, D. N. Jamieson, A. S. Dzurak and A. Morello, *Coherent control of electron and nuclear ^{31}P spin qubits in silicon*, presented at International Workshop on Silicon Quantum Electronics, Denver (CO), USA, August 2011 (Contributed Talk).

J. J. Pla, K. Y. Tan, J. P. Dehollain, J. J. L. Morton, W. H. Lim, C. Yang, D. N. Jamieson, A. S. Dzurak and A. Morello, *Coherent control of electron and nuclear ^{31}P spin qubits in silicon*, presented at International Conference on Quantum Information Processing and Communication, Zurich, Switzerland, September 2011 (Poster).

J. J. Pla, K. Y. Tan, J. P. Dehollain, J. J. L. Morton, W. H. Lim, C. Yang, D. N. Jamieson, A. S. Dzurak and A. Morello, *Coherent control of single ^{31}P and ^{29}Si nuclear spins in silicon*, presented at International Workshop on Silicon Quantum Electronics, Sydney (NSW), Australia, February 2012 (Contributed Talk).

J. J. Pla, K. Y. Tan, J. P. Dehollain, J. J. L. Morton, W. H. Lim, D. N. Jamieson, A. S. Dzurak and A. Morello, *EPR and NMR on a single atom in silicon*, presented at 54th Rocky Mountain Conference on Analytical Chemistry, Copper Mountain (CO), USA, July 2012 (Invited Talk).

J. J. Pla, K. Y. Tan, J. P. Dehollain, J. J. L. Morton, W. H. Lim, D. N. Jamieson, A. S. Dzurak and A. Morello, *A high-fidelity nuclear spin qubit in silicon*, presented at 20th Australian Institute of Physics Congress, Sydney (NSW), Australia, December 2012 (Contributed Talk).

Awards

- ★ UNSW IEEE Technologies of the Future Competition Winner (2009).

- ★ UNSW IEEE Technologies of the Future Competition Winner (2010).
- ★ UNSW Engineering Deans Award for Excellence in Postgraduate Research (2011).
- ★ Canon Information Systems Research Australia (CiSRA) Best Research Paper Award (2012).

Abbreviations

0D	Zero-dimensional
1D	One-dimensional
2D	Two-dimensional
3D	Three-dimensional
2DEG	Two-dimensional electron gas
AC	Alternating current
Al	Aluminium
AWG	Arbitrary waveform generator
BJT	Bipolar junction transistor
CI	Constant-interaction
CMOS	Complementary metal-oxide-semiconductor
CP	Carr Purcell
CPMG	Carr Purcell Meiboom Gill
CW	Continuous wave
DAC	Digital-to-analogue converter
DC	Direct current
DOS	Density of states
EBL	Electron beam lithography
EPR	Electron paramagnetic resonance
ESR	Electron spin resonance
FFT	Fast Fourier transform
FET	Field effect transistor
FWHM	Full-width at half-maximum
GaAs	Gallium arsenide
LED	Light-emitting diode
LNN	Linear nearest neighbor
MOS	Metal-oxide-semiconductor
MOSFET	Metal-oxide-semiconductor field effect transistor
NEMO	Nano electronic modeling
NMR	Nuclear magnetic resonance

NV	Nitrogen-vacancy
P	Phosphorus
PMMA	Polymethyl-methacrylate
Q1D	Quasi-one-dimensional
QEC	Quantum error correction
QED	Quantum electrodynamics
QIP	Quantum information processing
QND	Quantum non-demolition
RF	Radio-frequency
RSA	Ron Rivest, Adi Shamir and Len Adleman (encryption algorithm)
RTS	Random-telegraph-signal
SEM	Scanning electron microscope
SET	Single-electron transistor
Si	Silicon
SiO₂	Silicon dioxide
SMU	Source-measure unit
SNF	Semiconductor Nanofabrication Facility
SOI	Spin-orbit interaction
SRS	Stanford Research Systems
UNSW	University of New South Wales

Contents

Abstract	i
Acknowledgements	iii
Publications	vii
Abbreviations	xi
1 Introduction and Motivation	7
1.1 Quantum Computing	8
1.2 Spins for Quantum Computing	13
1.3 Kane Quantum Computer	17
1.3.1 A Quasi-2D Architecture	20
1.3.2 Si:P Qubit Physical Implementation	23
1.4 The Si:P Physical System	24
1.5 Thesis Outine	28
2 Experimental Methods	31
2.1 Device Fabrication	32
2.2 Measurement Setup	35
2.3 Single-Electron Transistor	38
2.3.1 Operating Principles	38
2.3.2 Si MOS SET	42
2.3.3 Measurement of SET Charge Sensitivity	42
2.4 Microwave Transmission Line	45
3 Electron Spin Readout	49
3.1 Introduction	50
3.2 Device Architecture	50
3.3 Charge Stability Diagram	52
3.4 Ion-Implantation	54
3.5 Features of the Charge Stability Diagrams	56
3.6 Definition and Properties of Special Device Bias Points	57
3.7 Donor-SET Resonant Tunneling Features	61
3.8 Single-Shot Spin Readout	65
3.9 Electron Temperature	74

3.10	Electron Spin Relaxation	75
3.11	Electron Spin Readout Fidelity	85
3.12	Suggestions for Future Device Improvements	88
3.13	Conclusion	89
4	Electron Spin Qubit	91
4.1	Introduction	92
4.2	Electron Spin Resonance	92
4.3	Electron Spin Rabi Oscillations	96
4.4	Simulation of Rabi Oscillations	100
4.5	Electron Spin Coherence	104
4.5.1	Phase Cycling	107
4.6	Electron Spin Qubit Fidelity	108
4.6.1	Measurement Fidelity	108
4.6.2	Initialization Fidelity	113
4.6.3	Control Fidelity	114
4.7	Conclusion	116
5	^{31}P Nuclear Spin Qubit	119
5.1	Introduction	120
5.2	Electrical Single-Shot Nuclear Spin Readout	121
5.3	Quantum Jumps of the Nuclear Spin State	125
5.4	Error Bars in the Nuclear Spin Flip Rates	128
5.5	Nuclear Spin-Up Flip Mechanisms	129
5.5.1	Isotropic Hyperfine Coupling	131
5.5.2	Anisotropic Hyperfine Coupling	135
5.6	Single-Spin Nuclear Magnetic Resonance	138
5.7	Calculation of the Electron g -Factor	140
5.8	Coherent Control: Rabi Oscillations	143
5.9	Nuclear Spin Qubit Coherence: Ramsey Fringes and Hahn Echo .	144
5.10	Qubit Readout and Control Fidelities	147
5.10.1	Nuclear Spin Readout Fidelity	147
5.10.2	Nuclear Spin Control Fidelity	148
5.11	Conclusion	151
6	^{29}Si Nuclear Spin Qubit	153
6.1	Introduction	154
6.2	Power Dependence of the Electron Spin Resonance Signal	155
6.3	Single-Shot Readout of a ^{29}Si Nuclear Spin	157
6.4	^{29}Si Spin Control: Nuclear Magnetic Resonance and Coherence Measurements	159
6.5	Single ^{29}Si Nuclear Spin Metrology	165

CONTENTS

6.6	Conclusion	167
7	Conclusion and Future Work	169
7.1	Summary of Achievements	170
7.2	Chapter 3 - Electron Spin Readout	170
7.3	Chapter 4 - Electron Spin Qubit	171
7.4	Chapter 5 - ^{31}P Nuclear Spin Qubit	171
7.5	Chapter 6 - ^{29}Si Nuclear Spin Qubit	172
7.6	Future Work and Outlook	173
	References	177

CONTENTS

List of Figures

1.1	Computational elements of modern-day classical computers	9
1.2	Different classes of solid-state spin qubits	14
1.3	Architectures for quantum computing with ^{31}P donors in silicon .	17
1.4	CTAP chain, pulse sequence and state evolution	22
1.5	Eigenstates and spin transitions of a single ^{31}P donor in Si	24
2.1	SEM micrographs and cross-section sketch of the Si:P qubit device	33
2.2	Wiring and equipment for qubit measurements	34
2.3	The general construction and operation of a single-electron transistor	38
2.4	SET bias spectroscopy	41
2.5	Charge sensitivity measurement of the Si MOS SET	43
2.6	Sketch of the broadband transmission line	45
2.7	SET response to the transmission line	47
3.1	Electron spin readout device and charge stability diagram	51
3.2	Charge stability diagrams for devices with different ion implantation fluences	54
3.3	Modulation of the Coulomb peak current with SET electron occupation number	55
3.4	Close-up of a charge transition and electrochemical potential diagrams	58
3.5	Tunnel rate measurements	62
3.6	Readout non-idealities	64
3.7	Single-shot electron spin readout experiment	67
3.8	Three level pulse experiment with variable load voltage	70
3.9	Four-level pulsing sequence for deterministic loading of the spin-down state and accurate extraction of the Zeeman splitting	72
3.10	Electron temperature and lever arm calibration	73
3.11	Single-shot vs. averaged spin lifetime (T_1) measurements	75
3.12	Spin relaxation rate magnetic field dependence	77
3.13	Electron spin flip-flop mechanism	82
3.14	Readout fidelity and visibility	84
3.15	Calculation of the peak current distributions	86

LIST OF FIGURES

4.1	Qubit device and pulsing scheme	93
4.2	ESR spectra	95
4.3	Rabi oscillation	98
4.4	Rabi oscillations and power dependence of the Rabi frequency . .	99
4.5	Rabi simulation model – measurement and thermal effects . . .	104
4.6	Coherence time and dynamical decoupling	105
4.7	Measurement fidelity analysis	109
4.8	Qubit fidelity analysis	111
4.9	Pulse error analysis	114
5.1	Qubit nanostructure and spin transitions	122
5.2	Nuclear spin quantum jumps, lifetimes and readout error	126
5.3	Pulse protocol for the modified quantum jumps measurement . .	127
5.4	Nuclear spin-up and spin-down flip time histograms	130
5.5	Donor ionization time dependence and neutral donor eigenstate probability evolution	132
5.6	Magnetic field angles for ionized and neutral donor	135
5.7	Nuclear magnetic resonance of a single ^{31}P nucleus	139
5.8	Rabi oscillations of a single ^{31}P nuclear spin	142
5.9	Ramsey fringes and spin echo decay	145
5.10	Coherence measurements for extracting the rotation angle error .	149
6.1	ESR peak at the ν_{e2} transition and its corresponding power dependence	156
6.2	ESR peak splitting at low microwave excitation powers	157
6.3	Quantum jumps of a single ^{29}Si nuclear spin	158
6.4	NMR experiment on a ^{29}Si nuclear spin	162
6.5	Single ^{29}Si nuclear spin Rabi oscillations	163
6.6	Ramsey fringes and Hahn echo decay for the ionized donor ^{29}Si nuclear spin	164
6.7	Possible lattice sites for the single ^{29}Si atom	166

Chapter 1

Introduction and Motivation

“Science is built up of facts, as a house is built of stones; but an accumulation of facts is no more a science than a heap of stones is a house.”

Henri Poincaré

1.1 Quantum Computing

Silicon microelectronics underpins the entire information age. From smart-phones to televisions to the latest in computing, the continued development of this technology is producing devices with applications once confined to the realms of science-fiction. The birth of solid-state electronics stems back over half a century, with the demonstration of a device [1] (now known as the point-contact transistor) that used electrical signals to control the flow of current through a block of doped germanium. It wasn't long before silicon emerged as the dominant semiconductor material for transistor technologies, due to its electrical, thermal and mechanical properties and because of the ease with which it could be oxidized. The real basis for modern silicon microelectronics came with the invention of the bipolar junction transistor (BJT) in 1948, and the subsequent development of the metal-oxide-semiconductor field effect transistor (MOSFET) in the years between 1955 and 1960 [2, 3]. Today, consumer grade microprocessors can contain in excess of 1.4 billion MOSFETs, with Intel currently manufacturing chips exhibiting transistor feature sizes at the 22 nm node [4] (see Figs. 1.1a,b). These transistors are used to form the bits of a computer – carriers of information that can exist in one of two states (labeled 1 or 0), represented by voltage and current signals. Calculations are performed sequentially by passing the bits (in the form of electrical signals) through logic gates (Fig. 1.1c) that reside inside the computers arithmetic logic unit.

Almost four decades ago, a major figure behind the development of the semiconductor industry and co-founder of Intel, Gordon Moore, made a prediction about the scaling of resources on silicon chips that has remarkably held true up to the present day. He suggested that the number of transistors on a single wafer

1.1. Quantum Computing

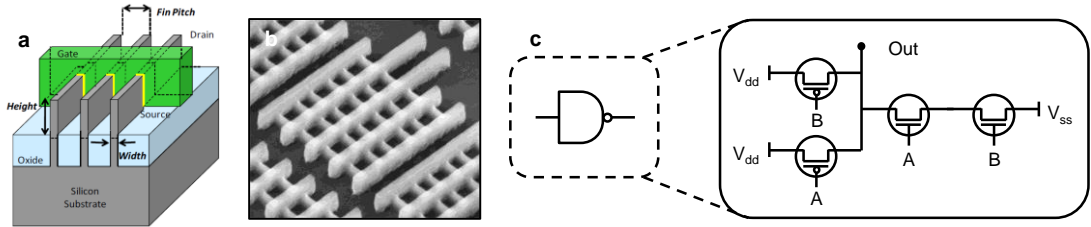


Figure 1.1: Computational elements of modern-day classical computers. **a**, Current generation 22 nm node FinFETs pioneered by Intel, figure taken from [4]. The fin width is ~ 8 nm, with a height of 34 nm and a pitch of 60 nm. **b**, Scanning electron microscope (SEM) micrograph of a FinFET device [4]. **c**, NAND logic gate and its internal MOSFET construct.

would double approximately every two years [5]. Whilst the constant demands of smaller devices and faster processing speeds have driven engineers to adhere to this law by rapidly shrinking transistor dimensions, this trend can clearly not continue indefinitely. An essential ingredient in MOSFET design is the dopant atoms that are introduced to give the silicon its electrical transport characteristics – the doping of silicon chips with impurity atoms (e.g. phosphorus) is a standard technique employed by the multi-trillion dollar microelectronics industry [6]. However, with gate dimensions expected to shrink below 5 nm beyond 2020, it is unclear what will happen once the feature sizes reach the dimensions of single donors (the Bohr radius of a phosphorus donor in silicon is ~ 2.5 nm). It is expected that classical laws will no longer strictly apply and quantum mechanical effects such as tunneling will need to be considered. In addition, device performance could be significantly affected by the behavior and placement of individual dopant atoms [7]. For conventional (classical) microelectronics, this is considered a major hindrance, as it results in irreproducible characteristics of the bits in a microprocessor chip.

We can take advantage of the technological advances that allow us to create

these ultra-small devices en masse, in order to develop a new kind of computational machine which exploits the laws of Quantum Mechanics. The fundamental unit of such a “quantum computer” – the quantum bit, or qubit – can theoretically be constructed from any general two level quantum system, which possesses two states $|0$ and $|1$ that are well separated in energy from any other state in the system. These states are the equivalent of the 1’s and 0’s in a conventional computer. There are, however, very important differences between a classical bit of information and a quantum bit, that arise as a result of quantum mechanics and allow quantum computers to perform certain tasks exponentially faster than their classical counterparts. Qubits can exist in superposition states, i.e. $|\Psi\rangle = \alpha|1\rangle + \beta|0\rangle$, where α and β are complex numbers and $|\alpha|^2 + |\beta|^2 = 1$, and two qubits (A and B) can be entangled [8] to form states with no classical analog. The Bell state $|\Phi^+\rangle = \frac{1}{\sqrt{2}}(|0\rangle_A \otimes |0\rangle_B + |1\rangle_A \otimes |1\rangle_B)$ (where \otimes is the tensor product) is an example of a maximally entangled state, where the individual qubit states are inseparable (although the physical qubits themselves are spatially separable), and measurement of one qubit instantaneously collapses the other. It is thought that entanglement is the resource which enables the exceptional power of a quantum computer. However, there do exist theoretical proposals [9, 10] and experimental demonstrations [11] of quantum algorithms which achieve exponential speedup over classical approaches that employ non-classical correlations between qubits other than entanglement. The challenge with a quantum bit is to maintain “coherent” superposition states, where the phase relationship between the complex coefficients above, $\alpha = |\alpha| e^{i\phi_1}$ and $\beta = |\beta| e^{i\phi_2}$, is known precisely over time. Decoherence is the process where this phase information is corrupted by environmental noise. The time over which the qubit is said to remain coherent

1.1. Quantum Computing

is characterized by the parameter T_2 . Decoherence is one of the most significant hurdles facing large-scale quantum computing and the demonstration of complex quantum algorithms.

The most widely recognized and celebrated quantum algorithm to date is known as Shor's algorithm [12]. It is capable of factoring a large composite number into its prime constituents, using a number of steps that grows only polynomially with the number of bits. A quantum computer could therefore decipher the RSA algorithm used in public key cryptography, something with obvious implications for data security. Other notable applications of a quantum computer include solving large systems of linear equations [13] (an ability crucial to a wide variety of problems in signal processing, systems theory, economics and statistics) and searching databases of unsorted data [14]. However, one of the most important applications may come in the form of simulations. Quantum computers are inherently good at simulating other quantum systems [15]. Representing the state of a system of n interacting two-level quantum particles on a classical machine would require a memory space large enough to hold 2^n numbers. For a system of $n = 300$ particles this requires $2^{300} \approx 10^{90}$ numbers – a figure larger than total number of estimated atoms in the observable universe. Furthermore, to calculate their time evolution, one would need to solve the exponential of a $2^{300} \times 2^{300}$ matrix, a task which is safe to say impossible on any classical computer. A quantum computer or simulator would require only n quantum bits evolving for a time proportional to that of the problem being investigated. Quantum simulators could be used to calculate the properties of molecules from first-principles [16] allowing the design of new chemicals and materials. The way drugs interact with proteins could also be accurately modeled using quantum mechanics [17] rendering computer-aided

drug design a possibility. With only 30 to 40 qubits, problems can already be solved that are too difficult using conventional techniques [15].

The implementation of quantum algorithms and simulators requires a platform capable of sustaining large numbers of interacting qubits. Finding such a platform is a daunting task, as one typically needs to balance the requirement of scalability with the need to preserve quantum information [18]. There are a plethora of physical systems that have been utilized as quantum bits. These include more exotic ideas such as floating electrons on liquid helium [19], computing with molecular magnets [20] and nuclear magnetic resonance (NMR) on ensembles of molecules in a test tube [21]. To date, the largest quantum computers have been built from ions cooled with lasers and suspended in electromagnetic traps in near-perfect vacuums [22], where quantum computers with 14 entangled qubits [23] and simulators with up to 300 qubits [24] have been demonstrated. It is desirable to develop quantum computing architectures that are based on solid-state technologies (such as semiconductor chips), as there are clearer pathways to achieve system scale-up. In the way of solid-state implementations, there are three primary categories or “flavors” of qubit: superconducting, charge and spin. Not all solid-state qubits fit into these labels, such as those based on orbital states [25] or valley states in silicon [26], however, qubits in these categories have attracted the lion’s share of attention over the past few decades. Superconducting qubits [27, 28] are quantum mechanical electronic circuits, which are fabricated on insulating substrates. The qubits, which are based on superconducting metallic structures, can be broken further down into the sub-categories of charge [29], phase [30] and flux [31] (or hybrids thereof [32, 33]). They employ dissipationless units of non-linear inductance called Josephson Junctions, through which Cooper

pairs of electrons tunnel. These superconducting qubits can be integrated with superconducting circuit cavities to perform quantum electrodynamics (QED) on a chip (circuit QED) [34], which has facilitated the coupling of multiple superconducting qubits [35] as well as permitted their interaction with other quantum systems [36]. The second type of solid-state qubit, which is based on charge states of quantum dots [37] or donors [38, 39], is attractive because of the relative ease with which the system can be tuned and operated. Furthermore, the strong charge to electric field coupling enables very fast control, where sub-nanosecond gate times are routine in such experiments. This dissertation focuses on the third type of qubit – that based on the spin degree of freedom [40], which is the topic of the proceeding section.

1.2 Spins for Quantum Computing

Spin is a quantum mechanical property of electrons, protons and neutrons which gives rise to a magnetic moment, $-g_e\mu_BS$ for electrons and $g_n\mu_NI$ for nuclei. Here we define $g_{e(n)}$ as the electron (nuclear) g -factor, $\mu_{B(N)}$ the Bohr (nuclear) magneton and $S(I)$ the electron (nuclear) spin. The magnetic moment of unpaired electron spins in solids is responsible for a vast range of interesting and fundamental phenomenon including paramagnetism and ferromagnetism. An entire field of research has emerged from the study of spins in solids, known as spintronics, that is aimed at controlling electron and nuclear spins in semiconductors and metals in order to create new spin-based multifunctional devices such as the spin-FET (field effect transistor), spin-LED (light-emitting diode) and novel memories [46]. In addition to spintronics, spins also possess great potential for

1. Introduction and Motivation

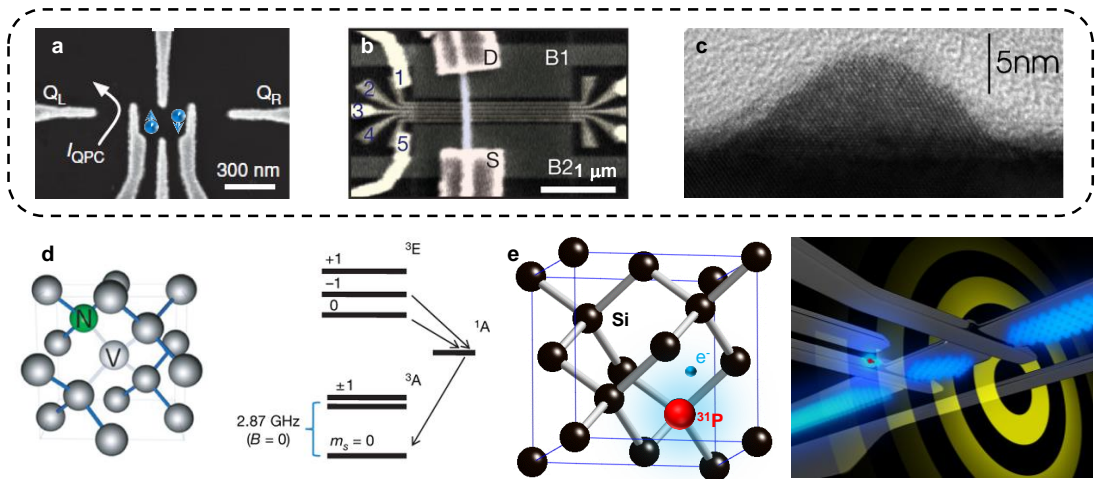


Figure 1.2: Different classes of solid-state spin qubits. **a-c**, Examples of spin qubit systems. Popular among this type is the lithographically-defined quantum dot (**a**), figure adapted from [41], where single electrons can be confined in electrostatic potentials by applying voltages to electrodes on semiconductor substrates. The nanowire quantum dots (**b**), figure taken from [42], have similar operating principles to the lithographically defined dots but make use of the natural confinement provided by the reduced dimensions of the wire to isolate single electrons. Artificial atoms may also be constructed by taking advantage of the strain relaxation in semiconductors made from materials with different lattice constants, where dots “self assemble” (**c**), figure from [43]. **d**, Left: The nitrogen-vacancy defect center in diamond. Right: Its corresponding spin triplet ground (${}^3\text{A}$), first excited (${}^3\text{E}$) triplet and metastable singlet (${}^1\text{A}$) state energy levels (right), figure taken from [44]. **e**, Left: The substitutional donor phosphorus is a silicon lattice, showing its weakly bound electron at cryogenic temperatures. Figure adapted from [45]. Right: An artists’ impression of a phosphorus donor based spin qubit in silicon (credit: William Algar-Chuklin, College of Fine Arts, UNSW).

quantum information processing. Advances in nanofabrication technologies have enabled the construction of semiconductor devices where single electrons can be isolated in artificial or natural atoms [47]. A single spin in a solid-state host is an excellent two-level system for quantum computing. This is because spins can be extremely well isolated from their environment – semiconductors like silicon have a very small spin-orbit interaction (SOI) [48] so that the spins are largely immune to charge noise (a leading source of decoherence in charged-based and certain superconducting qubits). For the simple case of a spin-half particle, i.e. an electron, the qubit states are defined as the up and down spin orientations ($|\uparrow\rangle$ and $|\downarrow\rangle$ respectively), which are separated in energy by the Zeeman splitting $E_Z = g\mu_B B_0$. Figure 1.2 portrays the various methods that have been employed to confine and control few or single electron (and nuclear) spins in solids.

Figures 1.2a-c demonstrates the class of qubit commonly referred to as artificial atoms [49]. Artificial atoms are quantum dots which, due to the tight confinement of electrons and their small effective masses, display properties characteristic of natural atoms such as quantized charge states, quantized energy levels and shell filling [50]. Quantum dots were identified early on as excellent candidates for quantum information processing (QIP) as noted in the seminal proposal by Daniel Loss and David DiVincenzo [51] and follow-on work from Jeremy Levy [52]. Few-electron quantum dots have been defined lithographically (see Fig. 1.2a) in GaAs [50] and SiGe [53] semiconductor heterostructures, where dots are constructed by depleting electrons with metallic electrodes. They have also been produced using Si MOS technology [54], where the dots are formed by accumulating electrons (see Section 2.3). In addition, both Si [55] and GaAs [56, 57] based quantum dots have been operated as spin qubits. Instead of isolating

electrons using electrodes alone, one can utilize the natural one-dimensional (1D) confinement of a quantum wire to produce arrays of single-electron quantum dots (Fig. 1.2b), or the zero-dimensional (0D) confinement of self-assembled quantum dots. Self-assembled quantum dots can be fabricated by using epitaxy to deposit materials with mismatching lattice constants, resulting in small islands of semiconductor forming due to the relaxation of strain energy [43] (see Fig. 1.2c).

Aside from artificial atoms, a large body of work has been carried out on spin qubits based on the nitrogen-vacancy (NV) defect center in diamond. The NV defect (Fig. 1.2d) is a color center with a strong optical transition between its electron spin triplet ground state (${}^3\text{A}$) and a first excited spin triplet state (${}^3\text{E}$). It exhibits a spin-dependent photoluminescence signal that enables optical readout of the spin state [58], permitting room-temperature device operation. Remarkably, the weak SOI in diamond ensures long coherence times even at room temperature. Over the past decade, extraordinary demonstrations of quantum control have taken place in this system, ranging from the operation of single electron [59] and nuclear [60] spin qubits, to the implementation of a quantum spin register [61] to the room temperature entanglement of NV pairs [62]. However, one issue with this system is the low efficiency with which the substitutional nitrogen atoms capture lattice vacancies to produce NV centers [63–65], presenting a challenge for the construction of multi-qubit quantum processors.

The final type of solid-state spin qubit deals directly with the issue of the shrinking silicon transistor and forms the basis of this thesis. By exploiting the silicon MOS fabrication techniques developed over the past few decades, which includes ion-implantation methods [66] for incorporating substitutional donors such as phosphorus (${}^{31}\text{P}$), one can produce devices where it is possible to isolate,

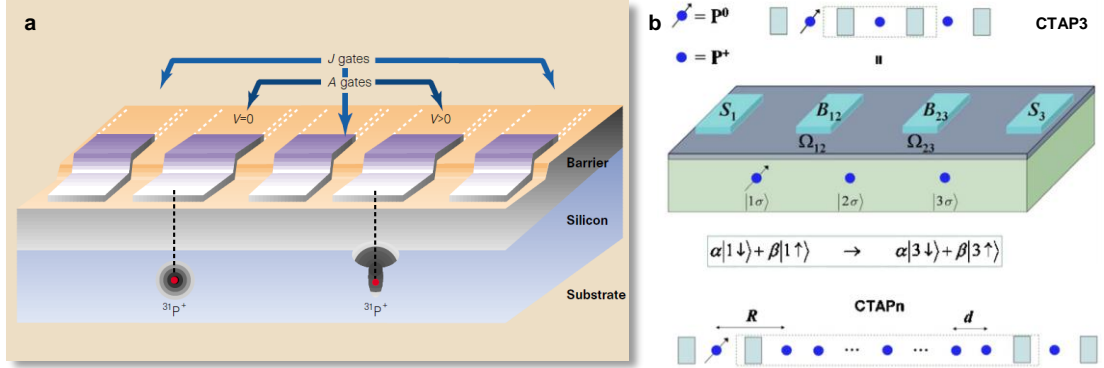


Figure 1.3: Architectures for quantum computing with ^{31}P donors in silicon. **a**, Kane proposal for a quantum computer, taken from [69]. Depicted are the individual donors buried in a silicon substrate, with hyperfine and electron exchange control gates (A-gates and J-gates respectively) fabricated on top of a thin layer of SiO_2 . **b**, Sample device for performing CTAP with the simplest case of a single donor transport channel (top) and the more general case of an arbitrary number of channel donors (bottom). Figure adapted from [70].

measure and control single donors inside silicon chips (see Fig. 1.2e). Methods for building silicon devices with atomic precision in the placement of phosphorus donors [67] have been pioneered at UNSW, however, such devices are not explored in this work. The following section will detail the use of the electron and/or nuclear spin of a single ^{31}P atom as a qubit, an idea that stems from the 1998 proposal of Bruce Kane [68] for a Si:P quantum computer.

1.3 Kane Quantum Computer

Exploiting the fact that spins could potentially be integrated in a solid-state approach [51], the Kane proposal attempts to extend the success of classical electronics to NMR quantum computing [21, 71]. To aid in the scalability of a nuclear spin solid-state computer, it is desirable to find an architecture that enables the electronic measurement and control of individual nuclear spins – which is possible

by exploiting the hyperfine interaction that couples electron and nuclear spins. Because the electron wavefunction extends over large distances through the crystal lattice, it can also be used to mediate coupling between neighboring nuclear spins. This approach has the added benefit that the electron wavefunction (and therefore the hyperfine and electron-mediated interactions) can be controlled with externally applied electric fields.

The most obvious method for achieving electron-nuclear coupling in a semiconductor is to use a donor – an atom that contains one extra valence electron than those of the host lattice, resulting in a positively charged nucleus with a weakly bound electron at cryogenic temperatures. Two primary requirements lead to the eventual selection of phosphorus donors in silicon (Si:P) as the physical system in the Kane proposal. The first requirement was for a host with spin-zero nuclei ($I = 0$). This serves to remove a major channel for decoherence – the dynamics of the nuclear spin bath is a source of magnetic noise which directly couples to the spin qubit [72]. This first requirement eliminated all of the group III-V semiconductors, since none possess stable $I = 0$ isotopes. Fortunately, the dominant material used in the microelectronics industry, silicon, can be isotopically purified to eliminate host nuclear spins. Natural Si has a $\sim 4.7\%$ abundance of the isotope ^{29}Si , which has a spin of $I = 1/2$. The remaining isotopes (^{28}Si and ^{30}Si) are all spin-zero. The ability to create Si wafers with a reduced ^{29}Si concentration means that this magnetic noise can be strongly suppressed, providing longer spin coherence times. The second requirement was for a shallow-level donor. This requirement ensures that the electron wavefunction extends several nanometers away from the nucleus, relaxing constraints on the placement of individual donors and the fabrication of surrounding electrodes. A spin-half ($I = 1/2$) nucleus was

1.3. Kane Quantum Computer

selected, as it provides a well-isolated two-level system – a requirement for quantum computation [18]. The only $I = 1/2$ shallow donor in silicon is phosphorus. It should be noted that a spin-half nucleus is not strictly required here. Donors with $I \geq 1/2$, for example bismuth ($I = 9/2$) [73, 73, 74], can present some very desirable properties and have been the focus of recent experimental investigations [75].

An exhaustive study of the Si:P system over four decades prior to the proposal [48, 76] had already demonstrated its potential for QIP, where measurements deduced a nuclear spin relaxation time exceeding 10 hours at a temperature of $T = 1.25$ K [48]. This knowledge, along with the simplicity of the Si:P system and the wide-spread adoption of phosphorus as an impurity in conventional semiconductor technologies, were all factors in the selection of the donor species.

The basic elements of a Kane quantum computer are shown in Fig. 1.3a. An array of ^{31}P donors is positioned inside a silicon substrate, on top of which a thin oxide (SiO_2) is grown. Directly above each donor an electrode (called the A-gate) is fabricated on the SiO_2 surface. In between adjacent donor pairs an additional electrode (referred to as the J-gate) is defined, with a typical separation of ~ 10 nm between the gates. A quantum logic gate with this device proceeds by controlling three external parameters: (1) An external global oscillating magnetic field is applied, typically from within the radio-frequency (RF) spectrum. The NMR frequency is carefully chosen to be in resonance with the donor nuclear spin state energy splitting. This field serves to induce controlled nuclear spin flips. (2) Voltages applied to the A-gates are used to distort the electron wavefunction, altering its overlap with the nucleus. This creates a “Stark shift” [77])

of the hyperfine interaction constant and causes a change in the nuclear Larmor precession frequency. The Stark shift can be used to bring individual nuclear spin qubits in or out of resonance with the global oscillating magnetic field. (3) The J-gates are employed to attract electrons from adjacent donors, providing control over their wavefunction overlap. Due to the exchange symmetry of indistinguishable particles, an exchange interaction arises from the overlap, which can be used to mediate an indirect interaction between the nuclear spins. By adjusting the coupling of each nuclear spin to its neighbors and to the oscillating field, one can perform different operations on each of the spins simultaneously. Measurement of a qubit is achieved using a pair of donors. The nuclear spin polarization is first transferred to the electrons, then through a process which involves adiabatically evolving the exchange interaction, the coupled two-electron spin state is projected onto the orbital state of one of the donors. Detection of the charge state of the donors – initially envisaged to be achieved by performing sensitive capacitance measurements between gates [78], but more likely realized through employing a single electron transistor (SET) [79] – will then reveal the nuclear spin orientation.

1.3.1 A Quasi-2D Architecture

The Kane proposal, whilst detailing a new solid-state qubit with many attractive properties, does not outline how the qubit would be utilized in a scalable quantum computing architecture. The scalability of a given design is much more complex than just the fabrication of many interacting qubits, it requires the consideration of systems-level issues, one of the most important being the implementation of quantum error correction (QEC) schemes [80, 81]. It has been shown that

the linear nearest neighbor (LNN) qubit communication employed in the Kane proposal is not ideal for executing these schemes [82]. Removing the burden of nearest neighbor communication is highly desirable, because it raises the allowed error thresholds for fault tolerant quantum computing.

A potential solution for the constraints imposed by a linear array of donor qubits was put forward by Hollenberg et al. [70]. This proposal is a modification of Kane’s original idea, with the most radical change being that it employs the ^{31}P donor electron (instead of nuclear) spin as a quantum bit. The donor electron spin is also known to have extremely long relaxation times in silicon (thousands of seconds at temperatures below ~ 2 K) [48] and more recent measurements have demonstrated its remarkable coherence preserving capabilities when hosted in isotopically enriched ^{28}Si substrates [83], making it an excellent qubit. Non-local communication is achieved in this scheme by transporting the electron spins across buried arrays of ionized donors, providing pathways for in-plane vertical and horizontal shuttling of qubit states to interaction regions which contain the familiar A and J gates. An outline of the transport mechanism is depicted in Fig. 1.3b. The gates $B_{i,i+1}$ serve to control the tunnel barrier and hence tunnel rate $\Omega_{i,i+1}$ between donors i and $i + 1$. Coherent spin transport across an array is accomplished by adiabatically lowering and increasing the tunnel rates $\Omega_{i,i+1}$ in a well-defined sequence to achieve coherent transfer by adiabatic passage (CTAP) [84]. One intriguing feature of the CTAP sequence is the ability to transfer the electron from one end of the chain to the other without populating the intervening channel donors.

The top portion of Fig. 1.3b presents the simplified case of a one donor channel where the states $|1\sigma\rangle$, $|2\sigma\rangle$ and $|3\sigma\rangle$ represent electron occupancy of the first

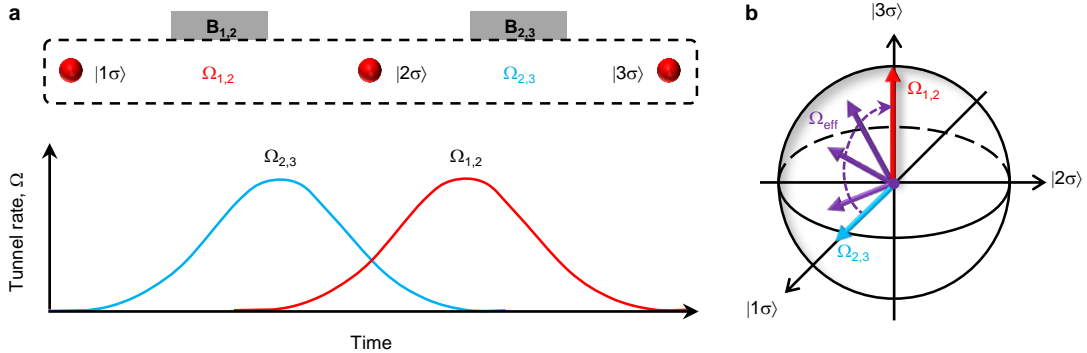


Figure 1.4: CTAP chain, pulse sequence and state evolution. **a**, Three donor CTAP chain (top) and the counter-intuitive tunnel rate control sequence (bottom), employed to adiabatically transfer the system from the state $|1\sigma\rangle$ directly to $|3\sigma\rangle$, without ever populating $|2\sigma\rangle$. **b**, State evolution during CTAP.

donor, the second (or “channel”) donor and the third donor, with σ indicating the spin state ($\sigma = \downarrow, \uparrow$). A counter-intuitive pulse sequence is used to transfer the electron from $|1\sigma\rangle$ directly to $|3\sigma\rangle$ without ever occupying the middle state $|2\sigma\rangle$. Fig. 1.4a depicts Gaussian modulations of the tunnel rates $\Omega_{1,2}$ and $\Omega_{2,3}$ between donors 1 and 2 and donors 2 and 3, resulting from controlled voltage pulses on the barrier gates $B_{1,2}$ and $B_{2,3}$. The tunnel barrier is *first* lowered between the ionized channel and third donor, it is then adiabatically raised (tunnel rate lowered) as the barrier between the channel and occupied first donor is simultaneously lowered. The end result is an effective coupling that adiabatically evolves the system from $|1\sigma\rangle$ to $|3\sigma\rangle$. The charge state evolution can be illustrated on a Bloch-sphere-like geometrical representation, as depicted in Fig. 1.4b. Since the SOI in silicon is extremely weak, the charge and spin degrees of freedom are essentially decoupled. Furthermore, the electron wavefunction maintains a large s-orbital component (even when the tunnel barrier is lowered) and has a negligible occupation probability of the channel state. These factors imply that charge dephasing will have very little effect on the electron spin coherence during

transport. Of greater concern are the hyperfine interactions at $|1\sigma\rangle$ and $|3\sigma\rangle$, where the nuclear spin states and hyperfine Stark shifts will need to be precisely controlled in order to avoid decoherence. This idea can be extended to large channels of donors (bottom portion of Fig. 1.3b), and is relatively robust to any variations in tunnel rates between adjacent donors that would likely result from donor placement.

1.3.2 Si:P Qubit Physical Implementation

Following the conceptual development of the Si:P electron-spin-based quantum computer [70], research became focused on solving the practicalities of building and experimentally demonstrating a single ^{31}P electron spin qubit. The work in Ref. [85] outlined a detailed architecture for achieving high-fidelity readout and control of the electron spin of an individual ^{31}P donor in silicon. The idea exploited a nanoelectronic device known as a silicon MOS single electron transistor (see Section 2.3 for details), which acts as a sensitive electrometer and is used to detect the qubit state through a process known as spin-to-charge-conversion (see Chapter 3). The architecture also included an on-chip broadband transmission line (Section 2.4) for delivering the high frequency microwave magnetic fields necessary to drive electron spin rotations – a technique referred to as electron spin resonance (ESR). Local field generation is useful for single to few qubit device demonstrations, as the sample fabrication is somewhat more manageable if it does not need to be housed inside a specially crafted microwave cavity [76] and the experimental infrastructure is also simplified.

This architecture [85] forms the basis for the devices investigated throughout this thesis. The experimental realization of both ^{31}P electron and nuclear spin

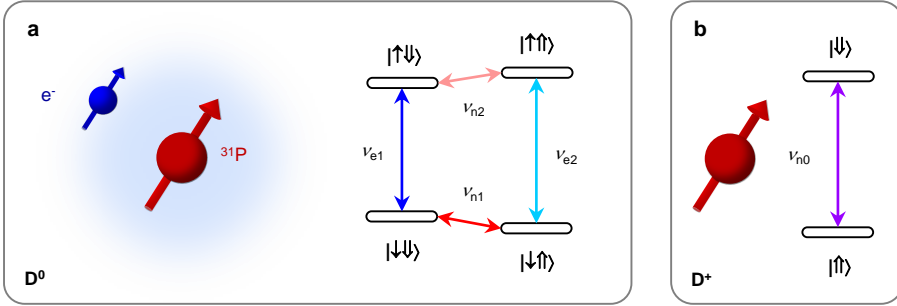


Figure 1.5: Eigenstates and spin transitions of a single ^{31}P donor in Si. **a**, Energy level diagram of the neutral ^{31}P donor system, with corresponding ESR (blue) and NMR (red) transitions. $\downarrow\uparrow$: electron spin states; $\downarrow\uparrow\downarrow\uparrow$: nuclear spin states. The depicted states are approximately eigenstates of the system in the high magnetic field limit $\gamma_e B_0 \gg A_{\parallel}$ under which experiments here are performed. **b**, Energy level diagram of the ionized ^{31}P donor, with the single NMR transition shown in purple. Here the $|\downarrow\downarrow\rangle$ state is highest in energy as a result of the positive value of the nuclear gyromagnetic ratio.

qubits using these devices [86, 87] is testament to the success of this architecture and the great promise of the Si:P system for quantum computing.

1.4 The Si:P Physical System

The ^{31}P donor in silicon can be thought of as the equivalent of a hydrogen atom, in a solid-state matrix. It possesses a nuclear spin $I = 1/2$, and the excess charge of the phosphorus nucleus, as compared to the surrounding silicon nuclei, creates a Coulomb potential that can bind an extra electron (with spin $S = 1/2$) in the neutral D^0 donor charge state [88]. Therefore, a single ^{31}P donor constitutes a two-qubit system, where the two qubits interact with an external magnetic field B_0 in proportion to their gyromagnetic ratios: $\gamma_n = 17.23 \text{ MHz/T}$ for the nucleus [89]; and $\gamma_e = g\mu_B/h = 27.97 \text{ GHz/T}$ for the electron, where h is Planck's constant and the electron Landé g -factor is known to be $g = 1.9985$ from measurements on bulk phosphorus-doped silicon samples [76]. γ_e is actually

a negative quantity, thus it should be taken here to mean $|\gamma_e|$. In addition, they interact with each other through the hyperfine interaction $A = 117.53$ MHz (Ref. [76]), which arises from the overlap of the electron wavefunction with that of the ^{31}P nucleus. The Hamiltonian describing this two-spin coupled system is given by Eq. 1.1.

$$\mathcal{H} = \gamma_e B_0 S_z - \gamma_n B_0 I_z + \mathbf{S} \cdot \underline{\underline{A}} \cdot \mathbf{I} \quad (1.1)$$

where S_z (I_z) is the z-component of the electron (nuclear) spin and $\underline{\underline{A}}$ is the hyperfine tensor between the electron and nuclear spins with isotropic component A_{\parallel} and anisotropic component A_{\perp} :

$$\underline{\underline{A}} = \begin{pmatrix} A_{\parallel} & 0 & A_{\perp} \\ 0 & A_{\parallel} & 0 \\ A_{\perp} & 0 & A_{\parallel} \end{pmatrix}, \quad (1.2)$$

If we assume the hyperfine coupling to be completely isotropic (see Section 5.5 for further discussion on this topic), i.e. $A_{\perp} = 0$, then solving Eq. 1.1 yields the following eigenstates [89]:

$$\begin{aligned} |\varphi_1\rangle &= \cos(\eta/2) |\downarrow\uparrow\rangle - \sin(\eta/2) |\uparrow\downarrow\rangle \\ |\varphi_2\rangle &= |\downarrow\downarrow\rangle \\ |\varphi_3\rangle &= \cos(\eta/2) |\uparrow\downarrow\rangle + \sin(\eta/2) |\downarrow\uparrow\rangle \\ |\varphi_4\rangle &= |\uparrow\uparrow\rangle \end{aligned} \quad (1.3)$$

where $\tan(\eta) = A_{\parallel}/(\gamma_e B_0)$ and we define $\gamma_{\pm} = \gamma_e \pm \gamma_n$. Under our experimental conditions, $\gamma_e B_0 \gg A_{\parallel} > 2\gamma_n B_0$, and $\sin(\eta/2) \approx 0$. This means that

the eigenstates of the two-spin system are approximately provided by the tensor products of those of their individual Hilbert spaces (in ascending order of energy) $|\downarrow\uparrow\rangle$, $|\downarrow\downarrow\rangle$, $|\uparrow\downarrow\rangle$, $|\uparrow\uparrow\rangle$, where the thin (thick) arrow indicates the orientation of the electron (nuclear) spin (Fig. 1.5a). The energies of these states are given (in frequency units) by:

$$\begin{aligned} E_{\downarrow\uparrow} &= \frac{-\sqrt{(\gamma_+ B_0)^2 + A^2} - A/2}{2} \\ E_{\downarrow\downarrow} &= \frac{-\gamma_- B_0 + A/2}{2} \\ E_{\uparrow\downarrow} &= \frac{\sqrt{(\gamma_+ B_0)^2 + A^2} - A/2}{2} \\ E_{\uparrow\uparrow} &= \frac{\gamma_- B_0 + A/2}{2} \end{aligned} \tag{1.4}$$

As will be described in this thesis, the system can be transformed to that of a single ^{31}P nuclear spin (Fig. 1.5b) with eigenstates $|\uparrow\rangle$ and $|\downarrow\rangle$ and corresponding energies $E_{\uparrow} = -\gamma_n B_0/2$ and $E_{\downarrow} = \gamma_n B_0/2$, by ionizing the donor to the D^+ charge state. We can address the electron spin qubit by applying microwave pulses at the transition frequencies $\nu_{\text{e}1} = E_{\uparrow\downarrow} - E_{\downarrow\downarrow}$ or $\nu_{\text{e}2} = E_{\uparrow\uparrow} - E_{\downarrow\uparrow}$. Likewise, we can address the neutral donor nuclear spin by sending RF excitations at $\nu_{\text{n}1} = E_{\downarrow\downarrow} - E_{\downarrow\uparrow}$ or $\nu_{\text{n}2} = E_{\uparrow\uparrow} - E_{\uparrow\downarrow}$ (or ionized donor nuclear spin at $\nu_{\text{n}0} = E_{\downarrow} - E_{\uparrow}$). In the high magnetic field limit $\gamma_e B_0 \gg A_{\parallel}$, these expressions for the spin transition frequencies become:

$$\begin{aligned} \nu_{\text{e}1} &= \gamma_e B_0 - A_{\parallel}/2 \\ \nu_{\text{e}2} &= \gamma_e B_0 + A_{\parallel}/2 \end{aligned} \tag{1.5}$$

for the electron, and:

$$\begin{aligned}\nu_{n1} &= A_{\parallel}/2 + \gamma_n B_0 \\ \nu_{n2} &= A_{\parallel}/2 - \gamma_n B_0\end{aligned}\tag{1.6}$$

for the nucleus.

Whilst the Si:P physical system was one of the first to be investigated after the invention of pulsed electron spin resonance techniques [90], it is still as relevant as ever today. Modern-day interest stems from its exciting potential for QIP. Recent measurements performed on bulk phosphorus-doped silicon samples have revealed the exceptional abilities of both the electron and nuclear spins to store quantum information over extended periods of time. In particular, by using isotopically enriched ^{28}Si chips, coherence times of up to 10 seconds have been measured in ensembles of donor electron spins [83] and times of ~ 44 seconds for the donor nuclear spins, raising the prospects of long lived solid-state quantum bits. Such experiments have lead to the term “semiconductor vacuum” being used to describe the (isotopically pure) $^{28}\text{Si:P}$ system – in reference to the long coherence times of qubits constructed from ions trapped in electromagnetic fields inside a near-perfect vacuum [91]. Other experiments on bulk-doped samples have demonstrated techniques for utilizing the nuclear spin as a quantum memory for the electron spin [92] and for generating entanglement in an ensemble of ^{31}P electron and nuclear spins [93]. Together with the single-donor measurement and control techniques described in this dissertation, these rich demonstrations have solidified the applicability of the Si:P system for quantum computing.

1.5 Thesis Outine

Chapter 2 gives an overview of the equipment and techniques employed throughout this thesis to fabricate and operate the single atom quantum bit devices. Details are given of the experimental setup, including a wiring schematic of the dilution refrigerator and associated room-temperature measurement electronics and a characterization of the single electron transistor charge sensitivity.

Chapter 3 describes the first demonstration of single-shot, time-resolved readout of an electron spin bound to a single ^{31}P donor in Si. This is achieved using a device consisting of implanted phosphorus donors coupled to a metal-oxide-semiconductor single electron transistor – compatible with current micro-electronic technology. A comprehensive analysis of the spin readout device is performed and its non-idealities investigated. The electron spin lifetime is measured, and found to be $T_1 \approx 6$ seconds at a magnetic field $B_0 = 1.5$ T, and the physical mechanisms for spin relaxation are discussed. Finally, a spin readout fidelity better than 90% is extracted from a combination of experimental data and simulations. The results of this chapter indicate that the electron spin can potentially be operated as a long-lived qubit with high fidelity all-electrical measurement and initialization.

Chapter 4 details the coherent manipulation of a single ^{31}P donor electron spin qubit in natural silicon. Measurements are performed electrically using the single-shot readout techniques introduced in Chapter 3 and with a device architecture similar to that utilized in the spin readout experiments, but with the addition of an on-chip broadband transmission line. Electron spin resonance is employed to

1.5. Thesis Outine

drive Rabi oscillations, while a Hahn echo pulse sequence reveals a spin coherence time (T_2) exceeding 200 μ s. Dynamical decoupling extends the coherence time and demonstrates qubit control about orthogonal axes on the Bloch sphere. A model is then developed and used to breakdown and analyze the electron qubit system fidelity.

Chapter 5 realizes a key component of the Kane quantum computer – a single ^{31}P nuclear spin qubit. Integrating single-shot readout of the electron spin (Chapter 3) with on-chip electron spin resonance (Chapter 4), enables the quantum non-demolition, electrical single-shot readout of the nuclear spin. Measured readout fidelities are better than 99.8% – the highest for any solid-state qubit. Quantum jumps of the nuclear spin are observed on minutes-long timescales, the mechanisms behind the nuclear spin flips are discussed and modeled numerically. The single nuclear spin is operated as a qubit by applying coherent radiofrequency pulses at frequencies found from nuclear magnetic resonance experiments. Hahn echo and Ramsey fringe measurements reveal the nuclear spin coherence times, which are shown to depend on the charge state of the donor. For an ionized ^{31}P donor the nuclear spin coherence lasts as long as 60 ms, with a 1-qubit gate control fidelity in excess of 98%.

Chapter 6 explores the local nuclear spin environment surrounding the single phosphorus donor. By using the sensitive nuclear spin detection techniques of Chapter 5 and very low electron spin resonance powers, the quantum non-demolition, electrical single-shot readout of an individual hyperfine-coupled ^{29}Si nuclear spin is achieved. The coherence of the single ^{29}Si spin is measured and

agrees well with expectations based on ensemble measurements in bulk samples. As well as providing unprecedented insight to the spin dynamics of the Si:P system at the single donor scale, the work in this chapter raises the prospect of utilizing individual host lattice nuclear spins as a possible resource for quantum computing.

Chapter 7 presents an overview of the most important advances reported in this dissertation. Suggestions are made for improvements along with an outlook on future experiments.

Chapter 2

Experimental Methods

This chapter describes the device fabrication process and experimental techniques employed throughout this thesis. All of the devices investigated were fabricated in the Semiconductor Nanofabrication Facility at the University of New South Wales. Measurements were performed in the Quantum Spin Control Laboratory (formerly the National Magnet Laboratory), University of New South Wales.

The author acknowledges K. W. Chan, K. Y. Tan and W. H. Lim for the fabrication of devices and J. P. Dehollain for the design and modeling of the microwave transmission line.

2.1 Device Fabrication

UNSW is home to the Semiconductor Nanofabrication Facility (SNF), a class 3.5 clean room. The SNF has facilities for a wide range of micro and nano-scale semiconductor fabrication techniques including silicon oxidation, electron-beam lithography (EBL), photolithography, metal deposition/evaporation and plasma and ion etching.

The devices used in this thesis (for example see Fig. 2.1a) were fabricated on a high-purity, near-intrinsic, natural-isotope [100] silicon substrate, with n^+ ohmic source/drain contacts obtained by phosphorus diffusion. A high-quality, 8 nm thick SiO_2 gate oxide was grown by dry oxidation at 800 °C. Phosphorus ions were implanted through a $90 \times 90 \text{ nm}^2$ aperture defined by electron-beam lithography in a polymethyl-methacrylate (PMMA) mask. The fluence was chosen to obtain the maximum likelihood of having ~ 3 P atoms in a $30 \times 30 \text{ nm}^2$ area (see Section 3.4), subject to Poisson statistics. The implantation energy was 14 keV, resulting in an average depth of ~ 15 nm below the Si/SiO_2 interface. A 5 s, 1000 °C rapid thermal anneal was performed to activate the donors and repair the implantation damage. The aluminium gates to form the spin read-out device and microwave transmission line (see Fig. 2.1b) were defined with electron-beam lithography using the process described in Ref. [94]. The left and right barrier gates (LB and RB respectively) and plunger gate (PL) were written in a first EBL step, followed by Al thermal evaporation and lift-off. The barrier and plunger gates were next passivated by oxidation on a hot plate at 150 °C in the clean room atmosphere, resulting in an electrically-insulating Al_xO_y layer approximately 3 nm thick. A second EBL step and aluminium layer was employed to define the transmission line and top gate (TG). A final forming gas anneal

2.2. Measurement Setup

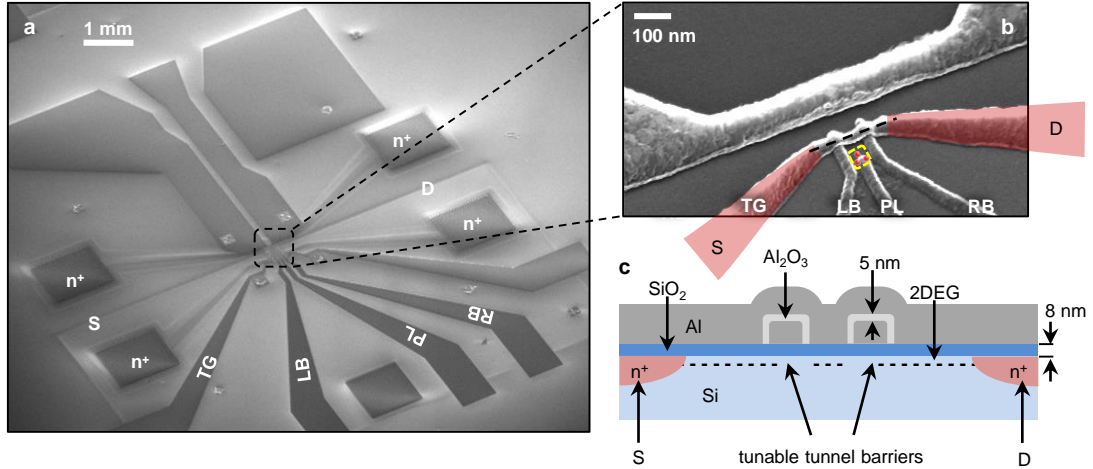


Figure 2.1: SEM micrographs and cross-section sketch of the Si:P qubit device. **a**, SEM micrograph showing the device micro-fabrication. **b**, SEM micrograph of the device nano-fabrication, with source/drain diffusion regions marked in red. The active implant area ($30 \times 30 \text{ nm}^2$) is marked by the yellow dashed box, which encompasses ~ 3 donors (red solid circles) subject to Poisson statistics. The black dashed line indicates the region through which the cross-section is taken in **c**. **c**, Sketch of a cross-section through the SET, as indicated in **b**. Applying a positive voltage to the top gate (TG) will induce a two-dimensional electron gas (2DEG) at the Si/SiO₂ interface. Applying less positive voltages to the barrier gates (LB and RB) locally depletes the 2DEG, forming tunnel barriers with opacities that can be tuned *in situ*. Sketch is not to scale.

(400 °C, 15 min., 95% N₂ / 5% H₂) was performed to reduce the interface trap density to the level of $\sim 2 \times 10^{10} \text{ cm}^{-2} \text{ eV}^{-1}$, as measured on devices fabricated with the same process [95]. Figure 2.1a presents a scanning electron microscope (SEM) image of the device used to perform spin readout (Chapter 3) as well as the on-chip broadband transmission line used for spin control (Chapters 4-6). A zoom-in of the device nano-fabrication is given in Fig. 2.1b, with a cartoon impression of a cross-section through the middle of the SET in Fig 2.1c.

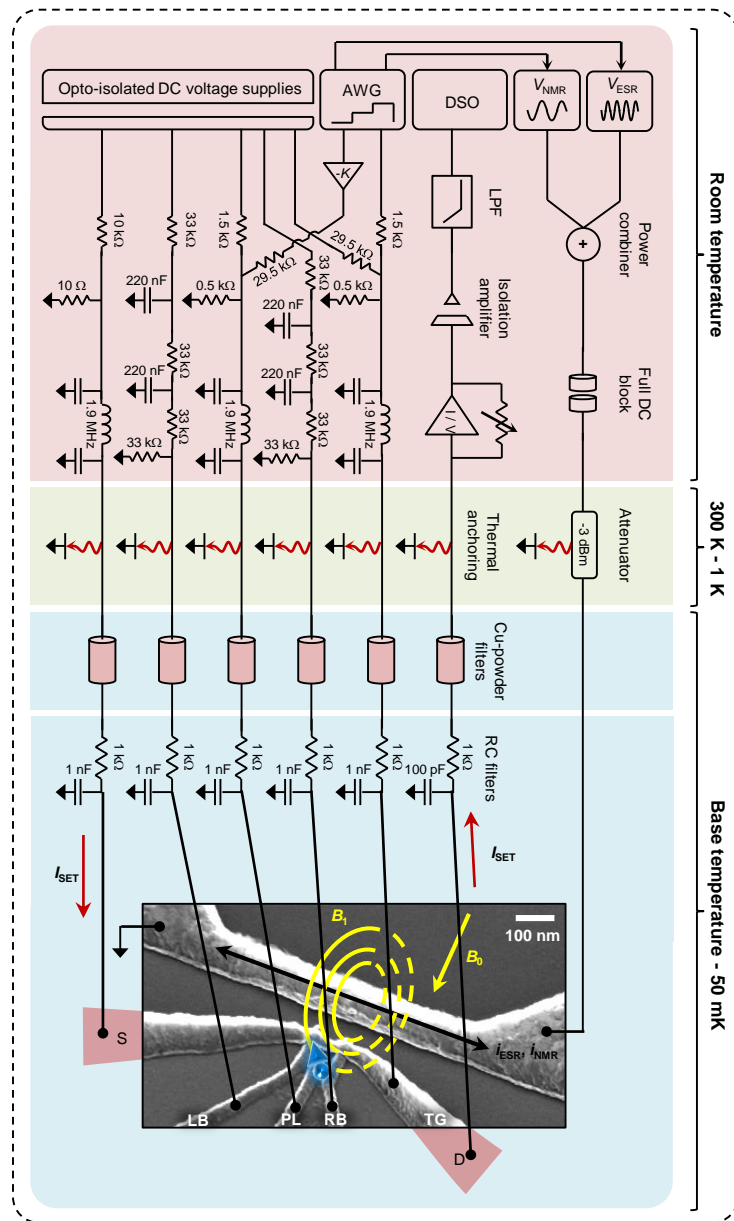


Figure 2.2: Wiring and equipment for qubit measurements. This schematic depicts the experimental setup from room temperature to the base temperature of the dilution refrigerator. The right-most part of the setup contains the equipment and high frequency line used to deliver the radio-frequency and microwave excitations for spin control. The remaining setup is for applying gate voltages and detecting current through the SET.

2.2 Measurement Setup

The sample was mounted on a high-frequency gold-coated printed circuit board in a copper enclosure, and thermally anchored to the cold finger of a Oxford Kelvinox 100 dilution refrigerator, with base temperature $T_{\text{bath}} \approx 40$ mK. The [110] crystal axis in the plane of the chip was oriented parallel to the axis of a 75 mm bore superconducting magnet, used to apply magnetic fields. The device possesses four gates: the left and right barriers (LB and RB), the top gate (TG) and the plunger gate (PL). In addition it has source and drain contacts (S and D) and a transmission line for spin control (Fig. 2.1). The four gates and S/D contacts were all connected to stainless steel inner/outer conductor semi-rigid coaxial lines. The lines were fitted with SMA connectors and ran from room temperature all the way to the base stage of the fridge. These stainless steel coaxials provided a low thermal conductivity and sufficient bandwidth for the pulsing and current detection of the spin readout experiments (Chapter 3).

Whilst the lattice phonons will be at a temperature roughly corresponding to that of the cold finger – a copper flange connected to the mixing chamber (the coldest part of the fridge) to which the sample enclosure is fixed – the electron temperature T_{el} is predominantly determined by the lines connecting to the S/D contacts and gates. In order to lower the temperature of the lines, they were bound to copper posts at the various temperature stages of the fridge using copper wire and coated with GE 7031 varnish (this thermal anchoring is represented by the green region in Fig. 2.2). Electrical noise and high frequency radiation in the lines were suppressed through the use of RC and Pi filters at room temperature and a combination of copper-powder and RC filters at base temperature (see Fig. 2.2 for details). Whilst the Pi and RC filters are good for

removing low to mid frequency noise (DC - ~ 1 GHz), they perform less well at high frequencies. The copper-powder filters [96] are copper enclosures containing wires that form counter-wound coils (first wound in one direction and then the other) in order to lower their inductance and minimize any crosstalk with other lines. The enclosures are filled with a fine copper powder, which serves to absorb high-frequency (GHz) noise. The lowest observed electron temperature with this setup was $T_{\text{el}} \approx 200$ mK (Section 3.9).

All DC voltages to the gates were provided by opto-isolated and battery-powered voltage sources, hosted in a Stanford Research Systems (SRS) SIM900 mainframe. For the LB and RB gates, the DC voltage sources were connected to resistive voltage dividers, which were located at room temperature on top of the dilution refrigerator. For the plunger and top gates, the DC voltages were passed to an additive resistive network (also at room temperature), which combined them with pulses produced by an arbitrary waveform generator (AWG) before being sent to the sample. For the electron spin readout experiments, we applied compensated pulses to the plunger and top gates. The pulse signal from the AWG (Tektronix AWG520) was therefore connected to an SRS SR560 inverting pre-amplifier (which multiplied it by a variable gain $-K$) before it was passed to the resistive adder of the plunger gate. The SET current was measured by a Femto DLPCA-200 transimpedance amplifier at room temperature, followed by a voltage post-amplifier (SRS SIM910), a analog 6th order low-pass Bessel filter (SRS SIM965), and a fast digitizing oscilloscope (Agilent DSO8104A). Full details of the room temperature electronics are provided in the schematic of Fig. 2.2.

For the electron and nuclear spin control experiments, ESR excitations were produced by an Agilent E8257D microwave analog signal generator and the NMR

2.3. Single-Electron Transistor

excitations by an Agilent MXG N5182A RF vector signal generator. The two signals were combined at room-temperature with a power divider/combiner, before being guided to the sample by a semi-rigid coaxial cable (2.2 m in length). The cable was constructed of a cupronickel outer conductor and silver-plated cupronickel inner conductor. This type of cable has low enough thermal conductivity, as required for operation in a dilution refrigerator, but the silver plating of the inner conductor allows for very low losses even above 10 GHz. Thermalization of the inner conductor was provided by a 3 dB attenuator placed at 4 K and the outer conductor was thermalized in the same manner as the coaxial cables described above. A full DC block (with a rated bandwidth 10 MHz-18 GHz), where both the outer and inner conductors are galvanically discontinuous, was installed on the fast line at room temperature. The DC block is used to prevent ground loops and suppress DC current signals (for example due to an offset voltage on the source output) that may run through the attenuator at 4 K.

The short spin control excitations were produced by using the fast-pulse generating capabilities (option UNW, narrow-pulse modulation) of the Agilent microwave and RF sources. The ESR/NMR pulses were gated externally by the AWG, which was synchronized with the TG and PL pulses. Phase-shifted pulses were obtained by using phase modulation (option UNT), where a minimum delay between consecutive phase-shifted pulses of $\sim 10 \mu\text{s}$ was set by the 1 MHz modulation bandwidth.

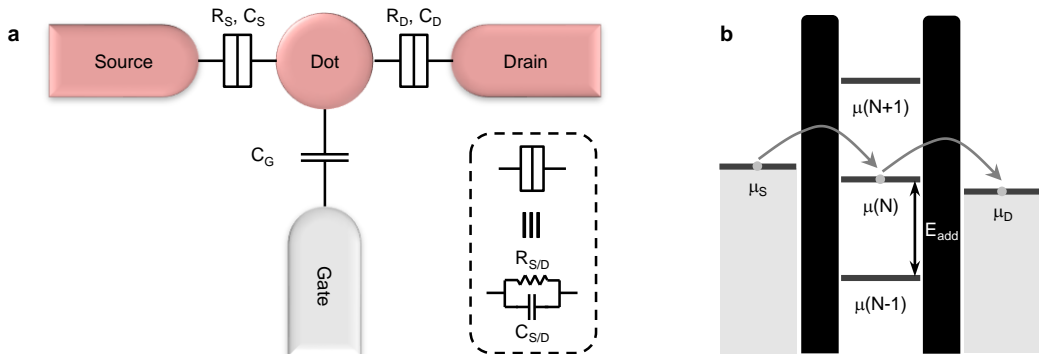


Figure 2.3: The general construction and operation of a single-electron transistor. **a**, Schematic representing the fundamental elements of a single-electron transistor. A quantum dot (or “island”) is tunnel-coupled to source and drain reservoirs, whilst a capacitively-coupled gate controls the electrochemical potential ladder of the dot. **b**, Electrochemical potential diagram showing transport when the electrochemical potential to add the N th electron to the dot is between the Fermi levels of the source and drain.

2.3 Single-Electron Transistor

2.3.1 Operating Principles

Quantum dots are nanometer to micrometer sized structures that display quantum effects with striking similarities to real atoms [49]. For example, the tight confinement of electrons inside these objects can result in a measurable quantization of the energy levels (often called single-particle levels). Even when the dot size is too large to allow the observation of quantized single-particle levels, the combination of charge quantization (integer electron number in the island) and classical charging effects allow the dot to be used as a very sensitive electrometer, often called Single-Electron Transistor (SET). Just as with a conventional capacitor, there is an energy associated with storing a charge on the quantum dot, given by $E = Q^2/(2C)$, where Q is the charge stored and C the capacitance. When we consider storing just a single electron ($Q = e$), this energy (Eq. 2.1) becomes vanishingly small for classical (large) capacitors. But for quantum dot

sized structures, where capacitances are routinely of order femto Farads (10^{-15} F), this single electron charging energy E_C can become important – especially when operating at the mK temperatures of a dilution refrigerator where $E_C \gg k_B T$.

If the quantum dot is then connected to the outside world by source and drain leads (Fig. 2.3a), charge in the system will rearrange itself in order to minimize the energy of the whole circuit. The dot is a floating “island”, and the tunnel coupling between this island and the source and drain – characterized by an effective tunnel resistance $R_{S/D}$ and capacitance $C_{S/D}$ (see Fig. 2.3a) – enables charge to be added to and removed from the system. Additional control over the electrostatic environment is provided by a capacitively-coupled gate electrode, with a capacitance C_G to the dot. Charge will remain discrete (i.e. an integer number of electrons N on the island) if the charging energy:

$$E_C = \frac{e^2}{2C_\Sigma} \quad (2.1)$$

where $C_\Sigma = C_G + C_S + C_D$ is the total capacitance of the dot, is significantly larger than the uncertainty in electron energy ΔE arising from the finite dwell time of the electron on the island. According to the energy-time uncertainty principle:

$$\Delta E > \frac{\hbar}{2\Delta t} \quad (2.2)$$

where $\Delta t \cong R_{S/D}C_\Sigma$ is the RC time constant, determined by the tunnel resistance between dot and source-drain, and the total capacitance of the dot. Quantum fluctuations are therefore suppressed if the tunnel resistance exceeds the resistance quantum, i.e. $R_{S/D} \gg h/e^2 = 25.8 \text{ k}\Omega$ [97].

A full description of the electronic states of the quantum dot is provided by

the constant-interaction (CI) model [49, 98]. The CI model is based on two assumptions: (i) That the Coulomb interaction between each electron on the dot with all others inside and outside of the dot, is captured by the single constant capacitance C_Σ . (ii) The discrete quantum states of the dot (e.g. due to confinement) are not affected by these interactions. The model then gives the following ground state energy estimate for a N -electron dot [99]:

$$U(N) = \frac{[-|e|(N - N_0) + C_S V_S + C_D V_D + C_G V_G]^2}{2C_\Sigma} + \sum_{n=1}^N E_n(B_0) \quad (2.3)$$

where N_0 is the number of electron on the dot when $V_G = 0$ and $E_n(B_0)$ is the single-particle energy level in an external magnetic field B_0 [98].

The electrochemical potential of the dot $\mu(N)$ is defined as the energy needed to add the N th electron:

$$\begin{aligned} \mu(N) &= U(N) - U(N - 1) \\ &= \left(N - N_0 - \frac{1}{2} \right) E_C - \frac{E_C}{|e|} (C_S V_S + C_D V_D + C_G V_G) + E_N \end{aligned} \quad (2.4)$$

where we have dropped the magnetic field dependence of the single-particle state energy for brevity. The energy separation between consecutive electrochemical potentials is called the addition energy:

$$E_{add}(N) = \mu(N + 1) - \mu(N) = E_C + \Delta E_n \quad (2.5)$$

The quantity ΔE_n can be zero if the electron is being added to the same spin-degenerate level. In larger dots, it is typically the case that $\Delta E_n \ll E_C$, and one obtains a uniformly spaced electrochemical potential ladder, as depicted in

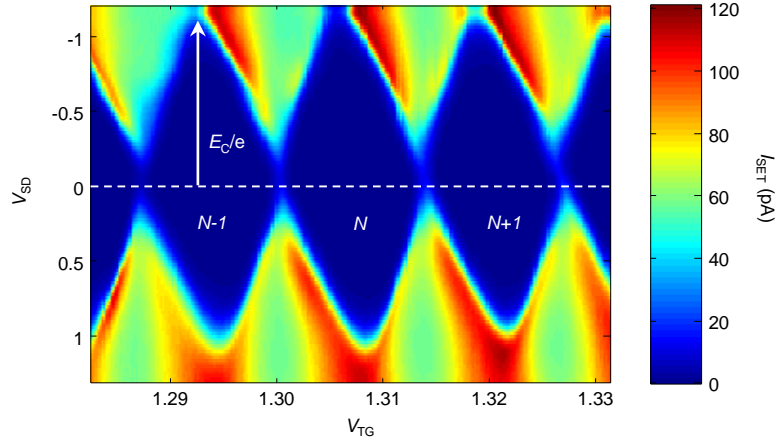


Figure 2.4: SET bias spectroscopy. Coulomb diamonds of the SET taken with $V_{LB} = V_{RB} \approx 0.8$ V and $V_{PL} \approx 0.15$ V. From the diamonds we extract a charging energy of $E_C \approx 1.2$ meV.

Fig. 2.3b. Using the gate voltage V_G , the ladder can be shifted to move levels in and out of the bias window defined by the source and drain electrochemical potentials (i.e. between the levels μ_S and μ_D). As levels pass through this window, sequential tunneling of single electrons from source to island to drain occurs – hence the name single electron transistor (SET). When no level exists between μ_S and μ_D , the SET is said to be in Coulomb blockade and no current flows. Scanning V_G whilst monitoring the source to drain current produces periodic “Coulomb oscillations”, as shown in Fig. 2.5b. These peaks possess steep roll-offs (i.e. large $\delta I/\delta V$) and can therefore be exploited to measure small changes in the charge environment surrounding the quantum dot. A fluctuating charge will shift the potential of the SET island and modulate the current through the device. This important feature is key to the ability to measure the spin of a single electron and will be utilized throughout this thesis.

2.3.2 Si MOS SET

Whilst there are many physical systems capable of realizing a SET [49], the one employed in this thesis is based on Si MOS technology [94]. Here the SET is derived from an electrostatically-induced two-dimensional electron gas (2DEG) at a Si/SiO₂ interface, using aluminium gates defined by electron-beam lithography, as depicted in Fig. 2.1c. Applying a voltage to the top gate of $V_{TG} \approx 1$ V induces the 2DEG, which is locally depleted beneath the barriers by setting slightly less positive voltages for V_{LB} and V_{RB} . This results in the formation of an island beneath TG and between LB and RB, which acts as the quantum dot and is tunnel-coupled to the source and drain leads via the electrically tunable tunnel barriers (see Fig. 2.1c).

The SET island has a lithographic area of $\sim 50 \times 90$ nm² and a corresponding charging energy of $E_C \approx 1.2$ meV. The charging energy is found by performing bias spectroscopy, where Coulomb oscillations are observed (as a function of the top gate voltage V_{TG}) at different source/drain biases $\mu_S - \mu_D$. Figure 2.4 demonstrates the outcome of such a measurement – “Coulomb Diamonds” are observed, with their heights providing the addition energy ($\approx E_C$).

2.3.3 Measurement of SET Charge Sensitivity

Key to the success of these single spin experiments is the ability to detect small charge fluctuations over a wide bandwidth and with great accuracy. State-of-the-art in charge detection is the radio frequency single electron transistor (RF-SET), where sensitivities of order $10^{-5} - 10^{-6} e/\sqrt{\text{Hz}}$ and MHz bandwidths are possible [100, 101]. However, utilizing an RF-SET for our single-shot spin detection measurements is challenging due to the presence of the RF voltage excitation

2.3. Single-Electron Transistor

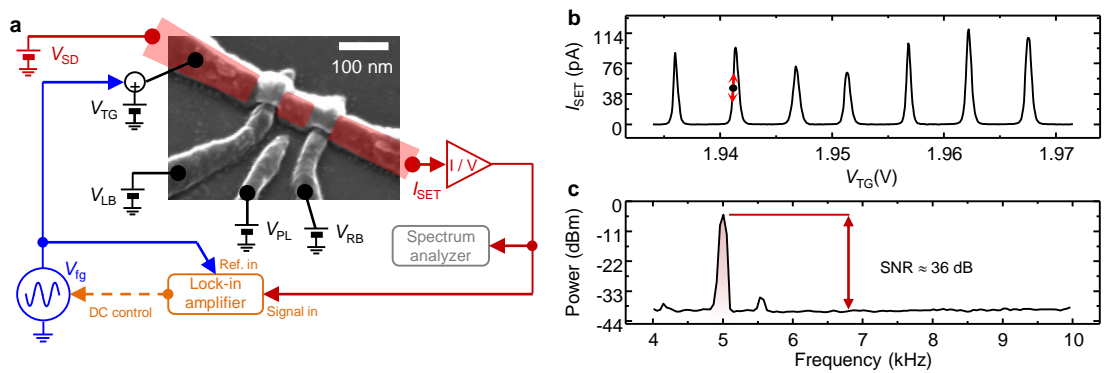


Figure 2.5: Charge sensitivity measurement of the Si MOS SET. **a**, Experimental setup for performing the charge sensitivity measurements on the SET. All of the electronics shown are situated at room temperature. In the measurement we have employed feedback, where the output current signal from the SET I_{SET} , which is modulated at the signal frequency f , is fed to a lock-in amplifier. The result of the lock-in measurement is monitored and the DC offset of the signal generator adjusted until the lock-in signal is maximized, resulting in a bias point on the shoulder of a Coulomb peak (as indicated in **b**). **b**, Top gate voltage scan whilst monitoring I_{SET} to show the sharpness of the Coulomb peaks. The black dot marks the bias point at which the charge sensitivity measurements were performed. The sinusoidal signal applied to the top gate causes a small modulation about this point, as indicated by the red arrow. **c**, FFT of I_{SET} in response to a 5 kHz, 125 μ V peak excitation signal, taken with a spectral analyzer using a 48 Hz resolution bandwidth B and a system bandwidth of 50 kHz.

applied to the device during readout. The RF-SET sensitivities quoted above are obtained when the source-drain RF excitation is of the order of the SET charging energy [100]. This excitation will couple to the SET island, rapidly modulating the electrochemical potential (see Chapter 3) and causing a loss of spin selectivity. Instead we make use of a much simpler DC-SET and a low-noise room-temperature transimpedance amplifier (Femto DLPCA-200) to achieve similar sensitivities and with a measurement bandwidth of up to 120 kHz [86].

We measure the charge sensitivity of the SET using the experimental setup outlined in Fig. 2.5a. Scanning V_{TG} whilst monitoring the current through the SET I_{SET} produces the characteristic Coulomb oscillations of Fig. 2.5b. The greatest sensitivity is achieved by biasing the SET on the shoulder of a Coulomb peak (as indicated in Fig. 2.5b). We apply a small sinusoidal excitation at a frequency of $f = 5$ kHz and with a peak amplitude of $V_{\text{pk}} = 125$ μV to the TG about the DC bias point. This excitation causes a modulation of I_{SET} , which is fed to a spectrum analyzer to obtain the fast Fourier transform (FFT) shown in Fig. 2.5c. To ensure we are tuned at the most sensitive point, we implement a feedback loop where I_{SET} is also input to a lock-in amplifier that has been synchronized to the 5 kHz TG signal. The output of the lock-in amplifier gives the differential conductance $\delta I_{\text{SET}}/\delta V_{\text{TG}}$, which we maximize by controlling the DC offset of the excitation signal. The spectrum of Fig. 2.5c was recorded with a 48 Hz resolution bandwidth (B) and indicates a signal-to-noise ratio (SNR) of 36 dB. The total input capacitance seen by the amplifier is estimated to be ≈ 400 pF (dominated by the nominal capacitance of the drain cable), such that the input voltage noise of the amplifier produces a corresponding input current noise of ≈ 160 pA RMS within a 50 kHz detection bandwidth. We can calculate

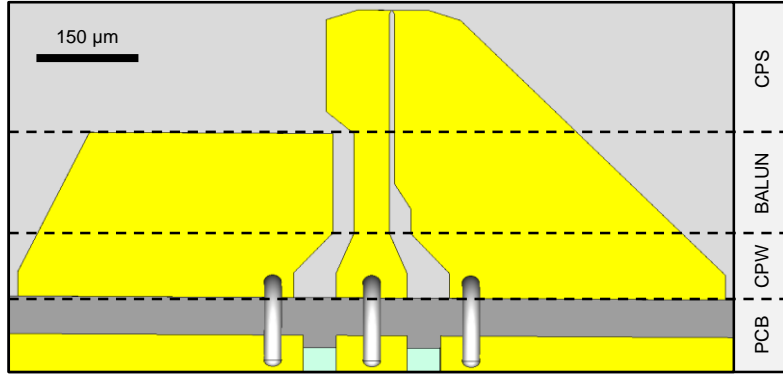


Figure 2.6: Sketch of the broadband transmission line. Shown are the Al bond wires that connect the transmission line to the gold-plated printed circuit board, and the balun transition that converts the coplanar waveguide to coplanar stripline.

the charge detection sensitivity of our SET using [101]:

$$\begin{aligned}\delta q &= \frac{\Delta q}{\sqrt{B} \times 10^{SNR/10}} \\ &= \frac{(V_{pk}/\Delta V_{TG}) e/\sqrt{2}}{\sqrt{B} \times 10^{SNR/10}}\end{aligned}\quad (2.6)$$

where Δq is the TG excitation amplitude in e_{RMS} and ΔV_{TG} is the difference in V_{TG} between consecutive Coulomb peaks. From Eq. 2.6 and using the parameters described above, we find a sensitivity of $\delta q \approx 4 \times 10^{-5} e/\sqrt{\text{Hz}}$, measured at 5 kHz and with a 50 kHz detection bandwidth.

2.4 Microwave Transmission Line

The oscillating magnetic fields used to drive electron and nuclear spin flips are generated through a broadband on-chip loop [102]. The loop consists of an aluminium short-circuited coplanar transmission line, fabricated on the silicon chip. The short-circuit forms a tapered loop, located ~ 150 nm from the spin readout

device. The design of the on-chip coplanar transmission line maximizes current flow at the loop over a wide range of frequencies. It contains a coplanar waveguide to coplanar stripline transition, similar to the one analyzed in [103], but carefully scaled and tapered to accommodate the chip and device dimensions (see Fig. 2.6). In order to maximize the frequency range of operation, the line is matched in impedance to the output of the microwave source; a high-frequency coaxial cable is used to transmit signals from the source to the device; an SK connector is soldered directly onto a matched coplanar waveguide on a high frequency printed circuit board; this waveguide connects to the on-chip transmission line through short bond wires ($\sim 200 \mu\text{m}$) to minimize their effective inductance. This setup has been simulated and measured over frequencies from DC to 50 GHz [102], the results indicating adequate magnetic fields for spin resonance experiments.

In order to probe the connectivity of the transmission line, preliminary tests are performed which involve sensing the electrical component of generated fields using the nearby SET. Figure 2.7a shows the SET current I_{SET} in response to continuous wave (CW) microwaves applied at frequencies from 28-50 GHz. The device is biased on top of a Coulomb peak, which sets the baseline current level. At certain frequencies, the current through the SET increases as a result of the electrical fields emanating from the transmission line. The observed fluctuations in I_{SET} as a function of excitation frequency are likely caused by resonances in the coaxial line. These fluctuations diminish in intensity at higher frequency due to the increased attenuation of the line. Observing Coulomb oscillations as the top gate voltage V_{TG} is varied, whilst applying microwaves of differing powers at a frequency of $\nu = 50 \text{ GHz}$, produces the plots of Figs. 2.7b-c. Increasing the microwave power P produces a larger amplitude of the electric field, further

2.4. Microwave Transmission Line

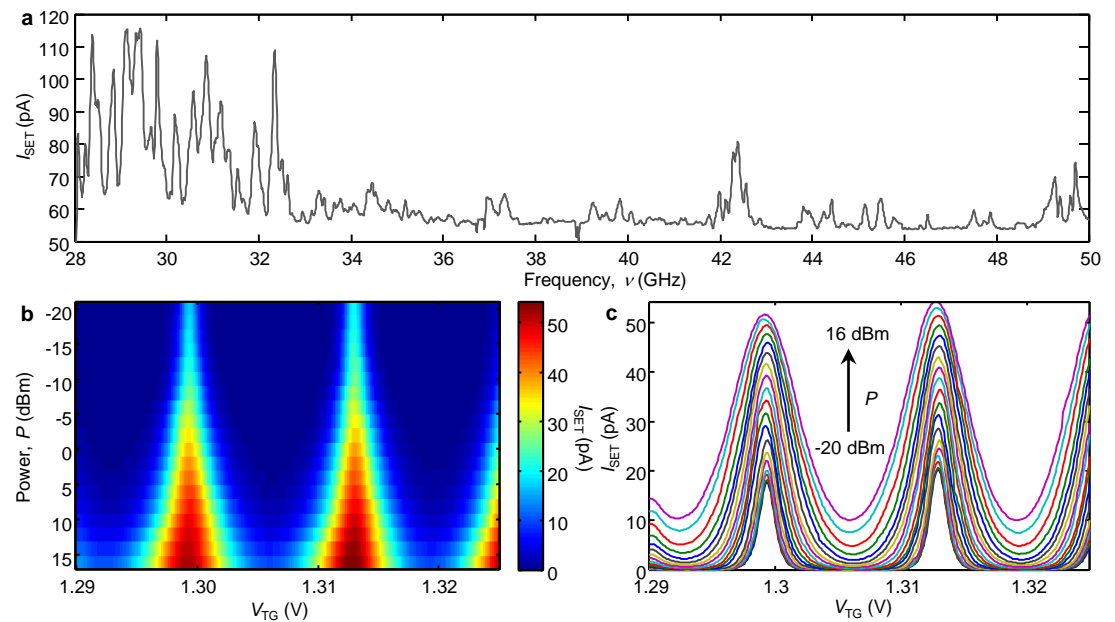


Figure 2.7: SET response to the transmission line. **a**, Current through the SET I_{SET} (whilst biased on top of a Coulomb peak) as continuous wave (CW) microwaves are applied to the line with a power of $P = -15$ dBm. **b**, 2D color plot of Coulomb peaks as a function of applied microwave power at $\nu = 50$ GHz. **c**, Individual scans of the Coulomb peak oscillations (I_{SET} vs V_{TG}) from **b**, clearly showing the broadening of the peaks with increasing microwave power.

2. Experimental Methods

broadening the Coulomb peaks.

Chapter 3

Electron Spin Readout

The size of silicon transistors used in microelectronic devices is shrinking to the level where quantum effects become important. While this presents a significant challenge for the further scaling of microprocessors, it provides the potential for radical innovations in the form of spin-based quantum computers and spintronic devices. An electron spin in Si can represent a well-isolated quantum bit with long coherence times because of the weak spin-orbit coupling and the possibility to eliminate nuclear spins from the bulk crystal. However, the control of single electrons in Si has proved challenging, and has so far hindered the observation and manipulation of a single spin. Here we report the first demonstration of single-shot, time-resolved readout of an electron spin in Si. This has been performed in a device consisting of implanted phosphorus donors coupled to a metal-oxide-semiconductor single electron transistor – compatible with current microelectronic technology. We observed a spin lifetime $T_1 \approx 6$ seconds at a magnetic field $B_0 = 1.5$ T, and achieved spin readout fidelity better than 90%. High-fidelity single-shot spin readout in Si opens the path to the development of a new generation of quantum computing and spintronic devices, built using the most important material in the semiconductor industry.

Parts of this chapter have been published in:

Morello, A., Pla, J. J., Zwanenburg, F. A., Chan, K. W., Tan, K. Y., Dehollain, J. P., Huebl, Möttönen, M., Nugroho, C. D., Yang, C., van Donkelaar, J. A., Alves, A. D. C., Jamieson, D. N., Escott, C. C., Hollenberg, L. C. L., Clark, R. G. and Dzurak, A. S. *Nature* **467**, 687-691 (2010).

3.1 Introduction

The electron spin of a single phosphorous (^{31}P) donor in silicon is a promising candidate for the qubit of a quantum computer [85, 87]. This is due to the extremely long coherence times demonstrated in this system - which exceeds seconds when the silicon crystal is purified in its ^{28}Si nuclear spin zero form [83] - and the potential for future scalability. In order to realize a quantum computer, the ability to measure individual qubits is prerequisite [104]. High-fidelity measurements [105] are desirable as this directly translates to a lower demand for system resources.

This chapter details a crucial step along the path to realizing QIP in silicon – the experimental demonstration of single-shot readout of an individual ^{31}P donor electron spin [86]. Measurement fidelities exceeding 90% were achieved, as well as long energy-relaxation times (qubit lifetimes) of up to ~ 6 seconds. The following presents a detailed account of these measurements and a description of the devices used in the experiments.

3.2 Device Architecture

The high effective mass and the valley degeneracy in silicon [106] require very tight confinement to isolate a single electron in a non-degenerate state. Phosphorus atoms in silicon naturally provide a sharp confining potential for their bound donor electron, and the quantum states $|\uparrow\rangle$, $|\downarrow\rangle$ of the electron spin ($S = 1/2$) form a natural qubit. In order to measure the donor electron spin states, we have fabricated devices which utilize an on-chip all-electrical detection method, based on nanostructures that are compatible with silicon metal-oxide-semiconductor (Si

3.2. Device Architecture

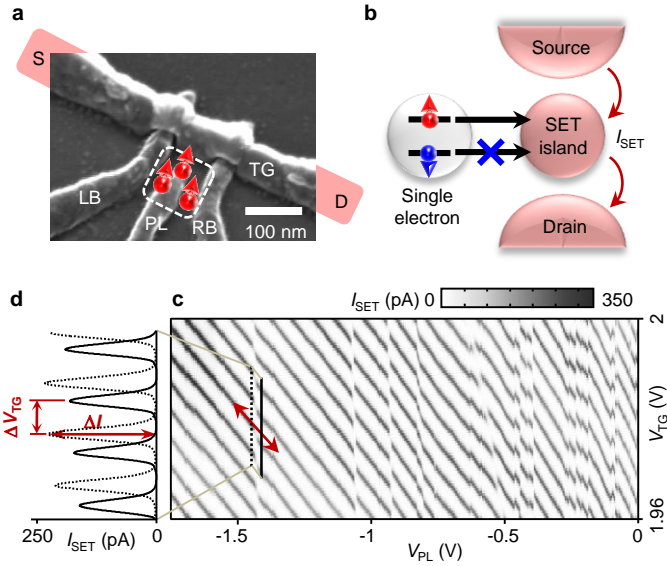


Figure 3.1: Electron spin readout device and charge stability diagram. **a**, Scanning electron micrograph of the spin readout device. The phosphorus donor implant area is marked by the white dashed box, with the donors colored red. The single-electron transistor (SET) is defined by the left and right barrier gates (LB and RB respectively) and the top gate (TG), whilst the plunger gate (PL) is used to control the electrochemical potential of the donor-bound electrons. Current through the SET is measured via the source (S) and drain (D) leads. **b**, Schematic depicting the spin-to-charge conversion process, where a single electron is displaced conditional on its spin state. **c**, SET current I_{SET} as a function of the voltages on the top and the plunger gates, V_{TG} and V_{PL} , at $B_0 = 0$. The lines of SET Coulomb peaks are broken by charge transfer events. The arrow on the transition at $V_{\text{PL}} \approx -1.4$ V shows the axis along which V_{TG} and V_{PL} are pulsed for the compensated time-resolved measurements discussed below. **d**, Line traces of I_{SET} along the solid and dashed lines in panel **c**. Ionizing the donor shifts the sequence of SET current peaks by an amount $\Delta V_{\text{TG}} = \Delta q/C_{\text{TG}}$, causing a change ΔI in the current. The charging energy of the SET is ~ 1.2 meV (see Section 2.3.2).

MOS) fabrication standards. The spin readout devices [85] (see Fig. 3.1a) consist of ion-implanted phosphorus donors [66], tunnel-coupled to a SET [94].

Historically, the most successful method of electrically measuring single electron spins has been spin-to-charge conversion [86, 107, 108]. For electron spins in solid state, this was first achieved in GaAs/AlGaAs quantum dots coupled to charge detectors [107]. By conditioning the displacement of the electron on its spin degree of freedom - typically by creating a situation where quantum mechanical tunneling of one of the spin states is energetically forbidden [86, 109], or by exploiting a difference in their tunnel rates [110] - the state can be detected by observing the resulting charge signal with sensitive nano-scale electrometers. Fig. 3.1b portrays the process of spin-to-charge conversion employed in our experiment. By utilizing a SET as both a reservoir of electrons for the phosphorus donor and also as a charge detector, our architecture is compact and capable of delivering a high signal-to-noise ratio for charge and thus spin state detection [86, 87].

3.3 Charge Stability Diagram

Our detection sensitivity is influenced by the charge transfer signal, $\Delta q/e$, which describes the shift in the SET electrochemical potential due to the displacement of the electron from the ^{31}P donor [85]. As the voltage on the plunger gate V_{PL} is varied, the implanted donors within the “active region” - a $30 \times 30 \text{ nm}^2$ area beneath the PL gate and between the two barrier gates, marked by the dashed box in Fig. 3.1a - undergo transitions from the neutral D^0 state to the ionized D^+ charge state. Due to the varying electric field and hence conduction band

3.3. Charge Stability Diagram

profile within this region [111], ionization will typically occur at a different value of V_{PL} for each donor. We observe the charge transfer signatures of the donors by measuring a charge stability diagram.

This is achieved by monitoring the SET current I_{SET} whilst scanning the top gate voltage (which generates Coulomb peak oscillations in I_{SET}) and then stepping the plunger gate (see Fig. 3.1c). Each time a charge center coupled to the SET changes its charge state, the sequence of SET current peaks breaks and shifts in gate voltage by an amount $\Delta V_{TG} = \Delta q/C_{TG}$, where Δq is the charge induced on the SET island and C_{TG} is the capacitance between island and top gate (Fig. 3.1d). Figure 3.1c shows a large number of charge transitions for $-0.7 < V_{PL} < 0$ V. Most of these transitions are irreproducible and hysteretic, and are probably caused by the charging/discharging of shallow traps at the Si/SiO₂ interface. The transitions for $V_{PL} < -0.7$ V, however, are stable and well reproduced even after several thermal cycles. Their number is consistent with the expected number of implanted donors in the active area (see following section), and they have been observed in a number of similar devices [112]. Considering the results of the spin lifetime measurements discussed below, it is likely that we are indeed observing transitions between D⁺ and D⁰ states of implanted ³¹P donors [113].

The charge stability diagrams are complicated by the fact that the PL gate can affect the transparency of the tunnel barriers in the SET. For large negative PL gate voltages the barriers can become completely opaque, stopping conduction through the SET. To mitigate this effect we perform a compensated sweep, where as V_{PL} is made more negative the barrier voltages (V_{LB} and V_{RB}) are gradually made more positive. This keeps I_{SET} relatively constant throughout the entire

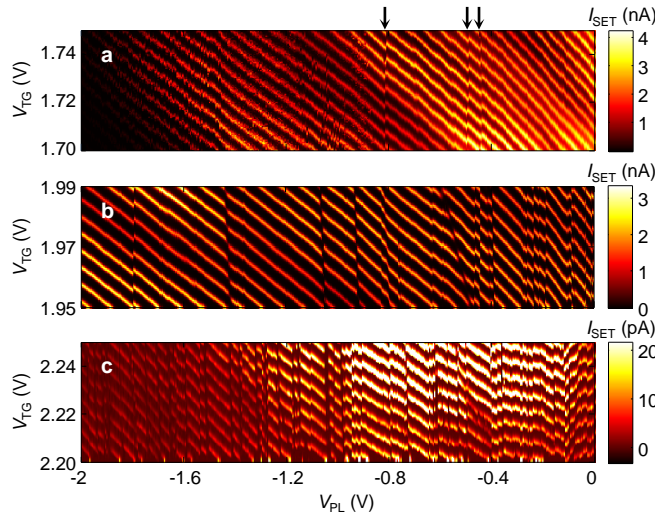


Figure 3.2: Charge stability diagrams for devices with different ion implantation fluences. a-c, Charge stability diagrams for spin readout devices with $\hat{N} = 0$ (a) $\hat{N} = 27$ (b) and $\hat{N} = 135$ (c) P ions implanted. In panel a, noise on the Coulomb peaks at the more negative V_{PL} region is likely the result of gate current leakage.

charge stability map.

3.4 Ion-Implantation

Implantation of the phosphorus ions was through a $90 \times 90 \text{ nm}^2$ aperture defined by e-beam lithography in a PMMA mask. The implantation energy was 14 keV, resulting in an average depth of $\sim 15 \text{ nm}$ below the Si/SiO₂ interface. Following implantation, a 5 s, 1000 °C rapid thermal anneal was performed to activate the donors and repair the implantation damage, reducing the likelihood of traps forming. By altering the ion fluence, we could control the maximum likelihood \hat{N} of phosphorus ions captured by the aperture. Fig. 3.2 shows charge stability diagrams from three different samples. The sample in panel a had no ion implantation at all, thus yielding $N = 0$. The other two samples had fluences chosen to produce maximum likelihoods of $\hat{N} = 27$ (panel b) and 135 (panel

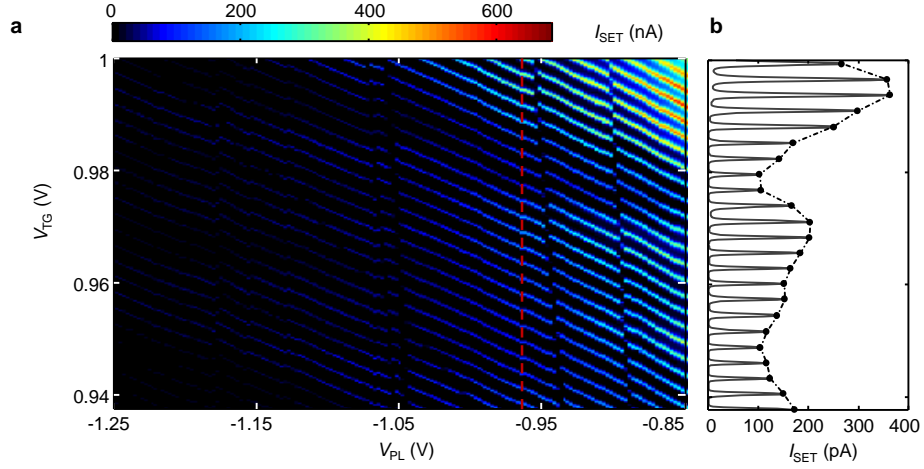


Figure 3.3: Modulation of the Coulomb peak current with SET electron occupation number. **a**, Charge stability diagram taken without compensation of the barrier gate voltages. Two features are apparent, the modulation of the Coulomb peak maximum current as the electron number in the SET is varied, and the gradual reduction in the overall current as V_{PL} is made more negative. **b**, Coulomb peak oscillations taken from the slice marked by the red dashed line in panel a. This plot highlights the fluctuation in Coulomb peak current as a function of top gate voltage, possibly due to the filling of different valley-orbit states in the SET island (see main text).

c) ions inside the aperture - corresponding to 3 and 15 ions within the “active region”. Figure 3.2a ($N = 0$) shows approximately four transitions, which we attribute to charge traps. Only the transitions marked by arrows were observed to be reproducible over several scans. Figure 3.2b and Fig. 3.2c display ~ 14 and 56 transitions respectively, in agreement with the larger values of \hat{N} . These results demonstrate that the ion-implantation has a detectable impact on the device characteristics, and in Section 3.10 we provide data which indicates that some of these transitions are indeed due to charge transfer events occurring between the neutral D^0 and ionized D^+ charge states of individual ^{31}P donors. The measurements described in this chapter were performed on two different devices, both implanted to achieve $\hat{N} \approx 3$ donors within the active region.

3.5 Features of the Charge Stability Diagrams

Figure 3.3a shows a charge stability diagram taken without compensation of the tunnel barriers - a technique that was employed in Figs. 3.1 and 3.2. As the plunger gate voltage is made more negative the conductance of the SET is gradually reduced, resulting in lower values of the on-peak/maximum I_{SET} . We also observe fluctuations in the Coulomb peak I_{SET} as the electron number on the SET is changed (i.e as V_{TG} is varied), producing the alternating regions of light and dark (high and low current) that are exemplified in the trace of Fig. 3.3b. One potential explanation for this modulation of I_{SET} with changing electron number is the fluctuating density of states (DOS) in the source and drain that results when the top gate voltage is varied. The top gate not only controls the electrochemical potential of the SET island, but it also controls the conduction band in the source and drain leads. This has the effect of shifting the quasi-one-dimensional (Q1D) DOS of the leads [114] with respect to the electrochemical potentials μ_S and μ_D (which are fixed by the external electronics), modifying the tunnel coupling of the leads to the island and thus the tunnel current [115]. The energy spacing of the Q1D subbands in the leads is expected to be of the order 0.3 meV, as measured in a device similar to the one here [114], which is much smaller than the range over which the Coulomb peak current modulation is observed to occur ($\sim 8E_C \approx 10\text{meV}$). This mechanism is therefore unlikely to account for the features of Fig. 3.3a.

Another explanation concerns shell filling of the single-particle states in the SET island [98]. Bulk silicon is an indirect band gap semiconductor with six degenerate conduction band minima (or valleys). As we add electrons to the SET island, they fill into different valley-orbital states [116]. These states will

exhibit different wavefunctions [98] with varying couplings to the source and drain reservoirs, producing different Coulomb peak tunnel currents I_{SET} . This could explain the seemingly random modulation of I_{SET} with SET electron number as observed in Fig. 3.3. The regions of like current could be explained by those states having similar orbital mixing.

3.6 Definition and Properties of Special Device Bias Points

The method of spin-to-charge conversion we employ in our experiments (Section 3.8) relies on the ability to detect in real-time the tunneling of an electron from a single donor. However, before performing real-time tunneling experiments, it is useful to explore the electrostatics of the donor-SET system. Every time a donor is tunnel-coupled to the SET island, the donor and the island effectively form a double quantum dot “in parallel” [117], and individual donors can be singled out by their unique value of V_{PL} at which ionization occurs. In order to shorten the notation in this chapter, we will often refer to the donor as “dot 1”, with occupation N_1 – here N_1 being 1 (i.e. in the D^0 charge state) or 0 (D^+) – and to the SET island as “dot 2”, with occupation N_2 . Figure 3.4a depicts a zoomed-in charge stability diagram in the vicinity of a charge transfer event. The charge configuration (N_1, N_2) of this double dot system has been superimposed on the scan, showing the change in the occupation of dot 1 and dot 2 as the plunger gate and top gate voltages are varied.

Fig. 3.4c shows a series of diagrams portraying the electrochemical potentials $\mu_{1/2}(N_1, N_2)$ of dots 1/2 for different device biasings (corresponding points

3. Electron Spin Readout

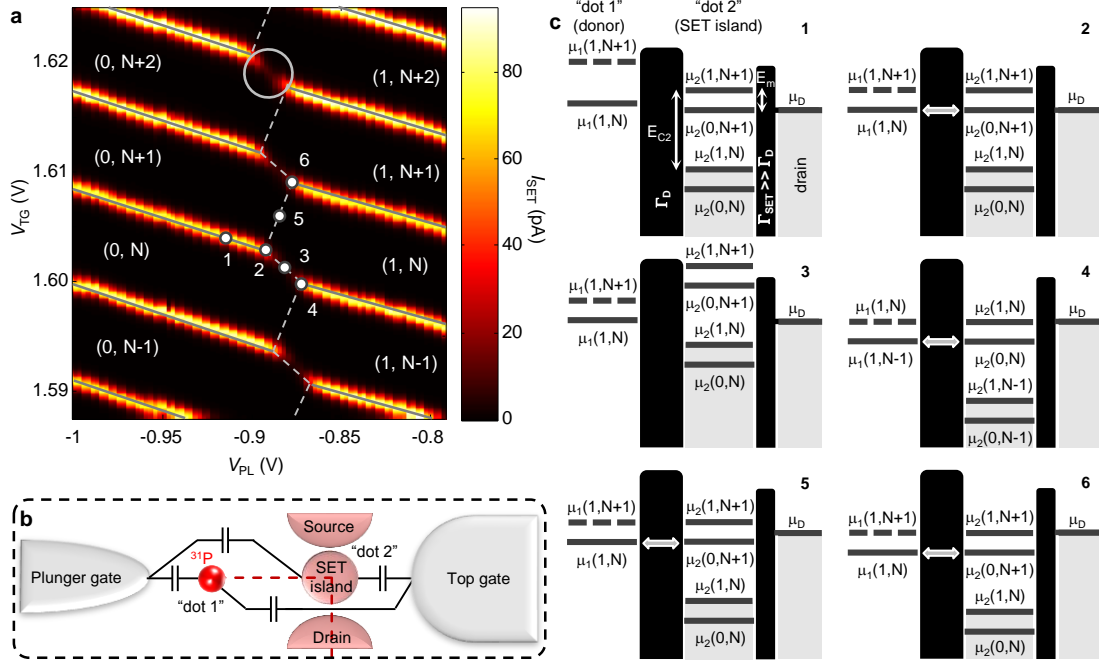


Figure 3.4: Close-up of a charge transition and electrochemical potential diagrams. **a**, Close-up stability diagram in the vicinity of a charge transfer event $D^0 \rightarrow D^+$ of a single ^{31}P donor. We use the notation (N_1, N_2) here to describe the charge occupation of dot 1 (the donor) and dot 2 (the SET island). The points marked 1-6 are described in panel **c**. **b**, Schematic of the cross capacitances involved with dot 1, dot 2 and their corresponding gates TG and PL. The capacitance between TG and dot 1 is responsible for a slight gradient of the overall transition, where the breaks in the Coulomb peaks occur at more negative values of V_{PL} as V_{TG} is raised. Likewise, the capacitance between PL and dot 2 is responsible for the non-zero slope of the Coulomb peaks with V_{PL} . The schematic is illustrative only for the purposes of displaying the relevant capacitive couplings, the barrier gates are not shown (see Fig. 3.1a). **c**, Electrochemical potential diagrams taken through the cross-section marked by the red dashed line in panel **b** for bias points 1-6 identified in panel **a**. The charging energy of dot 1 is $E_{C1} \approx 40$ meV, whilst $E_{C2} \approx 1.2$ meV. The tunnel rates between the dot 1 and dot 2 Γ_D and between dot 2 and the drain Γ_{SET} are such that $\Gamma_{\text{SET}} \gg \Gamma_D$, where the rate Γ_D is investigated in Section 3.7.

3.6. Definition and Properties of Special Device Bias Points

marked on Fig. 3.4a). The electrochemical potential landscape is taken through the device intersection traced by the red-dashed line in Fig. 3.4b. We define two potential ladders for each dot, separated by the mutual charging energy of the donor and SET island E_m (see Ref. 85 for further details). The situation in Fig. 3.4c panel 1 is perhaps the most simple, where the donor potential $\mu_1(1, N)$ is high enough that the donor remains in the 0 charge state and the SET island potential $\mu_2(0, N + 1)$ lies within the source/drain window (here only the drain potential μ_D is depicted). This arrangement produces sequential tunneling of electrons from the source to dot 2 to the drain. As we move towards the transition and V_{PL} is made more positive, the electrochemical potential of dot 1 is lowered. However, a finite cross-capacitance between the plunger gate and dot 2 (see Fig. 3.4b) causes μ_2 to also be lowered, necessitating a decrease in V_{TG} to keep $\mu_2(0, N + 1)$ within the source/drain bias window. This results in the non-zero slope of the Coulomb peaks with V_{PL} as is apparent in the charge stability diagrams. Following the Coulomb peak from bias point 1 to point 2 lowers the potential of dot 1, whilst keeping the μ_2 ladder fixed. Panel 2 shows the case where the transition has been intersected from the side where the donor is initially ionized. Here the electrochemical potentials $\mu_1(1, N)$ and $\mu_2(0, N + 1)$ are resonant and lie within the bias window. If dot 1 is in the 0 charge state, conduction of electrons will occur through the SET via $\mu_2(0, N + 1)$. However, the $(N + 1)$ th electron on dot 2 can tunnel through to dot 1 (in a time $1/\Gamma_D$, defined by the tunnel barrier) leaving the donor in the D^0 charge state. The relevant level for SET conduction is now $\mu_2(1, N + 1)$, which lies outside of the bias window. After some time $(1/\Gamma_D)$, the electron from dot 1 will tunnel back onto dot 2, once again leaving the system in the $(0, N + 1)$ charge state and admitting

a current through the SET. The result is a random telegraph signal in I_{SET} .

Point 3 is at the boundary between $(0, N)$ and $(1, N)$, where $\mu_1(1, N)$ lies within the source/drain bias window. Here we expect that no current should flow through the SET. However, we do sometimes observe a small current (of order 10 pA) in this region. A well-visible example is highlighted in the large gray circle in Fig. 3.4a. To understand the origin of this spurious current, we need to recall that the measurement is performed by fixing V_{PL} and sweeping V_{TG} , i.e. along a vertical line in the diagram. Notice however that, due to cross-capacitance, the charge transitions at different N do not lie along a vertical line. Consider now a scan that touched point 2. Moving further up in V_{TG} , we enter the $(0, N+1)$ charge state. Going vertically up, we do not reach the equivalent of point 2, but we cross the $(0, N+1)$, $(1, N+1)$ boundary on the right-hand side of the triple point. Ideally, what should happen while crossing that boundary is that an electron should occupy the donor, while leaving the SET in Coulomb blockade. However, loading an electron onto the donor is not instantaneous – it requires waiting the donor tunnel time. In this particular case, the relevant time is not the straightforward donor-SET tunnel time, because the SET potential is lower than μ_D (see panel 3 in Fig. 3.4c). Therefore, the loading of an electron onto the donor likely requires some higher-order – thus slower – co-tunneling process. If the donor is still ionized at the moment when V_{TG} reaches the value corresponding to the continuation of the $(0, N+1) – (0, N+2)$ boundary, the SET Coulomb blockade is lifted, and current can flow. This is why the “spurious current” features appear as continuations of the Coulomb lines, as highlighted in the gray circle. Bias point 4 (panel 4, Fig. 3.4c) is the reverse situation to panel 2, where conduction through the SET occurs when the dot 1 is in the 1 charge state

(neutral donor), via the $\mu_2(1, N)$ level ($\mu_2(0, N)$ is not within the bias window). In panel 5, the state switches between $(0, N + 1)$ and $(1, N)$, however, this just represents an internal redistribution of charge and no current is detected through the SET.

3.7 Donor-SET Resonant Tunneling Features

The duration over which the electron spin can be read and reset is ultimately limited by the tunnel barrier that exists between the donor and SET island. We can probe the electron tunnel rate by performing a pulsed spectroscopy measurement (Figs. 3.5a,b). To observe the time it takes to neutralize or “load” an electron onto the donor, we perform a simple experiment where we apply a square wave voltage pulse to the top and plunger gates. The first level of the square wave is fixed at bias point 1 of Fig. 3.4a (in order to initially ionize or “empty” the donor) and a variable second level starts just before point 2 and moves along the Coulomb peak well into the $(1, N)$ region (see Fig. 3.5a). In order to move the second level (or load phase) along the Coulomb peak, we utilize a compensation technique as described in Ref. 86. Here the voltage pulse is applied directly to the top gate, while it is inverted and amplified by a factor K before reaching the plunger gate (see Fig. 2.2). The gain K was carefully tuned to ensure that the SET operating point moved along the top of the SET current peaks (i.e. from bias point 1, past bias point 2, and into the $(1, N)$ region of Fig. 3.4c), as shown by the red arrow in Fig. 3.1c. Monitoring I_{SET} during the application of a single pulse sequence (for a particular value of the variable load voltage level) will produce a trace similar to that shown at the bottom of Fig. 3.5a, where the load

3. Electron Spin Readout

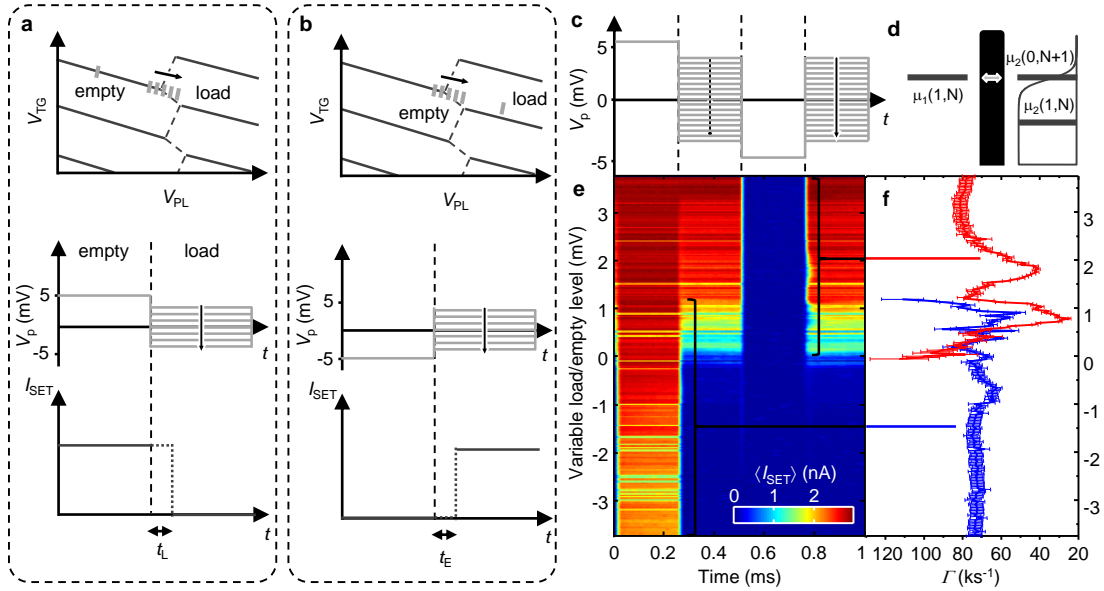


Figure 3.5: Tunnel rate measurements. **a-b**, Experiments for probing the load (**a**) and empty (**b**) rates of the donor electron. Top panel portrays the pulse sequence (light gray bars) used in the experiment (middle panel) and its relative position on the charge stability diagram. The bottom panel shows the expected I_{SET} response to the voltage pulse waveform. **c**, Pulse sequence for the combined load/empty rate experiment. **d**, In the experiments, $\mu_1(1, N) > \mu_2(0, N + 1)$ empties the donor and $\mu_1(1, N) < \mu_2(0, N + 1)$ loads an electron. As a result of the compensation applied to the top and plunger gates, the pulses move only the μ_1 electrochemical potential ladder and keep the μ_2 ladder fixed. Fermi broadening of the states in the SET island has also been depicted in this figure. The Fermi broadening modifies the available states to load from and empty to. **e**, Average SET current $\langle I_{SET} \rangle$ response to the sequence of panel **c**. The variable load and empty voltages are scanned together from 3.75 mV to -3.75 mV. **f**, Load and empty tunnel rates extracted from the averaged data in panel **e**. Rates are obtained from exponential fits of the form $\exp(-t\Gamma_{L/E})$ to the step edges indicated by the black brackets. Features in the data are discussed in the text.

3.7. Donor-SET Resonant Tunneling Features

time t_L is random and subject to the statistics of the tunneling electron. Taking many averages reveals an exponential decay curve (not shown), from which we may extract the loading tunnel rate Γ_L . We repeat a similar sequence to measure the empty tunnel rate Γ_E , where the first level of the square wave pulse is fixed well within the $(1, N)$ region, whilst the second level is again scanned from just before point 2 to inside the $(1, N)$ region (see Fig. 3.5b), along the Coulomb peak. Figure 3.5c shows a waveform where we have combined both measurements back-to-back to create a four-level pulse sequence. The resulting SET response as the variable load/empty voltage levels are scanned is shown in Fig. 3.5e, which contains the average I_{SET} for each voltage level over 32 measurements. The load and empty tunnel rates extracted from the step edges of the SET current response are displayed in Fig. 3.5f. This demonstrates the ability to load and empty the donor on timescales ranging from $10 - 100\mu\text{s}$.

Whilst the experiment of Section 3.5 probed the change in tunnel coupling of the SET island to the leads as a function of the number of electrons in the SET island, here we are probing the variation in the tunnel coupling between the donor and SET as the donor level μ_1 is moved with respect to the stationary electrochemical potential of the island μ_2 (see Fig. 3.5d). We observe clear features in the tunnel rates of Fig. 3.5f, and similar results are obtained from measurements on different electron numbers in the SET island (i.e. by moving up or down to different Coulomb peaks in the top panels of Figs. 3.5a,b). The modulation in the rates is very unlikely to be related to the discrete nature of the single-particle states in the SET island due to the energy scale over which they occur. Using the lever arm $\alpha \approx 0.3$ (extracted from the electron temperature measurements in Section 3.9) to convert the applied gate voltage into energy

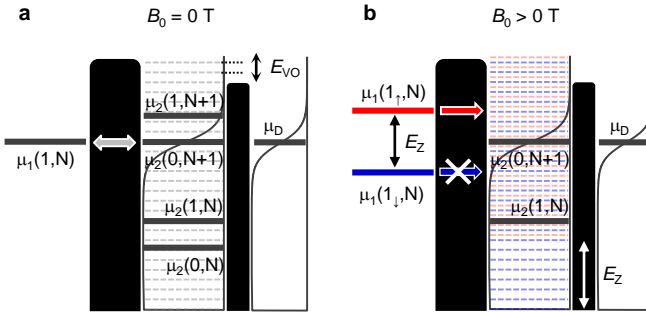


Figure 3.6: Readout non-idealities. **a**, Electrochemical potential diagram showing the readout biasing and the experimental non-idealities. The thin dashed lines in dot 2 represent the valley-orbit state splittings in the SET island which will be populated according to the Fermi distribution (also shown). **b**, The situation when an external magnetic field B_0 is applied. The donor electrochemical potential splits into two states, $\mu_1(1_\downarrow, N)$ and $\mu_1(1_\uparrow, N)$, split by the Zeeman energy. The valley-orbit states in dot 2 also split by roughly the same amount, providing a near-continuum of mixed spin-up and spin-down states.

units, we find that the modulations occur over a $\sim 300\mu\text{eV}$ scale. This is comparable to the measured valley-orbit splittings in few-electron Si MOS quantum dot devices with considerably smaller lithographic dimensions [118–120]. We would expect the single-particle state energy spacings in our SET island to be much smaller than this. Therefore, our current hypothesis is that these modulations could arise from shell-filling effects, i.e. “clustering” of single-particle states that yield an enhanced or suppressed density of single-particle states as a function of energy. The modulation becomes more prominent when μ_1 is within $\sim 5k_{\text{B}}T_{\text{el}}$ of the Fermi level in dot 2 (where T_{el} is the electron temperature as measured in Section 3.9), consistent with the reduction in the available states to tunnel to/from (Fig. 3.5d).

3.8 Single-Shot Spin Readout

Having demonstrated the ability to acquire fast and sensitive time-resolved measurements of the donor charge state, and shown that the electron can be made to tunnel quickly into and out of the donor, we now proceed to measurements of the donor electron spin state. A spin readout experiment begins by tuning the DC bias voltage of the SET to point 2 in Fig. 3.4a. At this point the electrochemical potential of the donor μ_1 (we have dropped the charge state notation here for brevity) is resonant with the Fermi level in the SET island and within the source/drain window (see Fig. 3.4a). This tuning is preferred over that of Fig. 3.4c panel 4, since here the detector back-action is minimized, i.e. no current runs through the SET whilst the donor is neutral, reducing a potential source of noise that may act as a channel for qubit decoherence. By applying an external magnetic field of order $B_0 \approx 1$ T, the electrochemical potential μ_1 of the single electron splits into two levels, $\mu_{1\uparrow}$ and $\mu_{1\downarrow}$ (corresponding to the spin-up $|\uparrow\rangle$ and spin-down $|\downarrow\rangle$ states respectively) which straddle the Fermi level ($\mu_{1\uparrow} > \mu_2 > \mu_{1\downarrow}$) and are separated by the Zeeman energy $E_Z = g\mu_B B_0 \approx 120\mu\text{eV}$. The Zeeman energy splitting is set to be greater than the thermal broadening of the Fermi distribution in the SET island $5k_B T_{\text{el}} \approx 86\mu\text{eV}$ (where the electron temperature $T_{\text{el}} = 200$ mK is described in Section 3.9) and also greater than the valley-orbit splitting E_{VO} – which is expected to be $\ll 0.1$ meV [118]. An electrochemical potential diagram displaying the non-idealities of the Fermi broadening and the discrete nature of the states in the SET island is presented in Fig. 3.6a. Figure 3.6b shows the situation where the external magnetic field has been applied, which Zeeman-splits both the donor ground state as well as the valley-orbit states in the SET island. However, because of the small valley-orbit splitting relative

to the Zeeman energy, this appears to the donor as a near continuum of mixed spin states.

Ensuring the condition $E_Z > 5k_B T_{\text{el}} > E_{\text{VO}}$ means that, with high fidelity, only an electron in the $|\uparrow\rangle$ state will find empty states to tunnel into in the SET island, causing conduction through the SET (i.e. the ON-value of I_{SET}). A $|\downarrow\rangle$ electron has a high probability of remaining on the donor, giving the OFF-value of I_{SET} . We call the situation described in Fig. 3.6b the “readout position”, and by combining this with additional load and empty stages, we are able to detect in a single-shot measurement (by monitoring I_{SET}) the spin of the donor-bound electron. Figure 3.7a shows the voltage pulse sequence for such a measurement along with the corresponding electrochemical potential diagrams and I_{SET} response. In the first phase, both $\mu_{1\uparrow}$ and $\mu_{1\downarrow}$ are plunged well below the Fermi level in the SET island, loading either a $|\uparrow\rangle$ or $|\downarrow\rangle$ electron onto the donor after a time Γ_L^{-1} and producing zero current through the SET. In the second phase the biasing is brought to the “readout position”, where $\mu_{1\uparrow} > \mu_2 > \mu_{1\downarrow}$, resulting in one of two scenarios: (i) If the donor electron is $|\uparrow\rangle$ then tunneling takes place from the donor to the SET island in a time Γ_E^{-1} . The change in the local potential induced by the ionized donor is detected as an increase in I_{SET} . Since $\mu_{1\downarrow} < \mu_2$, a $|\downarrow\rangle$ electron tunnels back onto the donor at a later stage, returning I_{SET} to its off value. (ii) If the donor electron is $|\downarrow\rangle$, it remains trapped on the donor throughout the entire phase, with I_{SET} at its off value. Both scenarios leave the donor electron initialized spin-down with a high probability at the end of the read phase, and a spin-up electron is distinguishable from a spin-down electron by the existence of a pulse in I_{SET} . In the final phase, we set $\mu_{1\uparrow}, \mu_{1\downarrow} > \mu_2$ in order to remove the $|\downarrow\rangle$ electron and repeat the sequence again with a new electron loaded in a random

3.8. Single-Shot Spin Readout

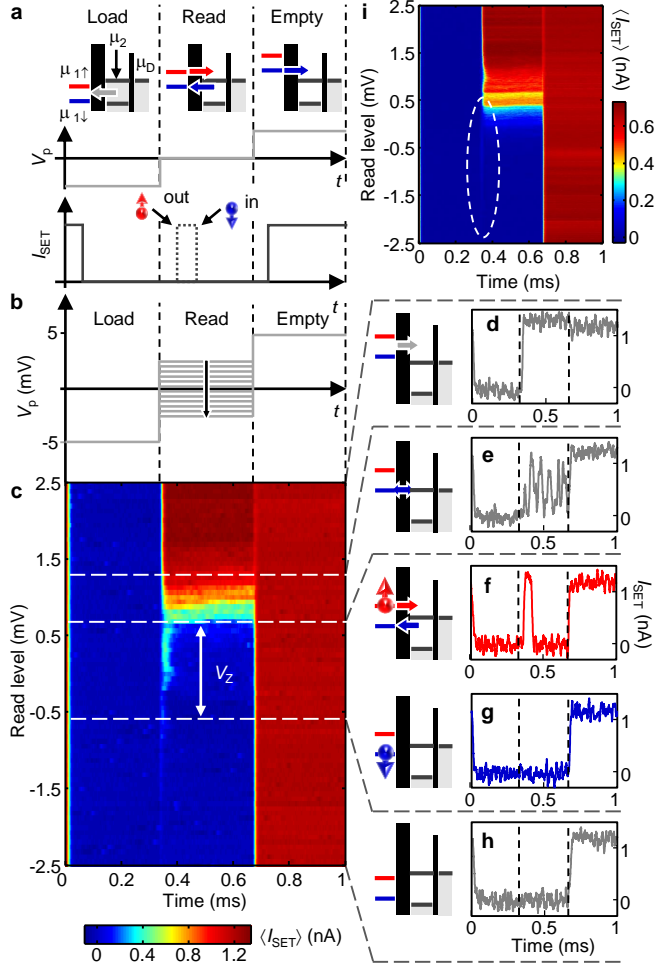


Figure 3.7: Single-shot electron spin readout experiment. **a**, Three level pulse experiment for measuring the spin state of the donor bound electron in a single shot. Top panel displays the electrochemical potential diagrams for each level, the middle panel shows the corresponding voltage pulse applied to the gates, and the bottom panel shows the expected current response of the SET. We first load an electron of random spin onto the donor, $\mu_{1\uparrow}, \mu_{1\downarrow} < \mu_2$. The readout position, $\mu_{1\uparrow} > \mu_2 > \mu_{1\downarrow}$, will produce a current pulse if the electron spin was $|\uparrow\rangle$ and produce no current through the SET if the electron spin was $|\downarrow\rangle$. Finally, we ionize the donor $\mu_{1\uparrow}, \mu_{1\downarrow} > \mu_2$ in order to repeat the sequence. **b**, Voltage waveform for performing an experiment to find the correct “readout” bias point. **c**, Average SET current $\langle I_{\text{SET}} \rangle$ response to the three level pulse experiment of panel **b**, while the read voltage level is varied. Experiment was performed in an external magnetic field of $B_0 = 5$ T. The region where a “bump” in current exists at the beginning of the read phase indicates the correct level for electron spin readout ($\mu_{1\uparrow} > \mu_2 > \mu_{1\downarrow}$). The length of the bump V_Z is proportional to the Zeeman energy splitting E_Z . **d-h**, Sample single shot traces of I_{SET} for different read voltage levels, as described in the main text. **i**, $\langle I_{\text{SET}} \rangle$ response to the three level pulse experiment of panel **b** with $B_0 = 0$ T. The white dashed oval encircles the induced current bump that results from pulsing directly on the top gate which has nothing to do with detection of $|\uparrow\rangle$ electrons.

spin state.

Finding the correct voltage level for the read phase is achieved by performing the pulse spectroscopy measurement detailed in Figs. 3.7b-h. Here we repeat the experiment outlined in Fig. 3.7a for different read voltages (using the voltage waveform of Fig. 3.7b), taking 128 single-shot traces of the I_{SET} response at each point and plotting the average current $\langle I_{\text{SET}} \rangle$ (Fig. 3.7c). We start with a voltage that ensures $\mu_{1\uparrow}, \mu_{1\downarrow} > \mu_2$ and observe a large current running through the SET, as exemplified by the single-shot trace of Fig. 3.7d. As the read level is lowered, the donor electron spin-down state comes into resonance with the Fermi level in the SET island ($\mu_{1\downarrow} \approx \mu_2$) which produces a random-telegraph-signal (RTS) in I_{SET} as spin-down electrons randomly tunnel (sequentially) on and off of the donor (Fig. 3.7e). Further lowering the voltage leads to the correct readout regime, where we observe I_{SET} traces that exhibit either a single current pulse near the beginning of the read phase (Fig. 3.7f), or zero current throughout the entire phase (Fig. 3.7g). The detection of spin-up electrons manifests in the average current plot as a light blue line at the beginning of the read phase. For lower read voltages still, we eventually reach the condition $\mu_{1\uparrow}, \mu_{1\downarrow} < \mu_2$ where spin readout is no longer possible and the signal disappears (Fig. 3.7h). A notable feature of this final region is the existence of a smaller/narrower bump at the load/read phase boundary. This feature is much more prominent in the color plot of Fig. 3.7i, which is the same experiment performed in a zero external magnetic field. Without the additional spin-up signal, this feature can be seen to run the entire length of Fig. 3.7i and also reduce in intensity as the read voltage is decreased. This artifact is a consequence of the compensation scheme we employ, where an attenuated and inverted copy of the readout pulse waveform is applied

3.8. Single-Shot Spin Readout

directly to the top gate, in order to keep the electrochemical potential ladder of the SET island fixed relative to that of the donor. The artifact arises from the charge induced by the top gate into the source contact upon pulsing. Assuming a parallel plate capacitor model, the top gate has a ≈ 20 fF capacitance to each of the source and drain. Using an electronic circuit simulation software package (PSpice) and entering all relevant capacitive and resistive components from the device/measurement setup, we are able to accurately recreate both the duration and size of the induced current pulse. The reduction in the height of the pulse as the difference in the load and read voltage levels is decreased, as observed in Figs. 3.7c and i, is simply the result of a smaller dV_p/dt being applied to the top gate.

The length of the spin-up signal in Fig. 3.7c gives a measure of the Zeeman splitting V_Z . However, an accurate extraction of the Zeeman energy from this measurement is complicated by the fact that the spin-up signal is convoluted in part with the end of the RTS region. We perform a different three-level pulse experiment, where instead of scanning the read voltage, we fix it at the readout position (as determined from Fig. 3.7c) and vary the load voltage (Fig. 3.8a). The resulting $\langle I_{\text{SET}} \rangle$ versus load voltage scan is shown in Fig. 3.8b. We begin with a load voltage such that $\mu_{1\uparrow}, \mu_{1\downarrow} > \mu_2$ (Fig. 3.8c) and the donor remains ionized throughout the load phase, the electron being loaded instead at the read level in the $|\downarrow\rangle$ state. Lowering the load voltage eventually provides the biasing that ensures $\mu_{1\downarrow} < \mu_2 < \mu_{1\uparrow}$ (Fig. 3.8e) and the donor electron is initialized $|\downarrow\rangle$ during the load phase. This experiment is relevant from a quantum information perspective. It shows that it is possible to initialize the spin to its ground state by means of electrical pulses, on a time scale determined by the electron tunnel

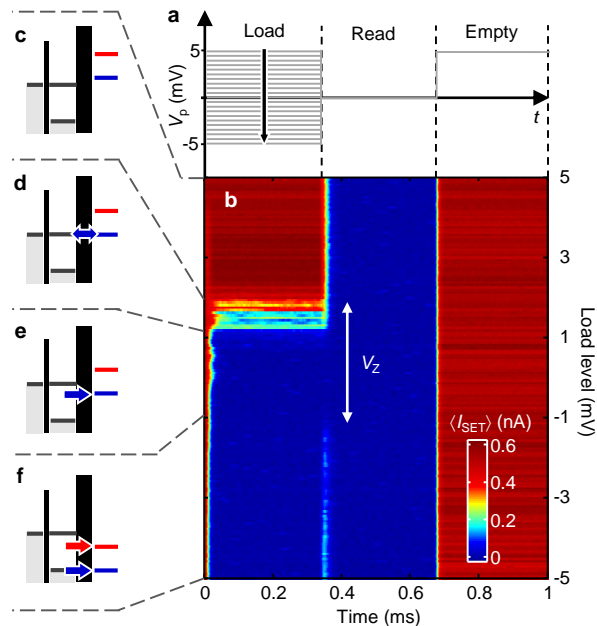


Figure 3.8: Three level pulse experiment with variable load voltage. **a**, Three level pulse experiment, where the read level is fixed at readout $\mu_{1\downarrow} < \mu_2 < \mu_{1\uparrow}$ and the load level is varied. **b**, $\langle I_{\text{SET}} \rangle$ response to the waveform of panel **a** as the load voltage is scanned from +5 to -5 mV. **c**, When the load voltage is too high, the electron is loaded in the read phase in the $|\downarrow\rangle$ state. **d**, During the load phase, $|\downarrow\rangle$ electrons tunnel back and forth between the donor and SET island. **e**, Here we deterministically load $|\downarrow\rangle$ electrons in the load phase, as a result the spin-up signal disappears from the read edge. **f**, Both $|\downarrow\rangle$ and $|\uparrow\rangle$ electron states can be loaded in this region, and the bump indicating spin-up readout returns to the beginning of the read phase.

3.8. Single-Shot Spin Readout

time $\Gamma_L^{-1} \approx 10\mu\text{s}$. This means it is not necessary to wait a time $\sim T_1$ – which can approach one second, as shown in Section 3.10 – to have a well-defined initial spin state. Figure 3.8f describes the situation when both spin states are lowered below the Fermi level during the load phase, providing a chance of initializing the electron $|\uparrow\rangle$. The readout signal consequently appears at the beginning of the read phase here, providing a more clear measure of the Zeeman splitting.

One complicating factor in extracting the Zeeman energy from Fig. 3.8b is that the signal is corrupted by the induced bump from pulsing on the top gate. We have solved this issue by modifying the previous experiment to add an additional “plunge” phase in between the load and read stages (Fig. 3.9a). This acts to provide a constant step (and therefore a constant pulse-induced current bump) at the readout boundary across all of the load voltages. The plunge voltage is chosen such that $\mu_{1\uparrow}, \mu_{1\downarrow} < \mu_2$. For the high load levels (Fig. 3.9c), no electron is loaded because the donor electrochemical potentials during the load phase are higher than that of the SET, for both spin states. An electron with random spin is then loaded during the plunge phase, and yields the characteristic peak of $\langle I_{\text{SET}} \rangle$ at the beginning of the read pulse (as depicted in Fig. 3.9b), due to the current pulses caused by $|\uparrow\rangle$ electrons. When the load level becomes comparable with the read level (Fig. 3.9e), then $\mu_{1\downarrow} < \mu_2 < \mu_{1\uparrow}$ and only $|\downarrow\rangle$ electrons can be loaded. The subsequent plunge pulse has no effect, since a $|\downarrow\rangle$ electron has already occupied the donor. Accordingly, we measure no spin-up signals during the read phase. Further lowering the load level (Fig. 3.9f) yields $\mu_{1\downarrow}, \mu_{1\uparrow} < \mu_2$ and allows the loading of both spin states, as revealed by the reappearance of spin-up signals in the read phase.

The voltage range V_Z where only spin-down electrons are loaded corresponds

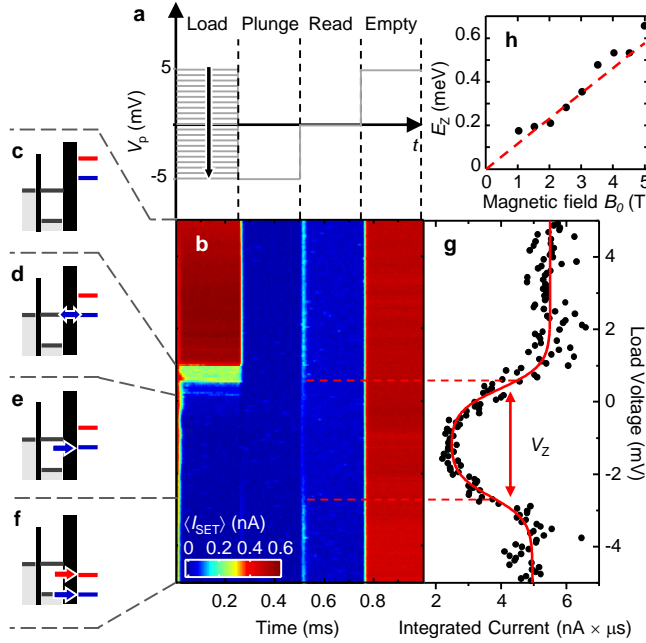


Figure 3.9: Four-level pulsing sequence for deterministic loading of the spin-down state and accurate extraction of the Zeeman splitting. **a**, The load level is scanned from +5 to -5 mV. A plunge phase at $V_p = -5$ mV is introduced to ensure that the step before the read phase remains constant. **b**, $\langle I_{SET} \rangle$ as a function of time and of the V_p level during the load phase, with 256 averages, $B_0 = 4$ T and 30 kHz bandwidth. **c**, High load level: The high $\langle I_{SET} \rangle$ signals that no electron is loaded during the load phase, but is loaded instead during the plunge region, in either the $|\downarrow\rangle$ or $|\uparrow\rangle$ state. Some $|\uparrow\rangle$ states are then detected during the read phase. **d**, Load level such that $|\downarrow\rangle$ electrons tunnel on and off the SET island. At the end of the load phase either a $|\downarrow\rangle$ electron will occupy the donor, or it will be ionized, with an electron of random spin then being loaded in the plunge phase. **e**, Load level comparable to read: Only $|\downarrow\rangle$ states are loaded. No $|\uparrow\rangle$ states detected, confirming the validity of the readout method. **f**, Low load level: Both states can be loaded, and detected accordingly. **g**, $\langle I_{SET}(t) \rangle$ integrated over the spin-up signal at the read edge, as a function of the load voltage level. Fit through the data is a double (back-to-back) Fermi distribution function. **h**, Zeeman splitting E_Z of the electron spin versus magnetic field B_0 . E_Z is calculated using the V_Z extracted from the plot of panel **g**, by converting it to energy units with the α value obtained in Section 3.9. The data are in good agreement with the values calculated for $g = 2$ electron spins in silicon (dashed line).

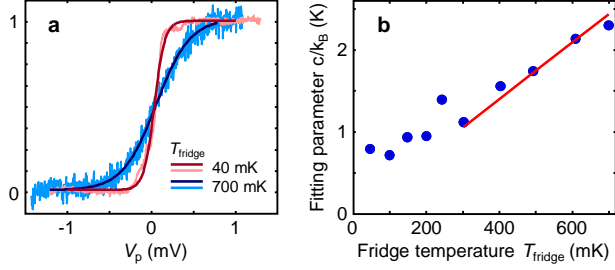


Figure 3.10: Electron temperature and lever arm calibration. **a**, $\langle I_{SET} \rangle$ resulting from a triangular wave (applied to the top and plunger gates) swept between -1.25 and $+1.25$ mV, as a function of the V_p level at fridge temperatures of 40 and 700 mK. **b**, Fitting parameter, c/k_B , versus fridge temperature, T_{fridge} . The inverse of the slope of the red line through the points at $T > 250$ mK yields a lever arm $\alpha \approx 0.28$.

to the energy interval where $\mu_{1\downarrow} < \mu_2 < \mu_{1\uparrow}$. Therefore, this experiment yields the Zeeman energy splitting of the electron spin, $E_Z = g\mu_B B_0$, after converting the voltages into energies through the expression $E_Z = \alpha e V_Z$, where $\alpha \approx 0.3$ and $e = -1.6 \times 10^{-19}$ C is the elementary charge. We integrate $\langle I_{SET} \rangle$ at the read edge over a small period of time that covers the spin-up induced current pulse, and plot in Fig. 3.9g the integrated current as a function of the load voltage. The resulting trace is fit with back-to-back Fermi distributions – where the Fermi distribution at higher (lower) load voltages is caused by $\mu_{1\downarrow}$ ($\mu_{1\uparrow}$) crossing the Fermi level in the SET island – and V_Z is found. The pulse-induced current bump is constant over all load voltages here and simply manifests as an offset in Fig. 3.9g. Evaluating the expression for E_Z above for the measurements at different magnetic fields, we find $E_Z(B_0)$ as shown in Fig. 3.9h. The field dependence of the measured E_Z is in good agreement with the calculated value for electron spins in silicon with gyromagnetic ratio $g = 2$, as highlighted by the dashed line.

3.9 Electron Temperature

To find both the lever arm α and electron temperature T_{el} , we apply compensated triangular waves to the top and plunger gates, and measure the average current through the SET at $B_0 = 0$ T over many sweeps. The triangular wave causes the biasing of the device to proceed from point 1 in Fig. 3.4a, along the Coulomb peak, and into the $(1, N)$ charge region. Accordingly, $\langle I_{\text{SET}} \rangle$ goes from high to low or vice versa when crossing the charge transition point. Figure 3.10a portrays the $\langle I_{\text{SET}} \rangle$ response to the triangular waves at two different temperatures of the dilution refrigerator. The width of the transition in $\langle I_{\text{SET}} \rangle$ is proportional to the width of the Fermi distribution of electron states in the SET island. Thus we fit $\langle I_{\text{SET}} \rangle$ to the function

$$\langle I_{\text{SET}}(V_p) \rangle = \frac{a}{1 + \exp \left[\frac{eV_p - b}{c} \right]} + d \quad (3.1)$$

where a , b , c and d are fitting parameters. The fitting parameter c has units of energy; dividing c by the Boltzmann constant yields a parameter c/k_B , with units of temperature but including the lever arm α , which converts the applied voltage pulse to units of energy and is used in Section 3.8 to calculate the Zeeman energy. Repeating the experiment at different fridge temperatures and plotting the extracted c/k_B against T_{fridge} yields the data in Fig. 3.10b. At $T_{\text{fridge}} > 250$ mK, c/k_B is linear in temperature and can be written as $c/k_B = T_{\text{fridge}}/\alpha$. Therefore, the lever arm $\alpha \approx 0.28$ is found by taking the inverse of the slope of the best fit through these points (the red line in Fig. 3.10b). At $T < 250$ mK, c/k_B deviates from the linear behavior, indicating that the electron temperature in the SET island deviates from T_{fridge} , and saturates to a value $T_{\text{el}} \approx 200$ mK.

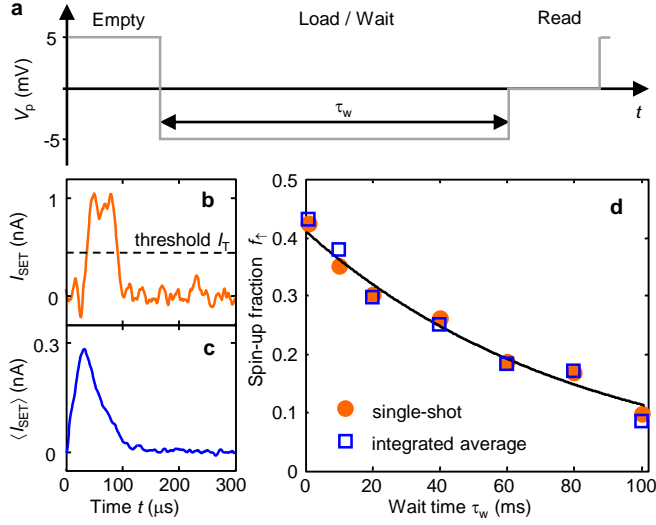


Figure 3.11: Single-shot vs. averaged spin lifetime (T_1) measurements. **a**, Pulse sequence for measuring the energy relaxation time T_1 of the electron spin. This sequence is identical to the spin readout experiment of Fig. 3.7a, but with a variable duration τ_w of the load phase. **b**, Example of single-shot trace during the read phase. A state $|\uparrow\rangle$ is counted when $I_{\text{SET}} > I_T = 0.45 \text{ nA}$ (dashed line). **c**, Average of 500 single-shot traces in the read phase. **d**, Spin lifetime (T_1) measurement taken with the two different methods introduced in panels **b** and **c**. The spin-up fraction $f_{\uparrow}(\tau_w)$ can be obtained by counting the $|\uparrow\rangle$ states in single-shot (dots) or by integrating $\langle I_{\text{SET}} \rangle$ (squares) within a window $0 < t < 100 \mu\text{s}$ of the read edge. Rescaling and normalizing $\langle I_{\text{SET}} \rangle(\tau_w)$ shows that the two approaches are equivalent and can be fitted by the same exponential decay (solid line) to reveal T_1 . Data taken on Device A at $B = 5 \text{ T}$.

3.10 Electron Spin Relaxation

Having demonstrated the ability to read out the electron spin state in single-shot, the spin energy relaxation rate T_1^{-1} can be obtained by measuring the fraction of spin-up counts f_{\uparrow} as a function of the wait time τ_w before the spin is read, as shown in Fig. 3.11a. f_{\uparrow} is observed to reduce with increasing τ_w because the excited state $|\uparrow\rangle$ relaxes to the ground state $|\downarrow\rangle$. The wait time dependence of f_{\uparrow} (Fig. 3.11d) is well described by a single exponential decay, $f_{\uparrow}(\tau_w) = f_{\uparrow}(0) \exp(-\tau_w/T_1)$, where T_1 is the lifetime of the spin excited state. However, we note that measuring T_1 does not strictly require single-shot readout. Since the spin-up current pulses

occur with the highest probability in a well defined time interval, the average current $\langle I_{\text{SET}}(t) \rangle$ has a Poissonian shape (Fig. 3.11c), and its integral is proportional to f_{\uparrow} . Figure 3.11d shows that the integral of $\langle I_{\text{SET}}(t) \rangle$ for $0 < t < 100 \mu\text{s}$ can be rescaled and superimposed with f_{\uparrow} as obtained from single-shot readout, and an exponential fit yields the same T_1 for both methods. The method of integrating the averaged current flowing through a quantum point contact has been used to measure the spin lifetime in Si/SiGe (Ref. 121) and Si/SiO₂ (Ref. 122) quantum dots, where the signal-to-noise ratio was not sufficient to achieve single-shot readout. Counting spin excited states in single-shot provides an absolute measure of f_{\uparrow} , but is otherwise equivalent to the averaged current method for T_1 measurements.

We have found the electron spin relaxation rate at different magnetic fields for both Device A (Fig. 3.12a) and Device B (Fig. 3.12b), with the resultant $T_1^{-1}(B_0)$ shown in Fig. 3.12c. Both devices display a $\propto B_0^5$ dependence in $T_1^{-1}(B_0)$, fits through the data sets are given in the figure caption. The longest spin lifetime achieved was on Device B at $B_0 = 1.5 \text{ T}$, where remarkably $T_1 = 6(2) \text{ s}$.

The spin-lattice relaxation rates for ³¹P donors in Si, in the temperature regime $T < 2 \text{ K}$ where only one-phonon processes are relevant, have been calculated by Hasegawa [123] and Roth [124] and is also discussed in a recent review on single electron spin relaxation in silicon [125]. Both calculations deal with a spin-lattice relaxation mechanism where the spin-orbit coupling is modulated by crystal strain. Because the strain breaks the equivalence of the 6 conduction band minima of silicon (“valleys”), it affects the anisotropy of the electron g -factor. The two models describe two different – both valid – ways in which the breaking of valley degeneracy influences the g -factor anisotropy, and give qualita-

3.10. Electron Spin Relaxation

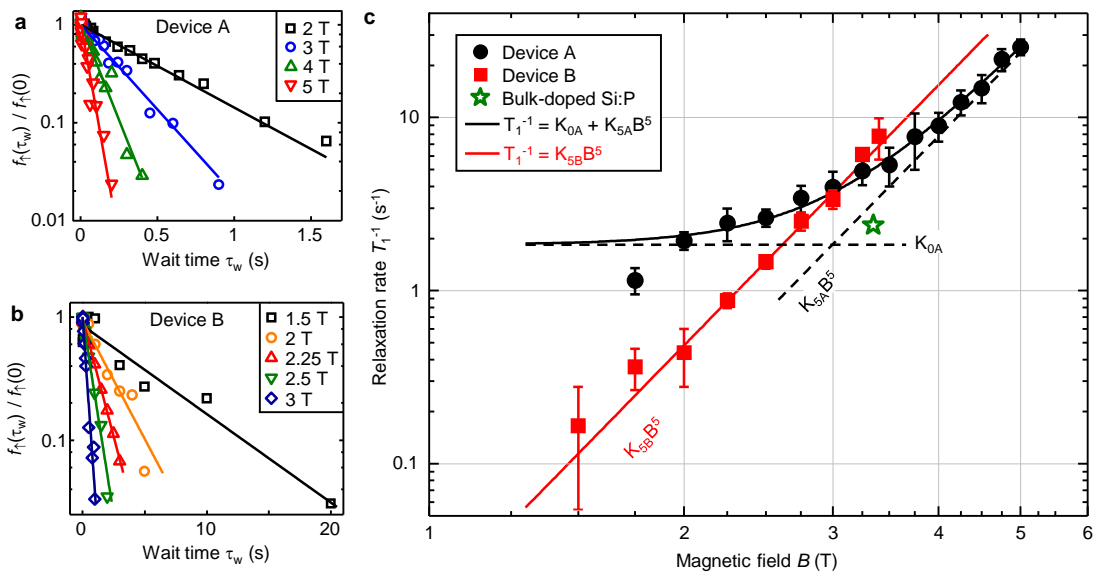


Figure 3.12: Spin relaxation rate magnetic field dependence. **a-b,** Exponential decays of the normalized spin-up fraction at different magnetic fields B_0 , for Devices A and B as indicated. **c,** Magnetic field dependence of T_1^{-1} . Error bars are 95% confidence levels. We find a best fit for the data of Device A of the form $T_1^{-1} = 1.84s^{-1} + 0.0076B^5s^{-1}T^{-5}$ (black solid line, sum of the dashed lines). The point at $B_0 = 1.75$ T is not included in this fit. The data for Device B follow $T_1^{-1} = 0.015B^5s^{-1}T^{-5}$ (red solid line). The green open star is a data point measured in a bulk doped Si:P crystal at $B_0 = 3.35$ T and $T = 5$ K (J. J. L. Morton, personal communication).

tively similar results but different angular dependencies. The Hasegawa “valley repopulation” model predicts no relaxation when $B_0 \parallel [100]$, while the “single valley” model of Roth yields a finite contribution for all field orientations. The magnetic field in our experiment is oriented along the [110] direction, thus both mechanisms give a contribution. A comprehensive discussion and experimental test of both relaxation mechanisms has been given by Wilson and Feher [126].

Both the above models have been written in the high-temperature limit, $k_B T \gg g\mu_B B_0$. The formula of Hasegawa [123], for example, reads:

$$T_1^{-1}(B_0) = f_{\text{Si}}(\theta, \phi) \frac{6}{5\pi} \left(\frac{g'\Xi}{3g\Delta E} \right)^2 \left(\frac{1}{\rho\nu_t^5} + \frac{2}{3\rho\nu_l^5} \right) \left(\frac{g\mu_B B_0}{\hbar} \right)^4 k_B T \quad (3.2)$$

$$= K_4 B_0^4 T \quad (3.3)$$

where $f_{\text{Si}}(\theta, \phi)$ is an angular factor of order unity, $g = 1.9985$ [76], $\Xi \approx -7$ eV is a parameter that describes the energy shift of the conduction band minima (“valleys”) due to a deformation of the crystal lattice, $g' = (g_l - g_t)/3$ describes the anisotropy of the g -factor along the principal axes of the effective mass tensor for each valley, ΔE is the energy difference between the first valley excited state and the ground state, $\rho = 2330 \text{ kg/m}^3$ is the density of Si, and $\nu_t = 5860 \text{ m/s}$ and $\nu_l = 8480 \text{ m/s}$ are the transverse and longitudinal sound velocities, respectively.

All the material (and donor) dependent properties can be condensed in a parameter K_4 which is explicitly independent of B_0 and T in the regime of interest. A B_0 -dependence of K_4 would arise if the wavelength of the emitted phonon became comparable with the Bohr radius of the donor wavefunction. However, this would require $B_0 \gg 50 \text{ T}$ for Si:P and is therefore not relevant here. The remaining $\propto B_0^4 T$ dependence contains a contribution $(1 + N_{\text{ph}}) \approx k_B T/g\mu_B B_0$, where

3.10. Electron Spin Relaxation

$N_{\text{ph}} = 1/[\exp(g\mu_{\text{B}}B_0/k_{\text{B}}T) - 1]$ is the Bose factor for the thermal occupation of the phonon modes with energy $g\mu_{\text{B}}B_0$. This factor is included to describe both spontaneous and stimulated emission of a phonon upon relaxation of the excited spin state.

The low- T limit of Eq. 3.2, $k_{\text{B}}T \ll g\mu_{\text{B}}B_0$, can be obtained by replacing $(1 + N_{\text{ph}})$ with 1, i.e. considering only spontaneous phonon emission in the derivation of $T_1^{-1}(B_0)$ (see e.g. Ref. 99), which becomes:

$$T_1^{-1}(B_0)|_{\text{low-}T} = K_4 \frac{g\mu_{\text{B}}B_0}{k_{\text{B}}T} B^4 T = K_5 B_0^5 \quad (3.4)$$

This is the $\propto B_0^5$ contribution to the relaxation rate we have found in our experiment (Fig. 3.12c). The B_0^5 dependence of Eq. 3.4 contains a contribution $\propto B^2$ from the phonon density of states as well as a contribution $\propto B$ from the high field/low temperature limit of the Bose factor, as described above. In Hasegawa's approach [123], the remaining B_0^2 contribution comes from time-reversal symmetry constraints [127]. The sharp confining potential of the donor causes a mixing of the valley and orbit degrees of freedom, resulting in a singlet ground state plus doublet and triplet valley-orbit excited states [88] (not including spin degeneracy). Time-reversal symmetry means that spin relaxation in the ground state occurs via a virtual transition to the doublet valley-orbit excited state (where the energy separation is of order $\Delta E \approx 10$ meV) – which is admixed with the ground state by spin-orbit coupling. This produces a matrix element $\propto g\mu_B B_0/\Delta E$, and hence a contribution of B_0^2 to the spin relaxation rate.

For the coefficients K_4 and K_5 the following relationship holds:

$$K_4 = \frac{k_B}{g\mu_B} K_5 \quad (3.5)$$

Feher and Gere [48] measured the T_1^{-1} of ^{31}P donors in a natural-isotope, bulk-doped ($n \sim 10^{16} \text{ cm}^{-3}$) Si crystal at $B_0 = 0.32 \text{ T}$ parallel to the [100] direction, down to $T = 1.25 \text{ K}$, obtaining $T_1^{-1} \approx 2 \times 10^{-4} \text{ s}^{-1}$, corresponding to a spin lifetime $T_1 \sim 1.4 \text{ hours}$ and a coefficient $K_4 \approx 0.015 \text{ s}^{-1}\text{T}^{-4}$. Using Eqs. 3.3 and 3.5, we can extrapolate the results of Feher and Gere to the low- T regime, obtaining $K_5 \approx 0.02 \text{ s}^{-1}\text{T}^{-5}$. This is higher by a factor ≈ 1.3 as compared to the single-spin results we obtained on Device B, and a factor ≈ 2.6 compared to Device A. As noted by Feher and Gere [48], when measuring such long relaxation times the presence of trace amounts of paramagnetic impurities can play an important role, and lead to the observation of artificially high relaxation rates.

The data point shown in Fig. 3.12c (J.J.L. Morton, private communication) was measured on a bulk Si:P crystal at $B_0 = 3.35 \text{ T}$ and $T < 5 \text{ K}$, yielding $T_1 = 0.42 \text{ s}$. This can be compared directly to the single-spin results, because it was attained in the low- T regime, $k_B T < g\mu_B B_0$. The bulk spin relaxation rate is in this case a factor ≈ 1.3 below the line $T_1^{-1}(B_0) = K_{5A} B_0^5$ of Device A, and a factor ≈ 2.6 below the line $T_1^{-1}(B_0) = K_{5B} B_0^5$ of Device B.

Equation 3.2 indicates that $T_1^{-1} \propto \Delta E^{-2}$, i.e. the spin lifetime is reduced when the valley-orbit ground and excited state splitting decreases. It has been shown that donors in gated nanostructures [128] can have ΔE values much lower than in bulk. Therefore the slight difference between our data and the bulk Si:P result, and the variability between the two devices we have measured, can be

3.10. Electron Spin Relaxation

accounted for by a variation of ΔE due to electric fields and proximity to the Si/SiO₂ interface.

The spin relaxation rate $T_1^{-1}(B_0)$ shown in Fig. 3.12c for Device A contains a field-independent contribution, $K_{0A} = 1.84(7) \text{ s}^{-1}$. We suggest that this contribution arises from spin diffusion, due to the dipolar coupling of the measured spin to the electron spins on neighboring ³¹P donors (mechanism depicted in Fig. 3.13). The device contains an expected 27 donors (Poisson statistics) in a $90 \times 90 \text{ nm}^2$ area. The dipolar coupling Hamiltonian contains a “flip-flop” term, which allows two spins to swap their orientation. Although this mechanism conserves the total energy of the spin system, when a spin-up electron loaded on the single donor under measurement undergoes a flip-flop with a neighboring spin, it will appear to have relaxed to the spin-down state if measured after some time.

In a natural-isotope silicon crystal, each donor site is subject to an inhomogeneous broadening of the local magnetic field due to the hyperfine coupling with ²⁹Si nuclei [87], with half-width $\langle \Delta\omega_I \rangle = g\mu_B\langle B_I \rangle/\hbar$, where $\langle B_I \rangle \approx 0.125 \text{ mT}$. $\langle B_I \rangle$ is much larger than the mutual dipolar field between electron spins at distances $> 10 \text{ nm}$, and has the effect of suppressing the energy-conserving flip-flops. An order of magnitude estimate of the flip-flop rate Γ_{ff} of two electron spins S at distance d can be obtained from a Fermi golden rule argument [129]:

$$\Gamma_{\text{ff}} \approx \frac{\pi}{2\langle \Delta\omega_I \rangle} M_{\text{ff}}^2 \quad (3.6)$$

$$M_{\text{ff}}^2 = \left(\frac{\mu_0}{4\pi\hbar}\right)^2 \frac{1}{12} S(S+1) g^4 \mu_B^4 \frac{(1-3\cos^2\theta)^2}{d^6} \quad (3.7)$$

where Eq. 3.7 represents the flip-flop matrix element in the dipolar Hamiltonian, dependent on the distance d and the angle θ that the vector joining the donors

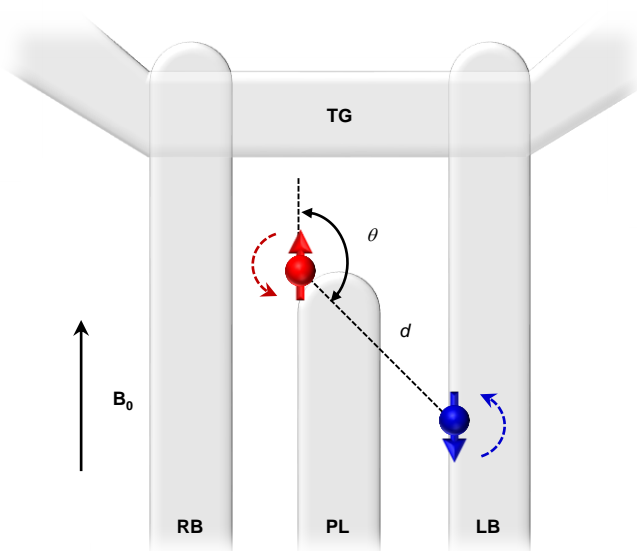


Figure 3.13: Electron spin flip-flop mechanism. Cartoon of the flip-flop mechanism to which we attribute the B_0 independent contribution to T_1^{-1} for Device A. This mechanism involves a flip of the $|\uparrow\rangle$ donor electron spin under measurement and a corresponding flop of another ^{31}P donor electron spin (which is in the $|\downarrow\rangle$ state). The flip-flop rate depends on the strength of the dipolar interaction between the donor and its neighbors. Here we have illustrated the simplified case of a single donor pair (separated by a distance d and at an angle θ with B_0).

3.11. Electron Spin Readout Fidelity

makes with the external field (see Fig. 3.13). The term $\pi/\langle\Delta\omega_I\rangle$ in Eq. 3.6 plays the role of a density of states, and the additional factor 2 in the denominator accounts for the effect of ^{31}P nuclei, which can have equal or opposite direction in the two donors. We can match the experimental value for Device A, $\Gamma_{\text{ff}} \approx 2 \text{ s}^{-1}$, by assuming $d = 24 \text{ nm}$ and averaging over θ . A more accurate estimate of Γ_{ff} would require summing the contributions of all neighboring donors, a detailed knowledge of their location, and whether they are neutral or ionized. Since this mechanism depends strongly on the mutual distance between implanted donors (i.e. $\Gamma_{\text{ff}} \propto 1/d^6$) as well as their relative orientations, one would expect the flip-flop rate to be highly sample-dependent – which could explain why we observe the field-independent contribution to the spin relaxation rate for Device A only.

Our result is incompatible with the known relaxation process for interface traps, which is dominated by the coupling to two-level fluctuators [130], yielding $T_1^{-1} \propto B_0^3$. A recent electron spin resonance experiment on shallow traps at the Si/SiO₂ interface [131] found $T_1 \approx 800 \text{ }\mu\text{s}$ at $T = 350 \text{ mK}$ and $B_0 = 0.32 \text{ T}$, i.e. 2 to 3 orders of magnitude shorter than our result, despite the much lower magnetic field. We conclude that the observation of $T_1^{-1} \propto B_0^5$ and the quantitative agreement with bulk Si:P data constitute a strong indication that we have measured the spin of a single electron bound to an implanted ^{31}P donor. The proximity of the donor to electrostatic gates and a Si/SiO₂ interface [132] could be responsible for the slight variability of T_1 but, importantly, does not substantially compromise the long spin lifetime of the donor-bound electron.

3. Electron Spin Readout

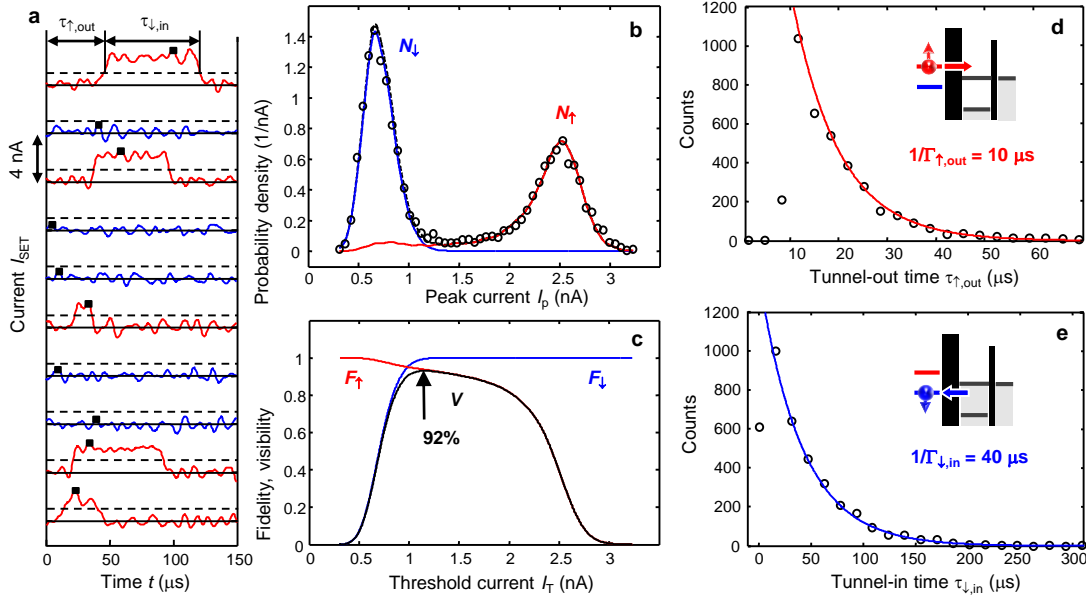


Figure 3.14: Readout fidelity and visibility. **a**, Examples of single-shot I_{SET} traces, each shifted by 4 nA for clarity, with $B_0 = 5$ T and 120 kHz bandwidth ($\sim 3\mu\text{s}$ rise/fall time). The spin is labeled $|\uparrow\rangle$ (red) or $|\downarrow\rangle$ (blue) depending on whether I_{SET} passes the threshold $I_T = 1.1$ nA (dashed lines). **b**, Histogram (circles) of the maximum values of I_{SET} in the interval $0 < t < 100\ \mu\text{s}$ (black squares in panel a), obtained from a 10,000 shot dataset. The red and blue lines are simulated histograms for states $|\uparrow\rangle$ and $|\downarrow\rangle$, respectively, and the black dashed line is the sum of the two. The simulated curves are obtained using $P_\uparrow = 0.47$, $\Delta I = 1.9$ nA, $1/\Gamma_{\uparrow,\text{out}} = 10\ \mu\text{s}$, $1/\Gamma_{\downarrow,\text{in}} = 40\ \mu\text{s}$. **c**, $|\uparrow\rangle$ (red) and $|\downarrow\rangle$ (blue) readout fidelities, and readout visibility (black) as a function of the discrimination threshold I_T . The maximum visibility is 92% at $I_T \approx 1.1$ nA. **d-e**, Histogram (circles) of the tunnel-out times for spin-up electrons, $\Gamma_{\uparrow,\text{out}}$ (**d**), and subsequent tunnel-in times for spin-down electrons, $\Gamma_{\downarrow,\text{in}}$ (**e**), as defined on the top trace in panel a. In **d**, notice a systematic $\sim 10\ \mu\text{s}$ delay between the beginning of the read phase and the tunnel-out events, due to the response of the amplifier and filter chain. The solid lines are exponential fits to extract the tunnel rates. These values of $1/\Gamma_{\uparrow,\text{out}}$ and $1/\Gamma_{\downarrow,\text{in}}$ were used to obtain the simulated curves in panel b.

3.11 Electron Spin Readout Fidelity

To assess the effectiveness of the spin readout process for quantum information purposes it is important to quantify the readout fidelity, i.e., the probability that an electron spin state is recognized correctly. In Fig. 3.14, we show the analysis of the readout fidelity for a set of 10,000 traces. The spin state is declared $|\uparrow\rangle$ if the peak value I_p taken by $I_{\text{SET}}(t)$ in the interval $0 < t < 100\mu\text{s}$ surpasses the threshold current I_T , and $|\downarrow\rangle$ otherwise. The probability distribution of I_p (Fig. 3.14b) shows well-resolved peaks, indicating that I_p takes two preferential values depending on the electron spin state. We have developed a numerical model that accurately simulates the measurement process and yields two separate histograms of peak current values for the states $|\downarrow\rangle$ and $|\uparrow\rangle$, $N_{\downarrow,\uparrow}(I_p)$, respectively.

The model, illustrated in Fig. 3.15, proceeds along the following steps:

- i. Randomly assign a spin state, $|\downarrow\rangle$ or $|\uparrow\rangle$ with a probability P_\downarrow or P_\uparrow , respectively. For $|\downarrow\rangle$ states, a trace with $I_{\text{SET}} = 0$ is created. For $|\uparrow\rangle$ states, a spin-up signal is generated, which includes a current pulse of height $\Delta I = 1.9 \text{ nA}$, as observed in the experiment. To simulate spin-up signals with the correct statistical properties, we generate for each trace two random numbers, r_{out} and r_{in} , with uniform probability distributions between 0 and 1. We thus define a pulse that starts after a delay $\tau_{\uparrow,\text{out}} = -\log(r_{\text{out}})/\Gamma_{\uparrow,\text{out}}$ and lasts a time $\tau_{\downarrow,\text{in}} = -\log(r_{\text{in}})/\Gamma_{\downarrow,\text{in}}$, with $\Gamma_{\uparrow,\text{out}} = 10 \mu\text{s}$ and $\Gamma_{\downarrow,\text{in}} = 40 \mu\text{s}$ as obtained from the fits to the experimentally observed tunnel times in Figs. 3.14d,e.
- ii. Add random Gaussian noise with amplitude A_n to each trace.
- iii. Apply a numerical filter with the same 6th order, 120 kHz low-pass Bessel

3. Electron Spin Readout

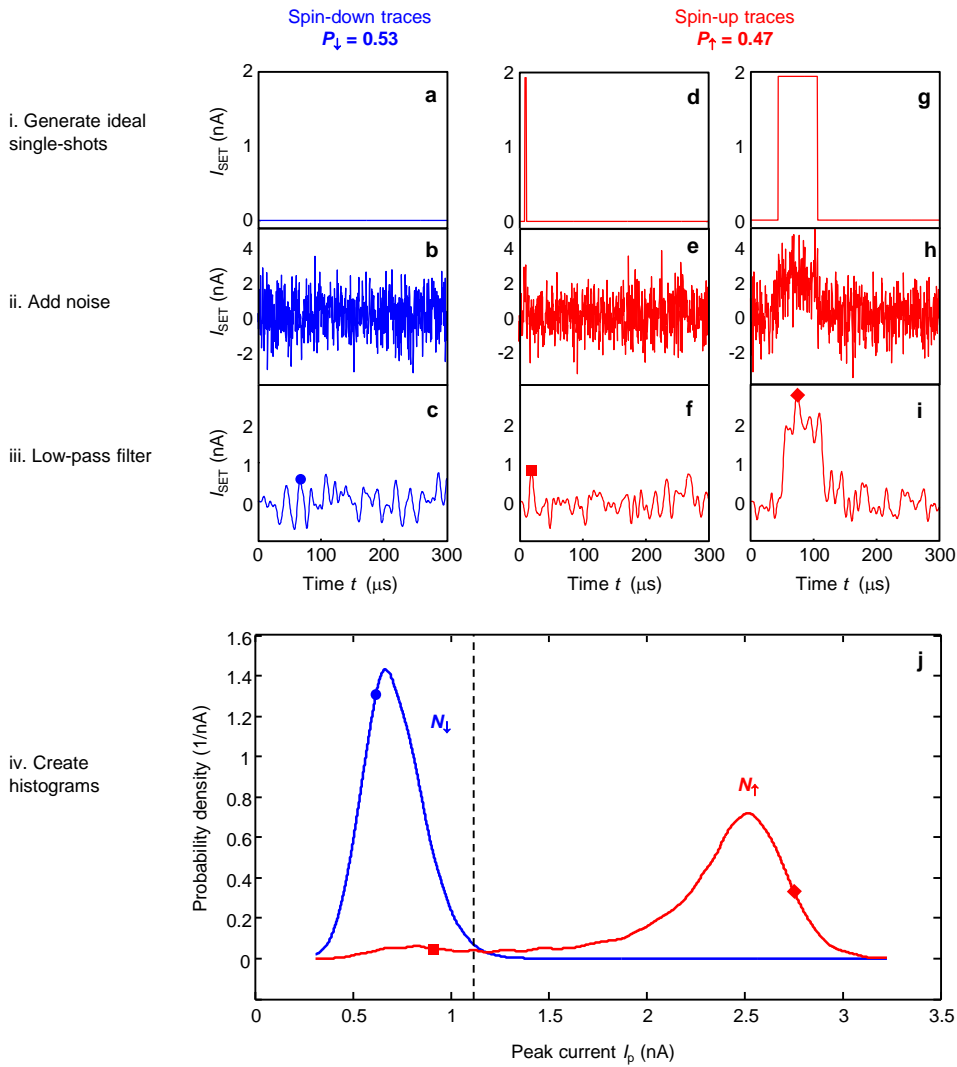


Figure 3.15: Calculation of the peak current distributions. Examples of the steps involved in calculating $N_{\downarrow}(I_p)$ and $N_{\uparrow}(I_p)$, as explained in the text. **a-c**, Spin-down traces. **d-i**, Spin-up traces. **j**, Calculated histograms, with the parameters that yield the best fit to the data in Fig. 3.14b. In **c**, **f** and **i**, the circle, square and diamond are the detected peak current values for each trace, and are reported in panel **j** accordingly. The dashed lines represent the optimal threshold current $I_T = 1.1$ nA, determined below.

3.11. Electron Spin Readout Fidelity

function as used in the experimental setup.

- iv. For each simulated trace, find the peak value I_p of $I_{\text{SET}}(t)$ in the interval $0 < t < 100 \mu\text{s}$. This value is used to construct the histograms $N_{\downarrow}(I_p)$ and $N_{\uparrow}(I_p)$, which represent the probability that a spin-down or spin-up electron produces a single-shot trace with a peak current value I_p . Here we can obtain separately $N_{\downarrow}(I_p)$ and $N_{\uparrow}(I_p)$ because we know a priori which spin state corresponds to each trace.

The only free parameters in the model are the noise amplitude A_n and the spin-up probability P_{\uparrow} . We start with an initial choice of A_n and P_{\uparrow} , generate $N_{\downarrow}(I_p)$ and $N_{\uparrow}(I_p)$ from 80,000 simulated traces, then run an optimization algorithm to find the best agreement between the simulated histograms and the experimental result, as shown in Fig. 3.14b. An example of the simulation is shown in Fig. 3.15. In particular, we show two different examples of spin-up signals, one of which is a current pulse of very short duration (Fig. 3.15d). Due to the low-pass filtering, such a short current pulse results in a low peak current (Fig. 3.15f). In a single-shot readout experiment, a trace like this would be erroneously interpreted as spin-down.

With the knowledge of $N_{\downarrow,\uparrow}(I_p)$, the readout fidelities [109] are obtained as $F_{\downarrow} = 1 - \int_{I_T}^{\infty} N_{\downarrow}(I)dI$ and $F_{\uparrow} = 1 - \int_{-\infty}^{I_T} N_{\uparrow}(I)dI$ for the states $|\downarrow\rangle$ and $|\uparrow\rangle$, respectively, as a function of the discrimination threshold I_T (Fig. 3.14c). The integrals in $F_{\downarrow,\uparrow}$ represent the probability that the spin state is incorrectly assigned, either because a spin-down trace has a noise spike $> I_T$, or because a spin-up signal does not reach the threshold. The visibility, defined as $V = F_{\downarrow} + F_{\uparrow} - 1$, reaches a maximum value $\approx 92\%$ at $I_T = 1.1 \text{ nA}$, where the readout fidelities are $F_{\downarrow} \approx 99\%$ and $F_{\uparrow} \approx 93\%$.

3.12 Suggestions for Future Device Improvements

Through careful design, the device described in this chapter is capable of achieving very high fidelity single-shot electron spin detection. As demonstrated, visibilities of up to 92% are possible with a magnetic field of $B_0 = 5$ T. Whilst the fidelity and visibility figures reported so far are promising, there is still room for improvement. The electrical readout errors may be mitigated with some practical changes to the experimental setup. The binary nature of the measurements (i.e. a spin-down electron gives a low I_{SET} and a spin-up electron gives maximum I_{SET}) could be exploited by employing a cryogenic current comparator [133], potentially enabling readout on a ~ 1 ns time scale. In addition to the vastly improved bandwidth, the noise floor would be significantly reduced due to the lower Johnson-Nyquist contribution (where $i_{\text{noise}} \propto \sqrt{T}$) and a reduced input capacitance resulting from the much shorter drain cable. The MOS compatibility of the device architecture also lends itself to the eventual fabrication of on-chip cryogenic current comparators, providing further improvements in speed and noise. The increased detection capabilities could be utilized by modifying the architecture to enable in-situ control of the electron tunnel times. This could be achieved by including a “rate gate” between the plunger and top gates to control the tunnel barrier separating the donor and SET island. There is, however, a limit to the coupling strength and hence readout speed possible. The levels $\mu_{1\downarrow}$ and $\mu_{1\uparrow}$ will be lifetime broadened by an amount $\hbar\Gamma_{\text{E/L}}$ where $\Gamma_{\text{E/L}}$ is the electron empty/load rate (see Section 3.7). At the typical magnetic fields that will be required to demonstrate spin control $B_0 \approx 2$ T, $E_Z \approx 230$ μeV . In order to attain good spin selectivity in the experiments we require $\hbar\Gamma_{\text{E/L}} \ll E_Z$. Taking $E_Z = 100\Gamma_{\text{E/L}}$, we then find a maximum tunnel rate of $\Gamma_{\text{E/L}} \approx 3$ Gs^{-1} , implying

sub-nanosecond tunnel times should be possible.

3.13 Conclusion

We have presented a detailed characterization of a device designed to measure the spin state of a single electron bound to a individual phosphorus donor in a silicon chip. Non-idealities in the readout process, including thermal broadening of states in the SET island, and the discrete nature of these states, have been discussed and experimentally investigated. The large charge transfer signal (Section 2.3.3) enabled by the coupled donor-SET architecture along with the long spin relaxation times (~ 50 ms at 5 T and up to 6 s at 1.5 T, see Fig. 3.9a) are responsible for the high electron spin readout fidelities demonstrated. Whilst there exist opportunities for optimization of the device and setup, the results achieved here have been more than adequate in demonstrating the appeal of this system (Si:P) for quantum information processing. The readout scheme has already enabled the demonstration of the first single donor-electron spin qubit (Chapter 4) as well as the readout and control of a single nuclear spin qubit in silicon (Chapter 5) - both of which represent landmark results in solid-state quantum computing.

Chapter 4

Electron Spin Qubit

A single atom is the prototypical quantum system, and a natural candidate for a quantum bit – the elementary unit of a quantum computer. Atoms have been successfully used to store and process quantum information in electromagnetic traps, as well as in diamond through the use of the NV-center point defect. Solid state electrical devices possess great potential to scale up such demonstrations from few-qubit control to larger scale quantum processors. In this direction, coherent control of spin qubits has been achieved in lithographically-defined double quantum dots in both GaAs and Si. However, it is a formidable challenge to combine the electrical measurement capabilities of engineered nanostructures with the benefits inherent to atomic spin qubits. This chapter details the coherent manipulation of an individual electron spin qubit bound to a phosphorus donor atom in natural silicon, which is measured electrically using the single-shot readout techniques introduced in Chapter 3. Electron spin resonance is employed to drive Rabi oscillations, while a Hahn echo pulse sequence reveals a spin coherence time (T_2) exceeding 200 μ s. This figure is expected to become even longer in isotopically enriched ^{28}Si samples. A model is then developed and used to breakdown and analyze the electron qubit system fidelity. Together with the use of a device architecture that is compatible with modern integrated circuit technology, these results indicate that the electron spin of a single phosphorus atom in silicon is an excellent platform on which to build a scalable quantum computer.

Parts of this chapter have been published in:

Pla, J. J., Tan, K. Y., Dehollain, J. P., Lim, W. H., Morton, J. J. L., Jamieson, D. N., Dzurak, A. S. and Morello, A. *Nature* **489**, 541-545 (2012).

4.1 Introduction

As was introduced in Section 1.2, there have been a number of proposals for the implementation of a solid-state spin-based qubit [47, 134, 135]. The phosphorus atom in silicon is among the most studied and best-understood systems in this context. This interest has been motivated by the knowledge, developed over half a century from electron spin resonance experiments on bulk-doped phosphorus in silicon [48], that spin coherence times can be exceptionally long, exceeding seconds [83] even for the electron spin. This is due to the availability of silicon in an enriched nuclear spin-zero (^{28}Si) form, as well as the low spin-orbit coupling in silicon [48]. The use of donor electron spins has further advantages of consistency (since each atom is identical) and tuneability (e.g. through the Stark shift [77]), while the donor atoms nuclear spin can be employed as a quantum memory for longer term storage [92].

Using methods compatible with existing complementary metal-oxide-semiconductor (CMOS) technology, we have fabricated a nanostructure device on the SiO_2 surface to enable read-out and control of an electron spin [85] (Fig. 4.1a). In this work, the donor is intentionally implanted into the silicon substrate, with future options including the use of deterministic ion implantation [66] or atomic precision in donor placement through scanning probe lithography [67].

4.2 Electron Spin Resonance

The device is placed in a magnetic field of ~ 1 T, yielding well-defined electron spin-down and spin-up states ($|\downarrow\rangle$ and $|\uparrow\rangle$). Transitions between the electron $|\downarrow\rangle$ and $|\uparrow\rangle$ states are driven by an ac magnetic field generated by applying

4.2. Electron Spin Resonance

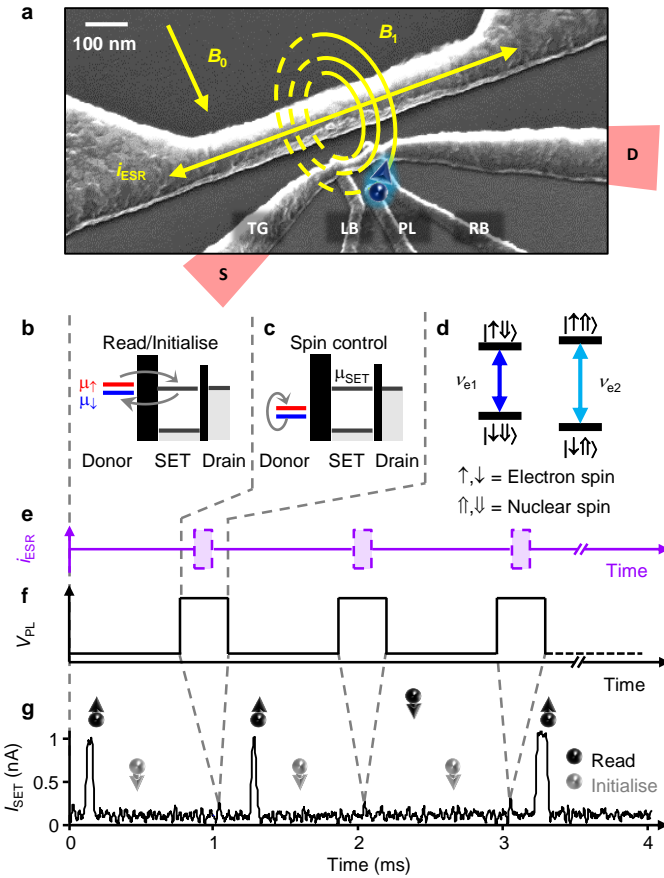


Figure 4.1: Qubit device and pulsing scheme. **a**, Scanning electron micrograph of a qubit device similar to the one used in the experiment. The SET (lower right portion) consists of a top gate (TG), plunger gate (PL), left and right barrier gates (LB and RB) and source/drain contacts (S and D). The microwave transmission line is shown in the upper left portion. The donor (blue) is subject to an oscillating magnetic field B_1 from the transmission line which is perpendicular to the in-plane external field B_0 . **b-c**, Pulse sequence for the qubit initialization, control and readout. **b**, Read/initialization phase $\mu_{\downarrow} < \mu_{\text{SET}} < \mu_{\uparrow}$: A spin-up electron will tunnel from the donor to the SET island, to later be replaced by a spin-down electron, causing a pulse of current through the SET. A spin-down electron remains trapped on the donor throughout the entire phase. **c**, Control phase $\mu_{\downarrow}, \mu_{\uparrow} \ll \mu_{\text{SET}}$: Electron spin states are plunged well below the SET island Fermi level whilst microwaves are applied to the transmission line to perform electron spin resonance. **d**, Energy level diagram of the ^{31}P electron-nuclear system. **e-f**, Microwave pulse sequence (e) and synchronized PL gate voltage waveform (f) for performing and detecting spin manipulations (not drawn to scale). An arbitrary ESR pulse sequence is represented by the dashed purple box in panel e. **g**, Example of I_{SET} response to four consecutive read/control events where a single microwave excitation of duration t_p is applied, taken at $B_0 = 1.07$ T. The time t_p has been set to give a high probability of flipping the electron spin. A statistical analysis of the I_{SET} pulse durations gives the electron spin-down tunnel-in time (~ 33 μs), whilst an analysis of their delay from the beginning of the read phase gives the spin-up tunnel-out time (~ 295 μs).

microwaves to a broadband on-chip loop [57, 102] (refer to Section 2.4). By operating at a high magnetic field and low electron temperature ($T_{\text{el}} \approx 300$ mK), we can detect these transitions through single-shot projective measurements on the electron spin using spin-to-charge conversion [86, 107] (see Chapter 3). Here the donor electron is both electrostatically and tunnel coupled to the island of a single electron transistor, with the SET serving as both a sensitive charge detector and an electron reservoir for the donor. Using gates PL and TG (Fig. 4.1a) to tune the electrochemical potentials of the donor electron spin states (μ_{\downarrow} and μ_{\uparrow} for states $|\downarrow\rangle$ and $|\uparrow\rangle$) and the Fermi level in the SET island (μ_{SET}), we can discriminate between a $|\downarrow\rangle$ and $|\uparrow\rangle$ electron as well as perform electrical initialization of the qubit, following the procedure introduced in Section 3.8.

Our experiments use a two-step cyclical sequence of the donor potential, alternating between a spin readout/initialization phase and a coherent control phase. The qubit is first initialized in the $|\downarrow\rangle$ state through spin-dependent loading by satisfying the condition $\mu_{\downarrow} < \mu_{\text{SET}} < \mu_{\uparrow}$ (Fig. 4.1b). Following this, the system is brought into a regime where the spin is a stable qubit ($\mu_{\downarrow}, \mu_{\uparrow} \ll \mu_{\text{SET}}$) by lowering the donor potential below the Fermi level. Here the spin is manipulated with various microwave pulse schemes resonant with the spin transition (Fig. 4.1c). The spin is then read out electrically via spin-to-charge conversion (Fig. 4.1b), a process which produces a pulse in the current through the SET I_{SET} if the electron was μ_{\uparrow} , and leaves the qubit initialised μ_{\downarrow} for the next cycle.

The electron spin resonance frequencies have been extracted from the spin Hamiltonian describing this system (see Section 1.4). If $\gamma_e B_0 \gg A$, the states shown in Fig. 4.1d are good approximations for the eigenstates of Eq. 1.1. Allowed transitions involving flips of the electron spin only (identified by arrows in

4.2. Electron Spin Resonance

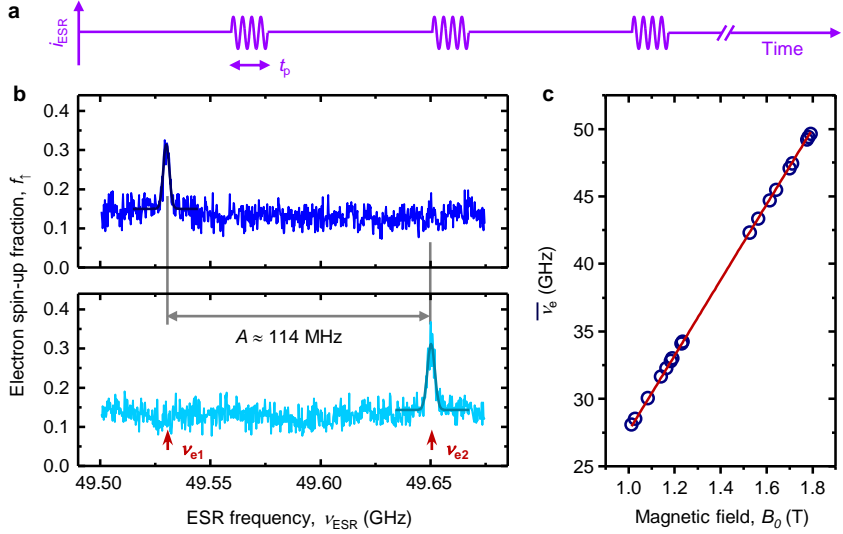


Figure 4.2: ESR spectra. **a**, Microwave pulse sequence used in the ESR experiment. **b**, ESR spectra at $B_0 = 1.79$ T and with a microwave pulse length of $t_p = 100$ μ s, obtained by counting the occurrence of $|\uparrow\rangle$ electrons while scanning the ESR frequency. Each data point is obtained from 250 single-shot counts. The nuclear spin is in the state $|\downarrow\rangle$ in the top panel, and $|\uparrow\rangle$ in the bottom panel. **c**, Center ESR frequency, $|\nu_e| = (\nu_{e1} + \nu_{e2})/2$, as a function of the external magnetic field B_0 .

Fig. 4.1d) exhibit resonance frequencies (Eq. 1.5) that depend on the state of the ^{31}P nuclear spin: $\nu_{e1} \approx \gamma_e B_0 - A/2$ for nuclear spin-down; and $\nu_{e2} \approx \gamma_e B_0 + A/2$ for nuclear spin-up. The transition frequencies ν_{e1} and ν_{e2} are found by conducting an electron spin resonance (ESR) experiment [136].

The ESR experiment follows the measurement sequence described above and outlined in Figs. 4.1b-f. However, instead of a resonant pulse sequence, the purple dashed boxes of Fig. 4.1e are replaced with a single microwave pulse of frequency ν_{ESR} (a train of such pulses is depicted in Fig. 4.2a). If ν_{ESR} coincides with one of the two possible ESR resonances, the electron spin can be excited from $|\downarrow\rangle$ to $|\uparrow\rangle$, which increases the probability of detecting a $|\uparrow\rangle$ state in the readout/initialisation phase (Fig. 4.1b). Figure 4.2b shows two measurements of the electron spin-up fraction f_{\uparrow} as a function of the ESR frequency. f_{\uparrow} is found for each ν_{ESR} by

repeating 250 times the sequence outlined above and counting the number of shots that produce a $|\uparrow\rangle$ state. The spectra in Fig. 4.2b were each obtained over 10 minutes and contain a single peak at either ν_{e1} or ν_{e2} . The ESR pulse sequence is almost identical to that used in the coherent Rabi measurements below, but here the microwave pulse length t_p is $\gg T_2^*$ ($= 55$ ns), resulting in an incoherent superposition of the states $|\downarrow\rangle$ and $|\uparrow\rangle$.

From the ESR spectra of Fig. 4.2b, we extract a hyperfine splitting $A \approx 114$ MHz, close to the bulk value of 117.52 MHz [76]. We attribute the slight difference in value to a Stark shift of the hyperfine coupling, caused by the strong electric fields produced at the donor site by the gated nanostructure surrounding it. Figure 4.2c shows the ESR center frequency $\overline{\nu_e}$ as a function of the external magnetic field B_0 . From the slope of a linear fit through the data of Fig. 4.2c, we can extract the electron g -factor using the relation:

$$\overline{\nu_e} = \frac{\nu_{e1} + \nu_{e2}}{2} = \frac{g\mu_B}{h}B_0, \quad (4.1)$$

where g is the Landé g -factor, μ_B is the Bohr magneton and h is the Planck constant. We find that $g = 1.98(2)$ (accuracy limited by the uncertainty in B_0), which is consistent with the bulk measured value of 1.9985 [76]. A more accurate measure of g is made in Section 5.7 using the NMR transition frequencies.

4.3 Electron Spin Rabi Oscillations

To demonstrate coherent control, we apply a single microwave pulse of varying duration t_p to perform Rabi oscillations of the electron spin. Following the pulse protocol outlined in Figs. 4.1e,f, we take 250 single-shot projective measurements

4.3. Electron Spin Rabi Oscillations

of the electron spin, first at ν_{e1} and immediately after at ν_{e2} (it is necessary to pulse on both ESR transitions as the ^{31}P nuclear spin can flip several times during acquisition of the Rabi data). Figure 4.1g displays single-shot traces of the SET output current I_{SET} for four consecutive repetitions of the measurement sequence, for an arbitrary pulse length. The threshold detection method (Section 3.10) is used to determine the fraction of shots that contain a $|\uparrow\rangle$ electron for the measurements at both frequencies. Figure 4.3a shows the electron spin-up fraction f_{\uparrow} at each frequency as a function of the microwave burst duration t_p . In this particular measurement run we observe that at $t_p \approx 250$ ns the ^{31}P nuclear spin flips from up to down. As a consequence, the frequency at which the electron spin responds to the microwave excitation jumps from ν_{e2} to the other hyperfine transition at ν_{e1} . Figure 4.3b combines 80 of these sweeps, and shows the average $f_{\uparrow}(t_p)$ for both transition frequencies. Also presented here is the off-resonance electron spin-up fraction (the “false counts”), which is found at each t_p by taking the minimum f_{\uparrow} observed at either ν_{e1} or ν_{e2} for each sweep and averaging over all sweeps.

The off-resonance signal exhibits a linear dependence on the pulse duration, i.e. the “false counts” increase for longer microwave bursts. Since we also observed that the slope is proportional to the microwave power P_{ESR} , we attribute this effect to local heating of the electron reservoir caused by the energy delivered by the transmission line. To get the final Rabi plot of Fig. 4.3c, we sum the averaged $f_{\uparrow}(t_p)$ plots at ν_{e1} and ν_{e2} and subtract a fit through the off-resonance background, since at each t_p the measurement is off-resonance for half of the time.

Figure 4.4a shows the electron spin-up fraction f_{\uparrow} as a function of the microwave pulse duration for different applied powers, P_{ESR} . The fits through the

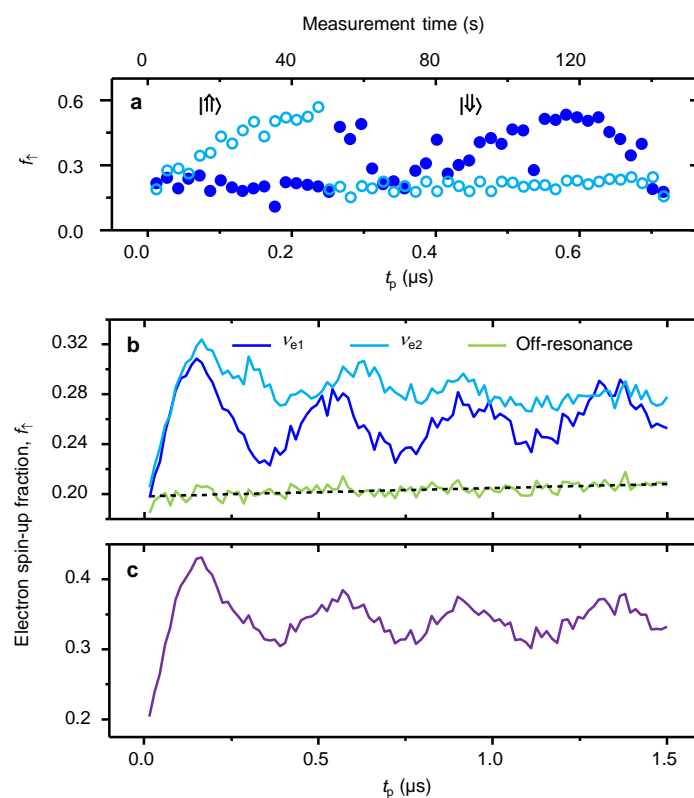


Figure 4.3: Rabi oscillation. **a**, Single Rabi sweep at $P_{\text{ESR}} = 7$ dBm. 250 single-shot electron spin readout measurements are performed at ν_{e1} (solid dark blue circles) and ν_{e2} (open light blue circles) for each t_p . The top axis displays the time taken to acquire the data. **b**, Averaged Rabi data over 80 sweeps at ν_{e1} (dark blue) and ν_{e2} (light blue). Also shown is the averaged off-resonance spin-up fraction (green) with a linear fit (black dash). **c**, Combined ν_{e1} and ν_{e2} Rabi data, minus the off-resonance contribution.

4.3. Electron Spin Rabi Oscillations

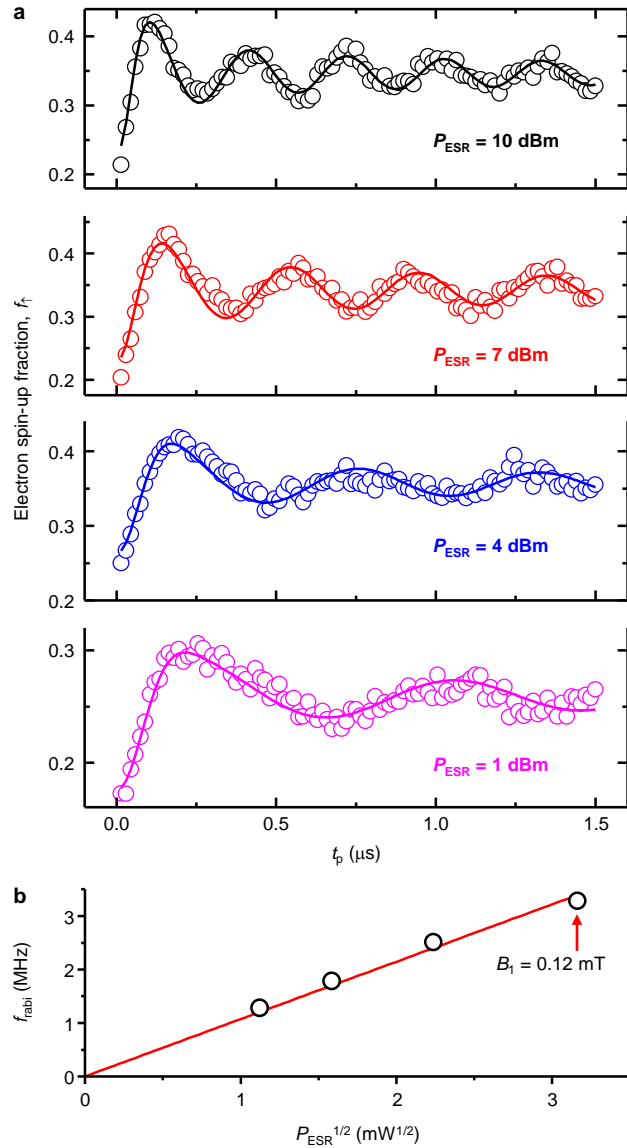


Figure 4.4: Rabi oscillations and power dependence of the Rabi frequency. **a**, Electron spin-up fraction as a function of the microwave burst duration for varying input powers P_{ESR} . Measurements were performed at an external field of $B_0 = 1.07 \text{ T}$ where the ESR frequencies are $\nu_{e1} = 29.886 \text{ GHz}$ and $\nu_{e2} = 30.000 \text{ GHz}$. Each point represents an average of 20,000 single-shot measurements, with each shot $\approx 1 \text{ ms}$ in duration. The solid lines are fits generated from simulations of the measurements. **b**, Rabi frequency versus the microwave excitation amplitude, with a fit displaying the linear relationship.

data are derived from simulations assuming Gaussian fluctuations of the local field (see below). Confirmation that these are Rabi oscillations comes from the linear dependence of the Rabi frequency with the applied microwave amplitude ($P_{\text{ESR}}^{1/2}$), i.e. $f_{\text{rabi}} = \gamma_e B_1$. Here B_1 is taken as half of the total linear oscillating magnetic field amplitude generated by the transmission line at the site of the donor, assuming the rotating wave approximation. Figure 4.4b shows the expected linear behavior with microwave amplitude of the Rabi frequencies extracted from the data in Figure 4.4a. The largest Rabi frequency attained was 3.3 MHz ($B_1 \approx 0.12$ mT), corresponding to a $\pi/2$ rotation in ~ 75 ns.

4.4 Simulation of Rabi Oscillations

To simulate the Rabi oscillations of Fig. 4.4a, we assume a decohering noise source with the following properties:

1. It can be modelled by a fluctuating magnetic field $\Delta B(t)$ along the axis parallel to B_0 . Physically, this can represent the z-component of the hyperfine (often called ‘Overhauser’) field produced by the bath of ^{29}Si nuclei on the electron spin [137, 138];
2. It follows normal (Gaussian) statistics;
3. It changes significantly from one individual measurement (“shot”) to the next, where each measurement lasts ~ 1 ms.

Assumption 3 is non-trivial. As we will show in Fig. 4.8b below (see Section 4.6), the ESR linewidth for a single sweep is narrower than that observed by ESR in bulk-doped samples, however by averaging several sweeps we recover

4.4. Simulation of Rabi Oscillations

a bulk-like linewidth (bottom panel of Fig. 4.8b). The observation of a non-zero width for a single sweep shows that some randomization of the Overhauser field does occur. We suggest that this is caused by the measurement method we employ, where the electron spin is read out through spin-dependent tunneling. The removal of the electron from the donor causes a large instantaneous change of the total magnetic field at each ^{29}Si nucleus. Several ^{29}Si sites have a strongly anisotropic hyperfine coupling [139]. Spins at those sites have a large probability of flipping as a consequence of an electron ionization/neutralization event. Conversely, other ^{29}Si have a very isotropic coupling to the electron spin, and their polarization is much less influenced by the measurement process. Slow nuclear spin flips at these ^{29}Si sites are likely to be responsible for the large shift of the central frequency between different sweeps.

In the Rabi experiment, each t_p point represents an average of 20,000 measurements. Over such a large number of shots, we may safely assume that the Overhauser field (e.g. the configuration of the ^{29}Si nuclear bath spins) spans the whole permissible range. We therefore generate a weighted distribution of detunings $d = \gamma_e \Delta B$ from the central values of the ESR frequencies ν_{e1} or ν_{e1} . The distribution of detunings, $P(d)$, is assumed to be a Gaussian function with standard deviation σ and mean μ :

$$P(d) = \frac{1}{\sqrt{2\pi}\sigma} \exp\left(\frac{-(d-\mu)^2}{2\sigma^2}\right), \quad (4.2)$$

where a value of $\mu \neq 0$ represents an experiment where the frequency of the microwave excitation is shifted from the center of the resonance line. For each detuning d , the Rabi oscillation (i.e. the electron spin-up probability as a function

of burst time t_p) is described by:

$$f_{\text{Rabi}}(t_p, d) = \frac{\Omega_1^2}{\Omega_1^2 + d^2} \sin^2 \left(\pi t_p \sqrt{\Omega_1^2 + d^2} \right), \quad (4.3)$$

The method above yields a model for the decay of the Rabi oscillations as a function of the pulse duration t_p as caused by a fluctuating Overhauser field. To match the experimental data we must also include non-idealities arising from the finite temperature of the electron reservoir (the SET island) to/from which the electrons tunnel. We define the parameter α as the probability of a spin-down electron $|\downarrow\rangle$ tunneling to the SET island during the read phase, and β as the probability of erroneously initializing the electron spin-up $|\uparrow\rangle$ (see Fig. 4.8a of Section 4.6). We define $P_{\uparrow I}$, as the probability of having a non-zero fraction of spin-up counts on the off-resonance – “inactive” – hyperfine line (the “false counts” rate), and $P_{\uparrow A}$ as the as the maximum spin-up fraction for the on-resonance – “active” – line. $P_{\uparrow I}$ also represents the spin-up fraction at (ideal) Rabi angles $2\pi, 4\pi, \dots$, while $P_{\uparrow A}$ is the spin-up fraction at (ideal) Rabi angles $\pi, 3\pi, \dots$

The measurement process is non-Markovian in nature. At any given shot, whether or not we load a new electron onto the donor depends on the outcome (spin-up detected or not) of the previous shot. Therefore $P_{\uparrow I}$ and $P_{\uparrow A}$ must be derived recursively. Calling $P_{\uparrow I}(0)$ and $P_{\uparrow A}(0)$ the probabilities to detect a spin-up count after a fresh electron load (i.e. loading onto a donor that was certainly ionized), we find the following recursive expressions:

$$\begin{aligned}
 P_{\uparrow I}(0) &= \beta + (1 - \beta)\alpha \\
 P_{\uparrow I}(i + 1) &= P_{\uparrow I}(i) P_{\uparrow I}(0) + [1 - P_{\uparrow I}(i)]\alpha \\
 &= P_{\uparrow I}(i) \beta(1 - \alpha) + \alpha
 \end{aligned} \tag{4.4}$$

$$\begin{aligned}
 P_{\uparrow A}(0) &= (1 - \beta) + \beta\alpha \\
 P_{\uparrow A}(i + 1) &= P_{\uparrow A}(i) P_{\uparrow A}(0) + [1 - P_{\uparrow A}(i)] \\
 &= 1 - P_{\uparrow A}(i) \beta(1 - \alpha)
 \end{aligned} \tag{4.5}$$

Finally, we include the imperfections of the measurement with a parameter F_{\uparrow} that represents the fidelity with which we detect a peak in I_{SET} caused by an electron tunneling out of the donor during the readout phase (see Section 4.6 for more details). Combining this with the thermal initialisation/readout effects, we call $K = F_{\uparrow}P_{\uparrow I}$ the observed baseline of the off-resonance counts, and $C = F_{\uparrow}(P_{\uparrow A} - P_{\uparrow I})$ the maximum Rabi oscillation depth, e.g. between (ideal) rotation angles 0 and π (see Fig. 4.5).

Combining all the effects together yields the following expression for the complete model of the Rabi oscillation experiment:

$$f_{\uparrow}(t_p) = K + C \sum_{d=\mu-5\sigma}^{\mu+5\sigma} P(d) f_{\text{Rabi}}(t_p, d) \Delta d, \tag{4.6}$$

where Δd is the detuning step-size.

The final step in producing the Rabi simulations is to run a nonlinear least-squares optimization algorithm to match Eq. (4.6) to the experimental data, where μ , Ω_1 , α and β are free fitting parameters. σ is fixed at 3.2 MHz, the value extracted from the ESR spectra of Fig. 4.8b. We chose Δd such that the

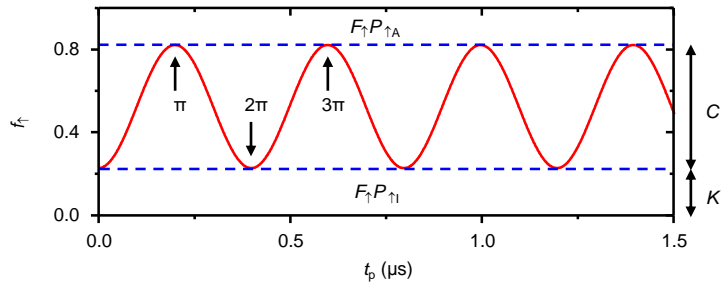


Figure 4.5: Rabi simulation model – measurement and thermal effects. Rabi oscillation with $F_1 = 2.5$ MHz, and $\sigma = \mu = 0$ MHz, i.e. no fluctuations or resonance offset. This is what a Rabi oscillation would look like in the absence of a fluctuating Overhauser field, but accounting for measurement errors and thermal effects (“false counts” and incorrect initialisation).

summation was done over ~ 2000 detunings ($\Delta d \approx 10$ kHz), a sample large enough that the fitting parameters had converged. We also note that in the above analysis, we have ignored any contribution due to incorrect detection of the $|\downarrow\rangle$ electron state, since $1 - F_{\downarrow} \approx 0$.

4.5 Electron Spin Coherence

The qubit manipulation time, as determined from the Rabi oscillations, should be contrasted with the coherence lifetime of the qubit, termed T_2 . Possible sources of decoherence include spectral diffusion of the ^{29}Si bath spins [48, 140, 141], noise in the external magnetic field, and paramagnetic defects and charge traps at the Si/SiO₂ interface [142]. These mechanisms can, to a degree, be compensated for by utilizing spin echo techniques (Fig. 4.6a), as long as the fluctuations are slow compared with the electron spin manipulation time (typically ~ 100 ns).

Figure 4.6a presents the gate voltage and microwave pulsing scheme for a Hahn echo measurement. Dephasing resulting from static local contributions to the total effective field during an initial period τ_1 is (partially or fully) refocused

4.5. Electron Spin Coherence

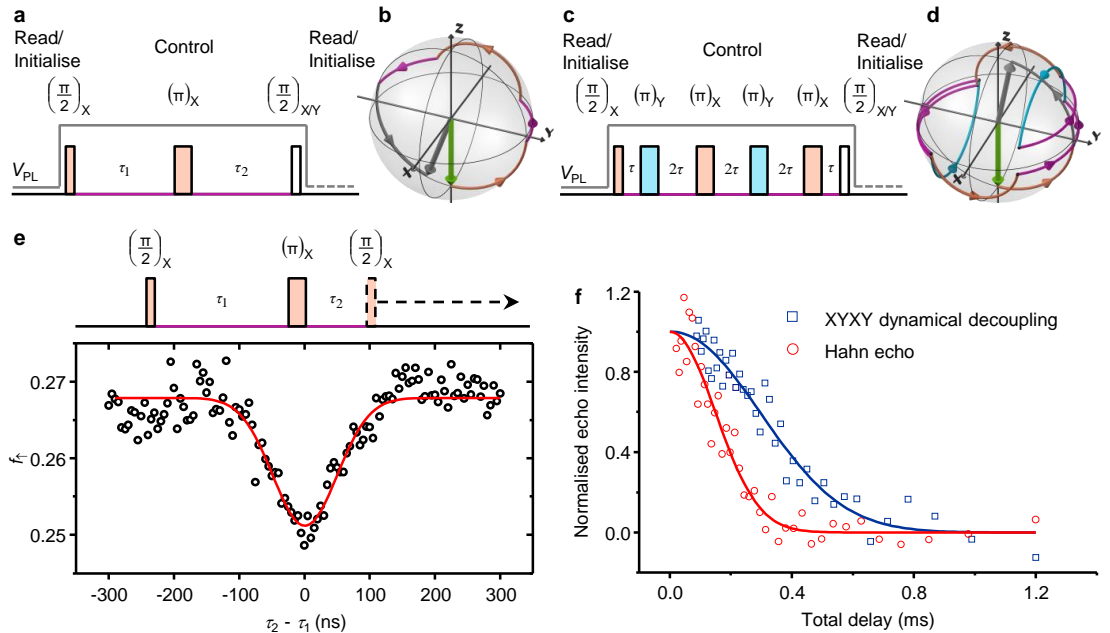


Figure 4.6: Coherence time and dynamical decoupling. **a-b**, Pulse protocols for the Hahn echo (**a**) and XYXY dynamical decoupling (**b**) sequences with accompanying PL gate voltage waveforms, as described in the main text. The rotation angles are displayed above each pulse in brackets, with the subscript (X or Y) denoting the axis on the Bloch sphere about which the rotation is applied. The read/initialization time is 1 ms. All measurements were performed at $B_0 = 1.07$ T and with $P_{\text{ESR}} = 10$ dBm, where a $\pi/2$ rotation takes ~ 75 ns. **c-d**, Bloch sphere representation of the evolution in the rotating frame for the Hahn echo (**c**) and XYXY (**d**) sequences. The green arrow represents the initial spin state $|\downarrow\rangle$, whilst the gray arrow represents the final state for the case when the second $\pi/2$ pulse is about X (Y is not shown). The purple path represents dephasing in between pulses, the orange path represents a rotation about X, and the blue path is a rotation about Y. We have included rotation angle errors of 5° and 15° for the $\pi/2$ and π pulses respectively. **e**, An echo curve, obtained by applying the depicted pulse sequence with a fixed τ_1 ($= 10\mu\text{s}$) and varying τ_2 . Each point represents the electron spin-up fraction f_\uparrow calculated from 50,000 single-shots acquired at both ESR frequencies ($\nu_{\text{e1}} = 29.886$ GHz and $\nu_{\text{e2}} = 30.000$ GHz) and summed. The fit in red is Gaussian and of the form $f_\uparrow = B \exp -[(\tau_2 - \tau_1)/C]^2 + D$. **f**, Hahn echo (XYXY dynamical decoupling) decay in red circles (blue squares), measured using phase cycling (see below). A fit through the data is given by $y = \exp -(N\tau/T_2)^b$, where $N = 2$ ($N = 8$) for the Hahn echo (XYXY dynamical decoupling) experiment. Parameter values are discussed in the main text.

by a π rotation followed by a second period τ_2 (see Fig. 4.6b for a Bloch sphere state evolution). A spin echo is observed by varying the delay τ_2 and recording the spin-up fraction. In Fig. 4.6e we plot the difference in delay times $(\tau_2 - \tau_1)$ against f_{\uparrow} . For $\tau_1 = \tau_2$, we expect to recover a $|\downarrow\rangle$ electron at the end of the sequence if little dephasing occurs (i.e. for short τ), and hence observe a minimum in f_{\uparrow} . When $\tau_2 - \tau_1 \neq 0$, imperfect refocusing results in an increase in the recovered spin-up fraction. The echo shape is approximated as being Gaussian and the half-width at half-maximum implies a pure dephasing time of $T_2^* = 55(5)$ ns.

We now set $\tau = \tau_1 = \tau_2$ and monitor the spin-up fraction as a function of τ , to obtain the spin echo decay curve of Fig. 4.6f. A fit of the form $y = \exp(-(2\tau/T_2)^b)$, where T_2 and b are free parameters, yields $T_2 = 206(12)\mu\text{s}$ and $b = 2.1(4)$. The coherence time T_2 is almost a factor of 2000 times longer than T_2^* , and is remarkably close to the value (300 μs) measured in bulk-doped natural silicon samples [143]. Variations in T_2 can be expected, depending on the exact distribution of ^{29}Si nuclei within the extent of the donor electron wavefunction. This indicates that the presence of a nearby SET and the close proximity of the Si/SiO₂ interface have little, if any, effect on the electron spin coherence. This is not entirely surprising, since paramagnetic centers at the Si/SiO₂ interface are expected to be fully spin polarized under our experimental conditions $g\mu_BB_0 \gg k_BT$ (where g is the center g -factor, μ_B is the Bohr magneton and k_B is the Boltzmann constant), leading to an exponential suppression of their spin fluctuations [144]. Direct flip-flop transitions between the donor electron qubit and nearby interface traps are suppressed by the difference in g -factor ($g = 1.9985$ for the donor, $g > 2$ for the traps [136]), whereas dipolar flip-flops with nearby donors [145] can appear as a T_1 process (Section 3.10) on a much longer timescale.

We measured $T_1 \approx 0.7$ s at $B_0 = 2.5$ T (data not shown), implying that this process has no bearing on T_2 . The echo decay is Gaussian in shape ($b \approx 2$), consistent with decoherence dominated by ^{29}Si spectral diffusion [140].

We have extended the coherence time by applying an XYXY dynamical decoupling ESR pulse sequence [146] (Figs. 4.6c,d). This sequence substitutes the single π rotation of the Hahn echo with a series of four π rotations alternating about the X and Y axis, achieved by applying adjacent π pulses that are 90° out of phase (see Section 2.2). The resulting echo decay is shown in Fig. 4.6f, with a fit to the data yielding $T_2 = 410(20)\mu\text{s}$ and $b = 2.1(4)$. As well as delivering a factor of 2 improvement in T_2 , the XYXY sequence demonstrates the ability to perform controlled rotations about two orthogonal axes on the Bloch sphere (X and Y), permitting arbitrary one-qubit gates for universal quantum computing [147].

4.5.1 Phase Cycling

Phase cycling is a well-known technique in bulk electron paramagnetic resonance (EPR) experiments [148], used to cancel unwanted artifacts. This is accomplished by adding or subtracting the signals from pulse sequences where the phase of the individual pulses is carefully chosen and varied. We employ a type of phase cycling in our Hahn echo decay and XYXY dynamical decoupling experiments. Here the phase of the final $\pi/2$ pulse in each sequence is altered between two different experimental runs, and the results are subtracted in order to remove any background signal. This ensures that the decays of Fig. 4.6f have a baseline of ~ 0 .

For each τ ($\tau = \tau_1 = \tau_2$ for the Hahn echo), the sequence of Fig. 4.6a (Fig. 4.6c) is repeated 30,000 times (75,000 times) for the Hahn echo (XYXY dynamical

decoupling) measurement at both ν_{e1} and ν_{e2} , and for X and Y phases of the final $\pi/2$ rotation. The resulting signal amplitude is given by $(f_{\uparrow}(\nu_{e1}, Y) - f_{\uparrow}(\nu_{e1}, X)) + (f_{\uparrow}(\nu_{e2}, Y) - f_{\uparrow}(\nu_{e2}, X))$, where $f_{\uparrow}(\nu_{e1}, Y)$ represents the electron spin-up fraction of the single-shot traces taken at ν_{e1} with a final $\pi/2$ pulse about the Y-axis etc. The data points in Fig. 4.6f have been re-normalized with the amplitudes and residual offsets extracted from free-exponent fits through the decays. A 30% reduction in signal amplitude was observed for the XYXY dynamical decoupling decay, relative to that of the Hahn echo. This reduction is likely the result of accumulated pulse errors.

4.6 Electron Spin Qubit Fidelity

Next we consider the fidelity of our electron spin qubit, broken down into three components: measurement, initialization and control.

4.6.1 Measurement Fidelity

The measurement fidelity F_M comprises errors resulting from detection limitations of the experimental setup as well as thermally-induced readout events. The electrical spin-down and spin-up read errors (γ_{\downarrow} and γ_{\uparrow} respectively) arise from a finite measurement bandwidth and signal-to-noise ratio. They depend on the threshold current I_T used for detecting the spin-up pulses. A finite bandwidth can result in an electron spin-up signal (SET current pulse) being missed. Alternatively, electrical noise can cause an incorrect classification of a $|\downarrow\rangle$ state as $|\uparrow\rangle$. We term these ‘‘electrical readout errors’’ in order to distinguish them from errors arising from thermal effects. Figure 4.7a presents the probability densi-

4.6. Electron Spin Qubit Fidelity

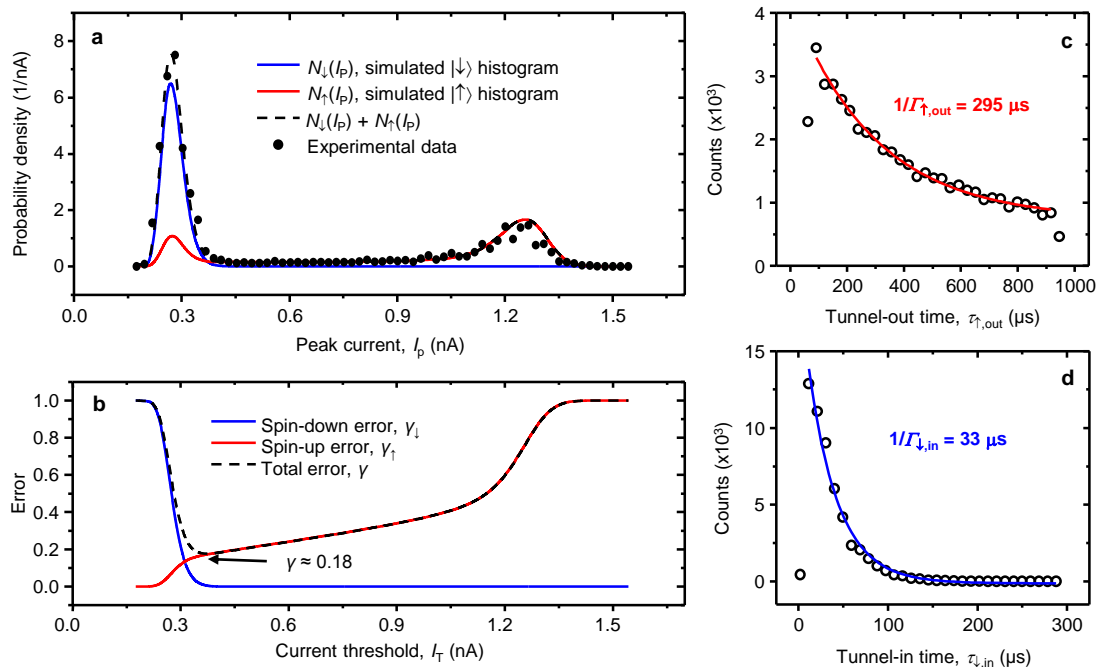


Figure 4.7: Measurement fidelity analysis. **a**, Peak current histogram (black circles) for the spin readout signal during the read phase, taken from approximately 125,000 single-shot measurements. Simulations of the peak current histograms for $|↓\rangle$ and $|↑\rangle$ electron states are given by the blue and red lines respectively, while their sum is given by the black dashed line. **b**, Electrical readout errors calculated from the simulated histograms of **a**. **c**, Electron spin-up tunnel-out time ($\sim 295 \mu s$) used in the simulations of panel **a**. **d**, Spin-down tunnel-in time ($\sim 33 \mu s$). A delay of $\sim 10 \mu s$ between the beginning of the read phase and tunnel events exists, because of the post amplifier and filter chain.

ties of peak SET current values for $|\downarrow\rangle$ and $|\uparrow\rangle$ electrons during the read phase. The blue and red curves ($N_{\downarrow}(I_p)$ and $N_{\uparrow}(I_p)$ respectively) are simulations which take a number of parameters as inputs, including the electron spin-up tunnel out time (Fig. 4.7c) and electron spin-down tunnel in time (Fig. 4.7d). A detailed explanation of the model used here can be found in Section 3.11. The simulation parameters are optimized in order to obtain a good fit to the peak current data (black solid circles in Fig. 4.7a) extracted from experiment.

With knowledge of the probability densities $N_{\downarrow}(I_p)$ and $N_{\uparrow}(I_p)$, one can readily calculate the electrical readout errors associated with $|\downarrow\rangle$ and $|\uparrow\rangle$ electrons by applying (4.7a) and (4.7b) respectively. Figure 4.7b shows the calculated errors as a function of the discrimination threshold I_T used when assigning a spin state to a single-shot measurement. We find a minimum total electrical error of $\gamma = \gamma_{\downarrow} + \gamma_{\uparrow} = 18(2)\%$ at $I_T = 370$ pA.

$$\gamma_{\downarrow} = \int_{I_T}^{\infty} N_{\downarrow}(I) dI, \quad (4.7a)$$

$$\gamma_{\uparrow} = \int_{-\infty}^{I_T} N_{\uparrow}(I) dI, \quad (4.7b)$$

With (4.7a) and (4.7b), the fidelities used in Section 4.4 are denoted as $F_{\downarrow(\uparrow)} = 1 - \gamma_{\downarrow(\uparrow)}$.

In addition to the electrical readout errors discussed, thermal broadening of the states in the SET island will also contribute to measurement fidelity degradation. Thermal broadening of the Fermi distribution in the SET island produces the read/load errors, as depicted in Fig. 4.8a. The process of a spin-down electron tunneling into an empty state in the SET occurs with a probability α , whereas β

4.6. Electron Spin Qubit Fidelity

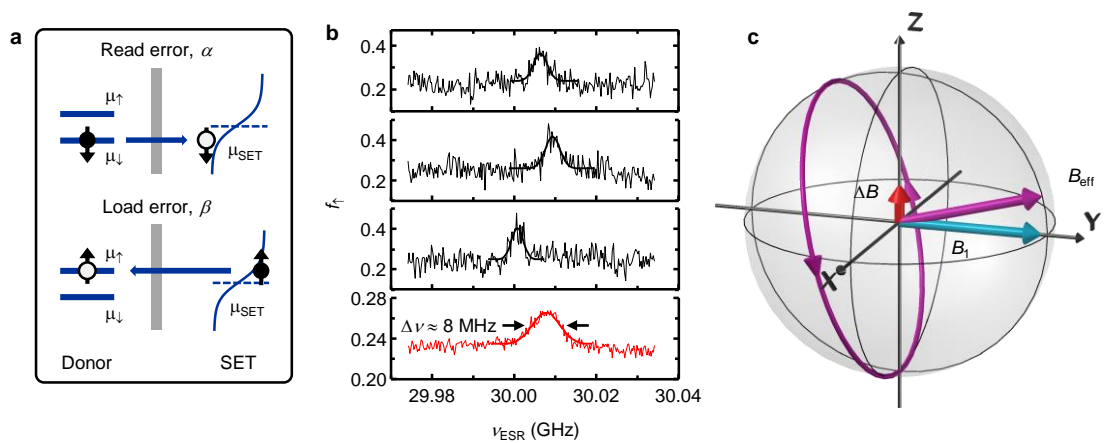


Figure 4.8: Qubit fidelity analysis. **a**, Mechanisms by which read (top) and load (bottom) errors are produced as a result of thermal broadening in the SET island (discussed in the main text). The solid circles represent full electron states with spin indicated by the arrow, whilst the empty circles signify unoccupied states. **b**, Sweeps of the frequency ν_{ESR} in the vicinity of the nuclear spin-up ESR transition ν_{e2} . The top three traces are individual sweeps where f_{\uparrow} at each ν_{ESR} is calculated from 250 single-shot measurements. The bottom trace is an average of 100 sweeps. **c**, Illustration of the rotation errors created by hyperfine field fluctuations of the ^{29}Si nuclear bath. For simplicity, only the z-component of the hyperfine field has been shown. The bath nuclear spins produce an offset from resonance, ΔB , which causes rotations about a new axis aligned with B_{eff} .

denotes the probability of incorrectly initializing the qubit in the spin-up state. The probability α of incorrectly identifying a $|\downarrow\rangle$ state as a $|\uparrow\rangle$ state during the read phase (as result of this thermally-activated tunneling) was given as a by-product of the Rabi oscillation simulations in Section 4.4.

We now define a total measurement error for both $|\downarrow\rangle$ and $|\uparrow\rangle$ electrons by combining the electrical and thermal contributions. We denote $e_{\downarrow(\uparrow)}$ as the total error involved in measuring a $|\downarrow\rangle$ ($|\uparrow\rangle$) electron, and make the following additional definitions,

$X \Rightarrow$ Incorrectly identify a spin-down electron due to noise exceeding the current threshold

$Y \Rightarrow$ Spin-down electron tunnels to the SET island due to thermal broadening

$Z \Rightarrow$ Incorrectly identify a spin-up electron as a result of the signal not reaching the current threshold

Using the fact that X and Y are independent events, but not mutually exclusive, we have,

$$\begin{aligned}
 e_{\downarrow} &= P(X \cup Y) \\
 &= P(X) + P(Y) - P(X \cap Y) \\
 &= P(X) + P(Y) - P(X)P(Y) \\
 &= \gamma_{\downarrow} + \alpha - \gamma_{\downarrow}\alpha
 \end{aligned} \tag{4.8}$$

$$\begin{aligned}
 e_{\uparrow} &= P(Z) \\
 &= \gamma_{\uparrow}
 \end{aligned} \tag{4.9}$$

This allows us to express the average measurement fidelity as

$$\begin{aligned}
 F_M &= 1 - \frac{(e_{\downarrow} + e_{\uparrow})}{2} \\
 &= 1 - \frac{\gamma + \alpha(1 - \gamma_{\downarrow})}{2}
 \end{aligned} \tag{4.10}$$

For the $P_{\text{ESR}} = 10$ dBm Rabi data, we find that $\alpha = 28(1)\%$. The exact value of α (and β) varies slightly from measurement to measurement, as it depends on the tuning of the electron electrochemical potentials with respect to the SET island. With (4.10), we find an average measurement fidelity of $F_M = 77(2)\%$.

4.6.2 Initialization Fidelity

Another by-product of the Rabi simulations was the parameter β . This represents the probability of loading a $|\uparrow\rangle$ electron (incorrect qubit initialization). We found $\beta = 1\%$ with a standard deviation of 9% (from the $P_{\text{ESR}} = 10$ dBm Rabi

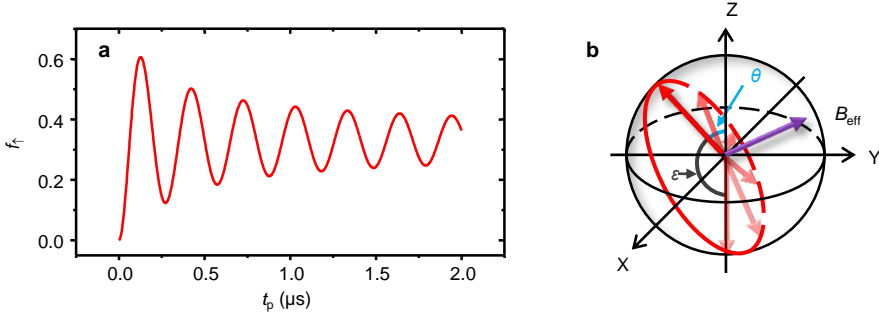


Figure 4.9: Pulse error analysis. **a**, Rabi simulation of the $P_{\text{ESR}} = 10$ dBm data with measurement and resonance offset related errors removed ($\alpha = \beta = 0$, $F_{\uparrow} = 1$ and $\mu = 0$). **b**, Bloch sphere illustrating the effect on control pulses of a B_{eff} tilted out of the XY-plane.

simulation), giving an initialization fidelity of $F_I = 1 - \beta \geq 90\%$.

The small value of β extracted is consistent with how the measurement is performed. In the experiment we tune the device such that a small amount of random telegraph signal (RTS) exists in the read phase (μ_{SET} is closer to μ_{\downarrow} than μ_{\uparrow} in Fig. 4.8a), resulting in a low probability of initializing in the $|\uparrow\rangle$ state.

4.6.3 Control Fidelity

The qubit control fidelity F_C is reduced by random field fluctuations ΔB from the ^{29}Si nuclear bath spins. These produce an effective field B_{eff} in the rotating frame that is tilted out of the XY-plane (Fig. 4.8c), and lead to imperfect pulses. We now estimate the strength of these fluctuations. Figure 4.8b presents a series of ESR spectra, where the electron spin-up fraction is monitored as a function of the microwave frequency. The top three traces of Fig. 4.8b contain individual sweeps with each point obtained over a timescale of ~ 250 ms. As described in Section 4.4, we attribute the shift in peak position between sweeps to slow fluctuations of a few strongly-coupled ^{29}Si nuclei, with hyperfine coupling strengths on the order of ~ 1 MHz. The width of the peaks is most likely the result of distant,

4.6. Electron Spin Qubit Fidelity

weakly-coupled ^{29}Si nuclear spins that fluctuate on the single-shot timescale. The bottom trace of Fig. 4.8b contains an average of 100 sweeps, representing many nuclear spin configurations. From this we extract a full-width at half-maximum (FWHM) of $\Delta\nu = 7.5(5)$ MHz. This is consistent with the observed T_2^* , where $\Delta\nu = 1/(\pi T_2^*) = 6(1)$ MHz.

In Section 4.4 we described how to model the experimental data by including the effect of this fluctuating Overhauser field $\Delta B(t)$, plus all the electrical and thermal contributions to the measurement and initialization errors. Once the model has been matched to the experiment, we may remove all the measurement and initialization errors to extract the control fidelity, i.e. the Rabi rotation errors occurring solely as a consequence of the random Overhauser field. We use the data set with microwave power $P_{\text{ESR}} = 10$ dBm that produced the largest B_1 achieved (0.12 mT), and fix $\mu = 0$, $\alpha = \beta = 0$ and $F_\uparrow = 1$ to remove the effect of the measurement process. We set the standard deviation for the Gaussian distribution of detunings to match the ESR FWHM extracted above ($\sigma = \Delta\nu / (2\sqrt{2 \ln 2}) = 3.2(2)$ MHz) and obtain the Rabi oscillations shown in Fig. 4.9a. The first peak of this plot gives an electron spin-up fraction of ≈ 0.6 . This is the average maximum spin-up fraction for an intended π rotation. Representing the state here as $|\Psi(t_\pi)\rangle = \eta|\downarrow\rangle + \kappa|\uparrow\rangle$, we find the average maximum tip angle ε (Fig. 4.9b) to be,

$$|\kappa|^2 = \cos^2\left(\frac{\theta}{2}\right) = 0.6$$

$$\theta = 2 \cos^{-1}\left(\sqrt{0.6}\right) = 78^\circ$$

$$\varepsilon = 180^\circ - \theta = 102^\circ$$

Thus, for an attempted 180° rotation we achieve $102(3)^\circ$ on average. This gives an average control fidelity of $F_C = \frac{\varepsilon}{180^\circ} = 57(2)\%$.

4.7 Conclusion

The processes that contribute to the measurement, initialization and control fidelity degradation can be mitigated with foreseeable adjustments to the device architecture and experimental setup. A low B_0 (~ 1 T) was necessary in these experiments in order to operate at ESR frequencies which produced a sufficiently high B_1 . This had the consequence of lowering E_Z with respect to $k_B T_{\text{el}}$, decreasing the measurement fidelity relative to the spin readout measurements presented in Chapter 3. Significant improvements in the read/load errors would follow from enhanced electrical filtering to lower the electron temperature, thus enabling the high readout fidelities ($> 90\%$) already achieved. Moving to an enriched ^{28}Si (nuclear spin-zero) substrate [149] would remove the primary source of rotation angle error, and allow access to the exceptional coherence times already demonstrated in bulk-doped samples [83].

Future experiments will focus on the coupling of two donor electron spin qubits through the exchange interaction [68], a key requirement in proposals for

4.7. Conclusion

scalable quantum computing architectures in this system [70]. Taken together with the single-atom doping technologies [66, 67] now demonstrated in silicon, the advances reported here open the way for a spin-based quantum computer utilizing single atoms, as first envisaged by Kane [68] more than a decade ago.

Chapter 5

^{31}P Nuclear Spin Qubit

A single nuclear spin holds the promise of being a long-lived quantum bit or quantum memory, with the high fidelities required for fault-tolerant quantum computing. We show here that such promise could be fulfilled by a single phosphorus (^{31}P) nuclear spin in a silicon nanostructure. By integrating single-shot readout of the electron spin with on-chip electron spin resonance, we demonstrate the quantum non-demolition, electrical single-shot readout of the nuclear spin, with readout fidelity better than 99.8% – the highest for any solid-state qubit. Quantum jumps of the nuclear spin are observed and their origins discussed and analyzed. The single nuclear spin is then operated as a qubit by applying coherent radiofrequency (RF) pulses. For an ionized ^{31}P donor we find a nuclear spin coherence time of 60 ms and a 1-qubit gate control fidelity exceeding 98%. These results demonstrate that the dominant technology of modern electronics can be adapted to host a complete electrical measurement and control platform for nuclear spin-based quantum information processing.

Parts of this chapter have been published in:

Pla, J. J., Tan, K. Y., Dehollain, J. P., Lim, W. H., Morton, J. J. L., Zwanenburg, F. A., Jamieson, D. N., Dzurak, A. S. and Morello, A. *Nature*, in the press (2013).

5.1 Introduction

Quantum computers have the potential to revolutionize aspects of modern society from fundamental science and medical research [15–17] to data analysis [13]. The successful demonstration of such a machine depends on the ability to perform high-fidelity control and measurement of individual qubits [18] – the building blocks of a quantum computer. Errors introduced by quantum operations and measurements can be mitigated by employing quantum error correction protocols [80], provided that the probabilities of the errors occurring are below certain stringent thresholds [150]. To date, the state-of-the-art in high-fidelity qubit control and readout has been defined by laser cooled atoms in electromagnetic traps [151, 152] – a result made possible because of their extreme isolation in a near perfect vacuum.

Qubits based on physical systems in the solid-state [27, 47, 135] are attractive because of their potential for scalability using modern integrated circuit fabrication technologies. However, they tend to exhibit much lower system fidelities owing to interactions with their host environment [72]. An ability to combine the control and measurement fidelities of trapped atoms with the scalability benefits inherent to solid-state implementations is therefore highly desirable. The nuclear spin of a single atom is a promising candidate in this regard; it represents a simple, well-isolated quantum system. It can be oriented and caused to precess using combinations of static and oscillating magnetic fields [153]. The spin orientation persists for a very long time, even when the nucleus is hosted by a crystal [48] or a molecule [154]. This property has been exploited for a variety of applications, ranging from magnetic resonance imaging (MRI) [155] to the execution of quantum algorithms [156].

5.2. Electrical Single-Shot Nuclear Spin Readout

One of the earliest proposals for quantum computing in the solid-state advocated the use of the nuclear spin of individual ^{31}P dopant atoms in silicon to encode and process quantum information [68]. Silicon is an ideal platform for spin-based quantum information processing because it can be enriched in the nuclear spin-zero ^{28}Si isotope [149, 157], providing an effective “semiconductor vacuum” and very long spin coherence times. Experiments in bulk phosphorus-doped isotopically-enriched silicon ($^{28}\text{Si:P}$) have already highlighted the potential of this system, where the ^{31}P nuclear spin has been implemented as a quantum memory [92] and as a qubit with extraordinary coherence lifetimes > 180 s (Ref. 158). However, due to detection limitations, experiments have so far only been carried out on large ensembles of ^{31}P nuclei, typically several billion in number [158, 159]. To realize nuclear spin-based solid-state quantum computing, one must first isolate, measure and control individual nuclear spins.

Here we demonstrate the readout and coherent manipulation of a single ^{31}P nuclear spin qubit in a silicon chip. As with modern microelectronic circuits, our qubit operations are performed electrically through the application of on-chip voltage and current signals. We show that this solid-state system is capable of realizing fidelities approaching those in vacuum-based ion-trap qubits, raising the prospects for scalable and fault-tolerant quantum computation in silicon.

5.2 Electrical Single-Shot Nuclear Spin Readout

Measuring the state of a single nuclear spin is challenging due to its weak magnetic moment. In the solid-state, this has only been achieved in the nitrogen-vacancy

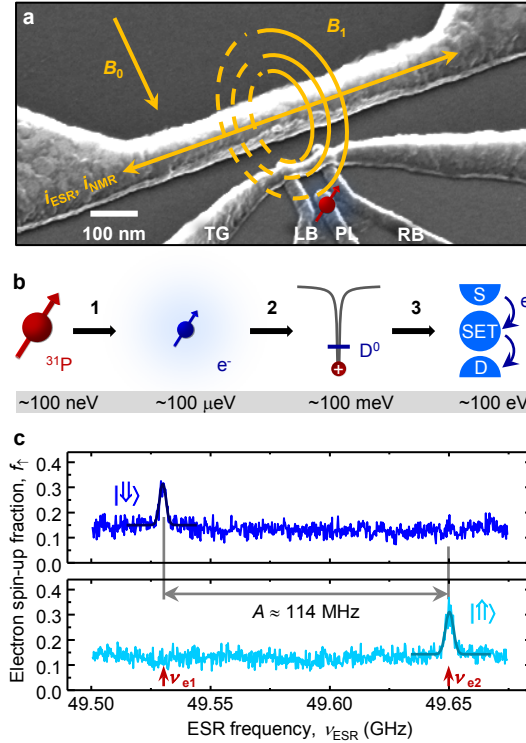


Figure 5.1: Qubit nanostructure and spin transitions. **a**, Scanning electron micrograph of the active area of the qubit device, showing an implanted donor (donor as red arrow), the SET and the short-circuit termination of the microwave line. The device is mounted in a dilution refrigerator with electron temperature $\sim 300 \text{ mK}$, and subject to static magnetic fields between 1.0 and 1.8 T . **b**, ^{31}P nuclear spin readout through our three stage amplification process. (1) The nuclear spin state ($\sim 100 \text{ neV}$ energy splitting) is mapped onto the electron spin state ($\sim 100 \mu\text{eV}$ energy splitting) by performing ESR. (2) The electron spin state is projected onto a charge state of the donor ($\sim 50 \text{ meV}$) by using spin-to-charge conversion. (3) The SET provides a current that is dependent on the donor charge state, thus revealing the electron and nuclear spin states. In particular, the signal is a current pulse (see Section 3.8), which has a total energy of (current \times voltage \times duration) $\sim 100 \text{ eV}$ under typical experimental conditions. **c**, ESR spectra obtained at $B_0 = 1.77 \text{ T}$ by scanning the microwave frequency and monitoring the electron spin-up fraction f_\uparrow . The top trace corresponds to an active ν_{e1} ESR transition (nuclear spin state $|\downarrow\downarrow\rangle$) and the bottom trace to an active ν_{e2} ESR transition (nuclear spin state $|\uparrow\uparrow\rangle$).

5.2. Electrical Single-Shot Nuclear Spin Readout

center in diamond [160], with optical detection, and on a rare earth terbium ion by performing electrical transport measurements through a single molecule [154]. In both of these cases, a coupled electron spin was used to read out the nuclear spin, and thus the ability to measure a single electron spin was prerequisite.

One of the most versatile and successful methods of electrically measuring single electron spins in the solid-state relies on a process known as spin-to-charge conversion [107]. The electron is displaced to a different location depending on its spin state, and the resulting change in the local potential can be detected using a nano-scale electrometer. This readout method can be applied to the electron spin of a ^{31}P donor in silicon (refer to Chapter 3), and forms the basis of our nuclear spin readout.

We employ the same device as used in Chapter 4, which consists of ion-implanted phosphorus donors [66] tunnel-coupled to a silicon MOS single-electron transistor (Fig. 5.1a). With this device we are able to read out both the electron and nuclear spins electrically. To achieve the single-shot readout of a ^{31}P nuclear spin, we implement a three-stage process (Fig. 5.1b) which amplifies the nuclear spin state energy splitting (~ 100 neV) by a factor of order 10^9 . In the first stage, we exploit electron spin resonance to map the nuclear spin state onto the electron spin. The second stage involves performing spin-to-charge conversion, which projects the electron spin state onto a charge state of the ^{31}P donor. Finally, we utilize the SET to provide a current, dependent upon the donor charge state, with a total signal energy of ~ 100 eV (see Fig. 5.1b caption) under typical experimental conditions.

The ^{31}P nuclear spin readout experiment begins by performing ESR on its bound donor electron (refer to Section 4.2), which is manipulated using a reso-

nant microwave excitation and measured in a single shot with the adjacent SET. The microwave pulses are delivered by a custom designed, on-chip broadband planar transmission line, as described in Section 2.4. The hyperfine coupling A between the electron and nuclear spins produces an effective magnetic field on the electron, which can add to or subtract from the external field B_0 depending on the orientation of the nuclear spin. Assuming the high magnetic field limit $\gamma_e B_0 \gg A$, the two possible ESR frequencies (see Section 1.4) become: $\nu_{e1} \approx \gamma_e B_0 - A/2$ for nuclear spin $|\Downarrow\rangle$; and $\nu_{e2} \approx \gamma_e B_0 + A/2$ for nuclear spin $|\Uparrow\rangle$. In a single-atom experiment, if we assume the ESR measurement duration to be much shorter than the nuclear spin flip time, then we expect only one active ESR frequency at any instant. Detecting electron spin resonance at the frequency ν_{e1} therefore indicates that the nuclear spin is in state $|\Downarrow\rangle$, whereas detection at ν_{e2} implies the nuclear spin is $|\Uparrow\rangle$.

Having identified the two resonance frequencies through an ESR experiment (see Fig. 5.1c and also Section 4.2), we performed repeated measurements of the nuclear spin state (Fig. 5.2a) by toggling the microwave frequency ν_{ESR} between ν_{e1} and ν_{e2} , averaging 250 electron spin measurements at each point (acquisition time 260 ms) to obtain the electron spin-up fraction f_{\uparrow} . In order to maximize the probability of flipping the electron spin in each shot, we execute a fast adiabatic passage by applying a frequency chirp centered about the ESR transition [161]. If the quantity $\Delta f_{\uparrow} = f_{\uparrow}(\nu_{e2}) - f_{\uparrow}(\nu_{e1})$ is positive, we assign the nuclear state $|\Uparrow\rangle$, and vice versa. A histogram of Δf_{\uparrow} (Fig. 5.2d) shows two well-separated Gaussian peaks, corresponding to the two possible nuclear orientations. The widths of the peaks result from a combination of effects including: thermal broadening (caused by microwave-induced heating), charge fluctuations (which alter the de-

vice biasing) and an imperfect adiabatic passage. These effects act to reduce the signal-to-noise ratio (SNR) of the measurement. The nuclear spin readout error (Fig. 5.2e) is obtained by fitting the two peaks and integrating each Gaussian beyond a discrimination threshold Δf_{th} . At the optimal value of $\Delta f_{\text{th}} = -0.025$, the SNR-limited readout error is 2×10^{-7} . A further analysis of measurement errors is presented later in Section 5.10.

5.3 Quantum Jumps of the Nuclear Spin State

We observe that the nuclear spin state remains unchanged for several minutes before exhibiting a “quantum jump” to the opposite state [160]. From Fig. 5.2b, it is evident that the nuclear spin is predominantly polarized in the $|\uparrow\uparrow\rangle$ state. We attribute this phenomenon to an electron-nuclear spin flip-flop process, in which the energy difference $E_{\uparrow\downarrow} - E_{\downarrow\uparrow}$ (i.e. between states $|\uparrow\downarrow\rangle$ and $|\downarrow\uparrow\rangle$) is released to the phonon bath. The spin-phonon coupling may arise from the modulation of the hyperfine coupling caused by lattice deformation [162]. The same mechanism was invoked to explain the ~ 100 s decay time of spin polarization stored in a ^{31}P ensemble [159]. Since $E_{\uparrow\downarrow}E_{\downarrow\uparrow} \gg k_B T$ in our experiment, this process acts only in the direction $|\uparrow\downarrow\rangle \rightarrow |\downarrow\uparrow\rangle$ (i.e., only spontaneous emission of phonons occurs), and should not be responsible for the observed nuclear spin jumps from $|\uparrow\uparrow\rangle$ to $|\downarrow\downarrow\rangle$.

We have established the cause of the $|\uparrow\uparrow\rangle \rightarrow |\downarrow\downarrow\rangle$ transition by modifying the rate of donor ionization/neutralization. We control the ionization/neutralization rate $\Gamma_{\text{ion/neut}}$ by adding to the measurement an additional “resonant tunneling” phase, where we align the donor electron spin-down electrochemical potential μ_{\downarrow}

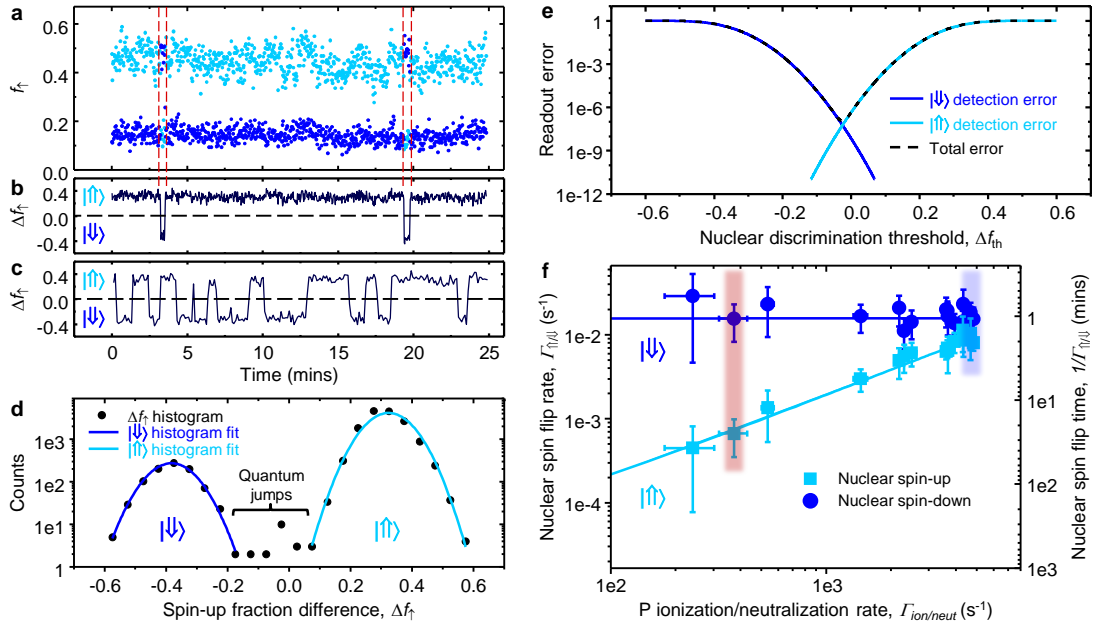


Figure 5.2: Nuclear spin quantum jumps, lifetimes and readout error. **a**, Repetitive single-shot measurements of the nuclear spin state, obtained by toggling ν_{ESR} between $\nu_{e1} = 49.5305$ GHz (dark blue) and $\nu_{e2} = 49.6445$ GHz (light blue), and recording the electron spin-up fraction f_{\uparrow} . Each data point represents the average f_{\uparrow} over 250 measurements. **b**, Electron spin-up fraction difference, $\Delta f_{\uparrow} = f_{\uparrow}(\nu_{e2}) - f_{\uparrow}(\nu_{e1})$, for the data in panel a. $\Delta f_{\uparrow} > 0$ indicates nuclear spin $|\uparrow\rangle$, and vice versa. **c**, Δf_{\uparrow} in an experiment with an additional resonant tunneling phase, to enhance the electron ionization/neutralization rate (see text). **d**, Histograms of Δf_{\uparrow} for the data in panel b, showing two well-separated Gaussian peaks, each corresponding to a nuclear spin state as indicated. The counts obtained for $-0.015 < \Delta f_{\uparrow} < 0.05$ are attributed to nuclear spin quantum jumps occurring during the measurement. **e**, Readout errors as a function of the detection threshold for Δf_{\uparrow} . **f**, Nuclear spin flip rates $\Gamma_{\uparrow/\downarrow}$ as a function of the donor ionization/neutralization rate $\Gamma_{\text{ion/neut}}$. The light blue line is a fit to $\Gamma_{\uparrow} = \Gamma_0 + p\Gamma_{\text{ion/neut}}$, with $p = 1.91(8) \times 10^{-6}$. The dark blue line is a constant $\Gamma_{\downarrow} = 1.54(17) \times 10^{-2} \text{ s}^{-1}$. The red and blue shading indicate the values obtained from the data sets in panels b and c, respectively. Calculation of the error bars is described in Section 5.4.

5.3. Quantum Jumps of the Nuclear Spin State

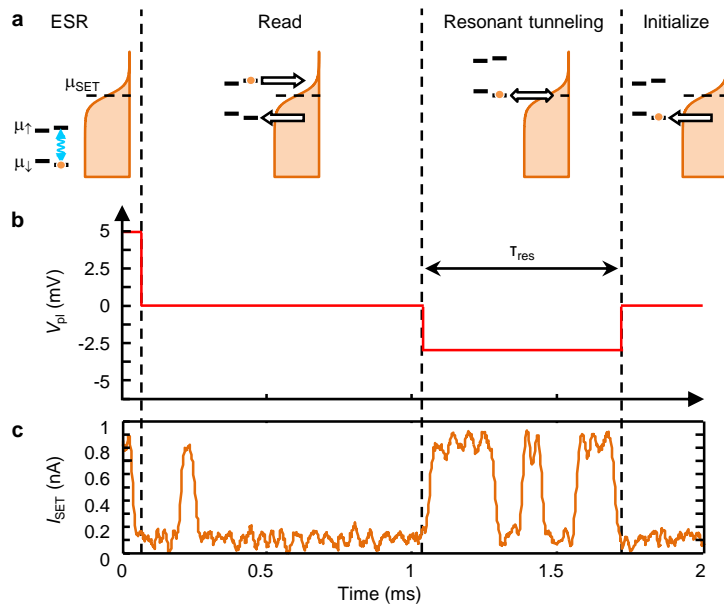


Figure 5.3: Pulse protocol for the modified quantum jumps measurement. **a**, Sketch of the (spin-dependent) electrochemical potentials of the donor electron $\mu_{\downarrow/\uparrow}$ and SET μ_{SET} during the measurement process. The pulse levels are chosen such that: $\mu_{\downarrow/\uparrow} \ll \mu_{\text{SET}}$ for the ESR phase, $\mu_{\downarrow} < \mu_{\text{SET}} < \mu_{\uparrow}$ for the read and initialize phases, and $\mu_{\downarrow} \approx \mu_{\text{SET}}$ for the resonant tunneling phase. **b**, Plunger voltage pulse level and timing scheme. **c**, Sample response of the current through the SET I_{SET} to the above pulse protocol. The current peaks during the resonant tunneling phase *do not* correspond to readout of $|\uparrow\rangle$ electrons, but arise because of the allowed tunneling of $|\downarrow\rangle$ electrons to and from the SET island.

with that of the electrons in the SET island μ_{SET} . During this phase (where $\mu_{\downarrow} \approx \mu_{\text{SET}}$) spin-down electrons tunnel back and forth between the donor and the SET island (see Figs. 5.3a,b). The corresponding pattern of I_{SET} (Fig. 5.3c) resembles a random telegraph signal (RTS). Varying the duration of the resonant tunneling phase τ_{res} provides control of $\Gamma_{\text{ion/neut}}$, which allows us to probe the nuclear spin-up flip process (Section 5.5). The ionization/neutralization process can be viewed as a modulation of the hyperfine interaction between the electron and nuclear spins with dynamics governed by the tunneling electron, and is observed to decrease the $|\uparrow\rangle$ state lifetime (Fig. 5.2c).

In Fig. 5.2f we plot the lifetime of the nuclear $|\Downarrow\rangle$ and $|\Uparrow\rangle$ states as a function of the rate of donor ionization/neutralization $\Gamma_{\text{ion/neut}}$. We find that the lifetime of the nuclear $|\Downarrow\rangle$ is approximately independent of $\Gamma_{\text{ion/neut}}$, as expected if the process is dominated by electron-nuclear spin flip-flops with phonon emission. Conversely, the lifetime of the nuclear $|\Uparrow\rangle$ is longer and inversely proportional to $\Gamma_{\text{ion/neut}}$. The results in Fig. 5.2f are accurately reproduced by a simulation where the hyperfine coupling is modulated in a random process that replicates the electron tunneling times as extracted from the measurements, as presented in Section 5.5.

5.4 Error Bars in the Nuclear Spin Flip Rates

Here we describe the estimation of errors for the nuclear spin flip rate measurements of Fig. 5.2f. Each point in Fig. 5.2f represents the inverse decay time (the rate, $\Gamma_{\Uparrow/\Downarrow}$) of a histogram of flip times (t_{flip}) extracted from data similar to that in Figs. 5.2b and 5.2c (see Fig. 5.4).

The uncertainty in the flip rate comes from having a finite sample size of flip times. With a small sample size, the choice of histogram bin size can affect the apparent $\Gamma_{\uparrow/\downarrow}$. We first calculate an optimum bin width $W = 2(IQR)L^{-\frac{1}{3}}$, where IQR is the interquartile range and L is the sample size. We then extract $\Gamma_{\uparrow/\downarrow}$ from a number of histograms using a range of bin sizes centered around the optimum. For each we also find the 95% confidence interval ε_{fit} of the fitting parameter $\Gamma_{\uparrow/\downarrow}$. The total error (vertical bar) is then given by equation Eq. 5.1, which is the geometric sum of: (i) the 95% confidence interval ε_{bin} of the fluctuations in $\Gamma_{\uparrow/\downarrow}$ resulting from different histogram bin sizes; and (ii) the average ε_{fit} from all histograms. We neglect experimental error due to the sampling resolution of the quantum jumps measurements, since the minimum nuclear flip time (~ 1 minute) is much greater than the maximum sample time (~ 1.5 seconds for the longest resonant tunneling measurement).

$$\varepsilon = \sqrt{\varepsilon_{\text{bin}}^2 + \overline{\varepsilon_{\text{fit}}}^2} \quad (5.1)$$

The error in $\Gamma_{\text{ion/neut}}$ (horizontal bar) results from small fluctuations in the sample biasing over the duration of each measurement. For each $\Gamma_{\uparrow/\downarrow}$ data point, we count the total number of ionization/neutralization events per single-shot and calculate the standard deviation over all shots $\sigma_{\text{ion/neut}}$. We then convert $\sigma_{\text{ion/neut}}$ into a rate by dividing by the length of each single-shot.

5.5 Nuclear Spin-Up Flip Mechanisms

As shown in Fig. 5.2f, the spin flip rate for the nuclear spin-up state Γ_{\uparrow} is found to be proportional to the ionization/neutralization rate of the donor $\Gamma_{\text{ion/neut}}$, with

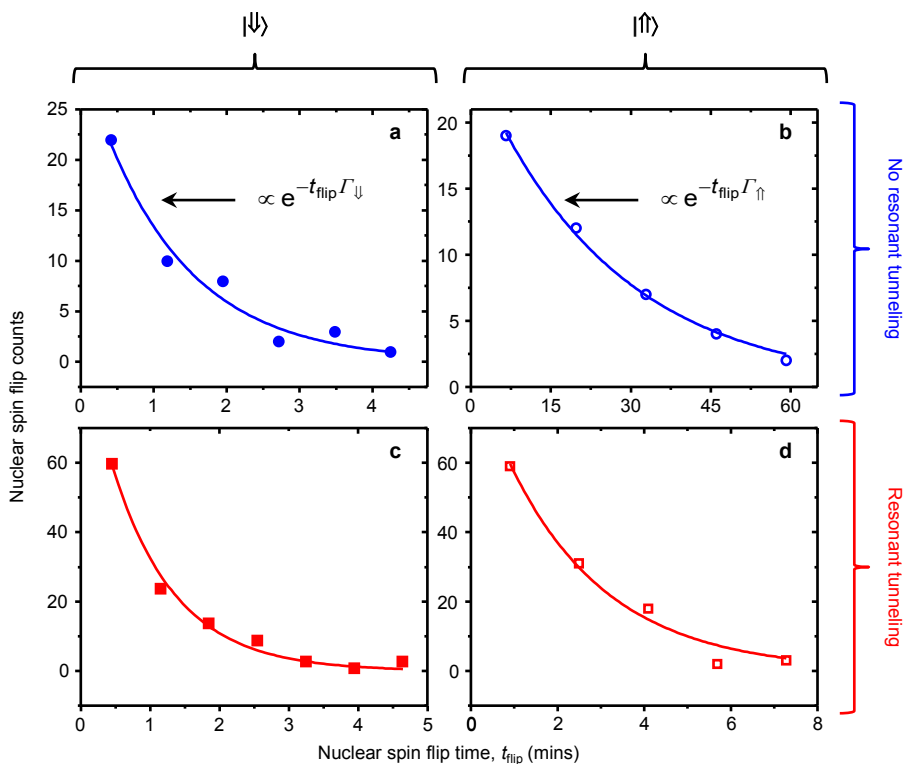


Figure 5.4: Nuclear spin-up and spin-down flip time histograms. **a-b**, Nuclear spin-down (a) and spin-up (b) flip time histograms, extracted from the data of Fig. 5.2b in the main text. Exponential fits are used to determine the nuclear spin flip rates $\Gamma_{\uparrow/\downarrow}$. **c-d**, Nuclear spin-down (c) and spin-up (d) flip time histograms, extracted from the data of the resonant tunneling experiment of Fig. 5.2c. It is evident from the histograms that the addition of the resonant tunneling phase drastically increases Γ_{\uparrow} , but has little effect on Γ_{\downarrow} .

a proportionality constant $p = 1.91(8) \times 10^{-6}$. The ionization/neutralization process is inherent to the way we perform electron spin readout, but it can also be enhanced by including a resonant tunneling phase, as described in Section 5.3 above. In this section we present two mechanisms that may be responsible for the observed flips of the nuclear spin-up state.

5.5.1 Isotropic Hyperfine Coupling

The effect of the resonant electron tunneling is to randomly modulate the hyperfine interaction between the electron spin S and nuclear spin I from being fully on to fully off (or zero). We model this process by multiplying the S terms in the spin Hamiltonian of the neutral donor (Eq. 5.2a) by $\Xi(t)$, a time-dependent variable that switches randomly between 0 and 1 with statistics that match that of the tunneling electron. Assuming the hyperfine coupling to be purely isotropic, we can express the time-dependent Hamiltonian as Eq. 5.2c.

$$\mathcal{H}_{\text{neut}} = \gamma_e B_0 S_z - \gamma_n B_0 I_z + S \cdot \underline{\underline{A}} \cdot I \quad (5.2a)$$

$$\mathcal{H}_{\text{ion}} = -\gamma_n B_0 I_z \quad (5.2b)$$

$$\mathcal{H}(t) = \Xi(t) \gamma_e B_0 S_z - \gamma_n B_0 I_z + A_{\parallel}(t) (S_x I_x + S_y I_y + S_z I_z) \quad (5.2c)$$

where $A_{\parallel}(t) = A_{\parallel}\Xi(t)$ is the modulated isotropic hyperfine coupling. Here $\mathcal{H}(t)$ will be equal to $\mathcal{H}_{\text{neut}}$ (Eq. 5.2a) or \mathcal{H}_{ion} (Eq. 5.2b), depending on the value of $\Xi(t)$ at a given time t .

We simulate the resonant tunneling experiments by creating a sequence $\Xi(t)$ that consists of the three phases presented in Section 5.3. In the first phase we model the electron spin readout process, where a single ionization/neutralization

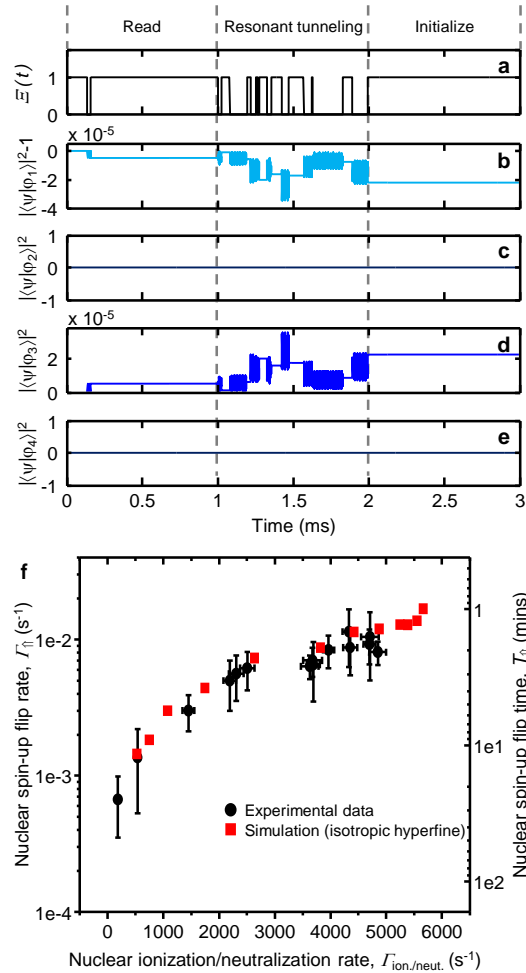


Figure 5.5: Donor ionization time dependence and neutral donor eigenstate probability evolution. **a**, An example of the electron tunneling dynamics. Here $\Xi(t) = 1$ implies the donor is neutral and $\Xi(t) = 0$ implies that it is ionized. The single ionization/neutralization event in the read phase occurs with an average probability $P_{\text{read}} = 0.5$, as found from experiment. **b-e**, Time evolution of the probability weighting of the neutral donor eigenstates $|\langle \Psi(t) | \varphi_n \rangle|^2|$. **f**, Comparison of the simulated and experimental nuclear spin-up flip rate Γ_{\uparrow} against donor ionization/neutralization rate $\Gamma_{\text{ion/neut.}}$.

5.5. Nuclear Spin-Up Flip Mechanisms

event occurs with a probability P_{read} and tunnel times $\tau_{\text{read}}^{\text{out}}$ and $\tau_{\text{read}}^{\text{in}}$. Next we generate a random telegraph signal that lasts for the entire resonant tunneling phase (duration τ_{res}) and has statistics determined by the tunnel times $\tau_{\text{res}}^{\text{out}}$ and $\tau_{\text{res}}^{\text{in}}$. Finally, in the third phase we force the donor to be neutral ($\Xi(t) = 1$). We extract the exact tunnel times from the experimental data and find $\tau_{\text{read}}^{\text{out/in}} = 300/30 \mu\text{s}$ (see Section 4.6.1) and $\tau_{\text{res}}^{\text{out/in}} = 50/90 \mu\text{s}$. Figure 5.5a displays a sample trace of $\Xi(t)$ over the read, resonant tunneling and initialization phases for $\tau_{\text{res}} = 1 \text{ ms}$. As in the experiment, we can simply count the total number of ionization/neutralization events in Fig. 5.5a to calculate the rate $\Gamma_{\text{ion/neut}}$.

In order to estimate the nuclear spin-up flip time for a given $\Gamma_{\text{ion/neut}}$, we need the exact eigenstates of the neutral donor Hamiltonian presented in Section 1.4 (Eq. 1.3) and reproduced here:

$$|\varphi_1\rangle = \cos(\eta/2) |\downarrow\uparrow\rangle - \sin(\eta/2) |\uparrow\downarrow\rangle$$

$$|\varphi_2\rangle = |\downarrow\downarrow\rangle$$

$$|\varphi_3\rangle = \cos(\eta/2) |\uparrow\downarrow\rangle + \sin(\eta/2) |\downarrow\uparrow\rangle$$

$$|\varphi_4\rangle = |\uparrow\uparrow\rangle$$

where $\tan(\eta) = A_{\parallel}/(\gamma_{+}B_0)$, $B_0 \approx 1.8 \text{ T}$ and we take the isotropic hyperfine component to be equal to the measured hyperfine splitting $A_{\parallel} = 114.3 \text{ MHz}$ (see Section 5.6 below). Under our experimental conditions, $\tan(\eta) \approx 0$, which means that $|\varphi_1\rangle \approx |\downarrow\uparrow\rangle$ and $|\varphi_3\rangle \approx |\uparrow\downarrow\rangle$. However, in this model the nuclear flipping process is caused precisely by the fact that $|\downarrow\uparrow\rangle$ and $|\uparrow\downarrow\rangle$ are not *exact* eigenstates of the neutral donor Hamiltonian. This fact can be traced back to the presence of the terms $S_x I_x + S_y I_y$, which do not commute with I_z . In other

words, I_z is not a constant of motion for the neutral donor. Conversely, \mathcal{H}_{ion} does not contain such terms, and I_z becomes a constant of motion.

We start the system in the exact eigenstate $|\Psi(t=0)\rangle = |\varphi_1\rangle$ and evolve it over small time intervals Δt with the time-dependent Hamiltonian $\mathcal{H}(t)$, which has been calculated using the predetermined $\Xi(t)$. After each time increment we calculate the probability of finding the state $|\Psi(t)\rangle$ in each of the neutral donor eigenstates $|\langle\Psi(t)|\varphi_n\rangle|^2$. Figures 5.5b-e show the evolution over one complete cycle of $\mathcal{H}(t)$. When the donor becomes ionized, the state $|\Psi(t)\rangle$ is no longer an exact eigenstate of the system Hamiltonian \mathcal{H}_{ion} (since $|\langle\varphi_1|I_z|\varphi_1\rangle| < 0.5$) and we observe small probability oscillations between $|\langle\Psi(t)|\varphi_1\rangle|^2$ and $|\langle\Psi(t)|\varphi_3\rangle|^2$. At the end of the cycle (which has a duration τ) we find a non-zero value of $|\langle\Psi(\tau)|\varphi_3\rangle|^2$ which corresponds to a probability of flipping the nuclear spin from $|\uparrow\rangle$ to $|\downarrow\rangle$. We generate 250 random evolutions using a different $\Xi(t)$ sequence each time and initializing the state $|\Psi(t=0)\rangle = |\varphi_1\rangle$ at the beginning of each run. Taking the average of the $|\langle\Psi(t)|\varphi_n\rangle|^2$ evolutions over the 250 runs, we calculate the $|\uparrow\rangle$ flip time using:

$$T_{\uparrow} = \frac{\tau}{\overline{|\langle\Psi(\tau)|\varphi_3\rangle|^2}}$$

where $\overline{|\langle\Psi(\tau)|\varphi_3\rangle|^2}$ is the average probability over the runs of finding the final state in $|\varphi_3\rangle$. We vary τ_{res} over the range explored experimentally (0 – 4 ms) and plot the resulting T_{\uparrow} 's as a function of $\Gamma_{\text{ion/neut}}$ in Fig. 5.5f. The model involves no free fitting parameters, and produces results that are in remarkable agreement with the experimental data.

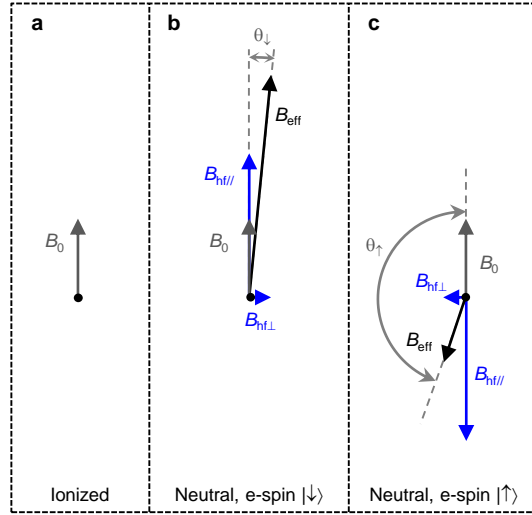


Figure 5.6: Magnetic field angles for ionized and neutral donor. **a**, Ionized donor: $B_{\text{eff}} = B_0$. **b-c**, B_{eff} is the vector sum of B_0 and B_{hf} , forming angles θ_{\downarrow} or θ_{\uparrow} with respect to the z-axis, depending on the electron spin state.

5.5.2 Anisotropic Hyperfine Coupling

An alternative explanation for the observation that $\Gamma_{\uparrow} \propto \Gamma_{\text{ion/neut}}$ is to assume the existence of a non-diagonal (anisotropic) component of the hyperfine coupling tensor $\underline{\underline{A}}$. In bulk phosphorus-doped silicon samples, the hyperfine coupling is perfectly isotropic ($A_{\perp} = 0$). However, in a nanostructure, some degree of anisotropy could be expected as a result of distortions to the donor electron wavefunction [128, 163].

As a consequence of the random electron stripping in the resonant tunneling experiments, the nuclear spin experiences frequent sudden changes of the effective magnetic field it is subject to, $B_{\text{eff}} = B_0 + B_{\text{hf}}$, where $B_{\text{hf}} = \underline{\underline{A}}S/\gamma_n$ depends on the electron spin state, and becomes zero when the donor is ionized. If the hyperfine tensor $\underline{\underline{A}}$ is diagonal, then B_0 and B_{hf} are exactly parallel. Conversely, if $\underline{\underline{A}}$ contains a non-diagonal component, B_{hf} is slightly tilted from B_0 . Therefore B_{eff} (the field on the nucleus when the donor is neutral) and B_0 (the field

on the nucleus when the donor is ionized) are no longer parallel. After donor ionization, the nuclear spin precesses around a new axis (aligned with B_0), and when an electron returns onto the donor, the nuclear spin may be oriented along an axis which is not parallel to that of B_{eff} , thereby precessing further, and so on. Quantum mechanically, this means that the nuclear spin has a probability to flip, proportional to the square of the (small) angle between the directions of B_0 and B_{hf} . This is analogous to the problem of orthogonality blocking in the general theory of the spin bath [164], exemplified by the dynamics of nuclear spins coupled to a magnetic molecule undergoing spin tunneling [165].

To describe this effect with a simple model, we write the hyperfine tensor as:

$$\underline{\underline{A}} = \begin{pmatrix} A_{\parallel} & 0 & A_{\perp} \\ 0 & A_{\parallel} & 0 \\ A_{\perp} & 0 & A_{\parallel} \end{pmatrix}, \quad (5.3)$$

where $A_{\parallel} = 114.3$ MHz, and we leave the anisotropic component A_{\perp} as a free (small) parameter, to be determined by matching the experimental value of p (the $\Gamma_{\uparrow\uparrow}$ to $\Gamma_{\text{ion/neut}}$ proportionality constant). The corresponding components of the hyperfine field exerted by the electron on the nucleus are $B_{\text{hf}\parallel} = A_{\parallel}/2\gamma_n = 3.317$ T and $B_{\text{hf}\perp} = A_{\perp}/2\gamma_n$. Calling \hat{z} the unit vector along the direction of the external magnetic field B_0 (the [110] crystal axis in the plane of the chip), the total magnetic field applied to the nucleus is:

$$B_{\text{eff}} = (B_0 \pm B_{\text{hf}\parallel})\hat{z} \pm B_{\text{hf}\perp}\hat{x} \quad (\text{neutral}), \quad (5.4)$$

$$B_{\text{eff}} = B_0\hat{z} \quad (\text{ionized}), \quad (5.5)$$

5.5. Nuclear Spin-Up Flip Mechanisms

depending on the charge state of the donor. The + sign in equation 5.4 corresponds to the case for electron spin-down, and vice versa.

Figure 5.6 shows the three possible directions of the total field B_{eff} for ionized donor, neutral donor with electron spin $|\downarrow\rangle$, and neutral donor with electron spin $|\uparrow\rangle$. Let us assume the donor is initially ionized, and the nuclear spin is in the state $|\uparrow\rangle$, which is an *exact* eigenstate of \mathcal{H}_{ion} (Eq. (5.2b)). This means the nuclear spin is exactly quantized along the z-axis. If the donor is neutralized by loading an electron in the $|\downarrow\rangle$ state, the magnetic field suddenly switches to a new direction, tilted by an angle $\theta_{\downarrow} \approx B_{\text{hf}\perp}/(B_{\text{hf}\parallel} + B_0)$ from the z-axis, and the Hamiltonian becomes $\mathcal{H}_{\text{neut}}$ (Eq. (5.2a)). The consequence of this change of quantization axis is that the nuclear spin now starts to precess around the new direction of the total field.

Calling $|\tilde{\uparrow}\rangle$ and $|\tilde{\downarrow}\rangle$ the nuclear parts of the exact eigenstates of $\mathcal{H}_{\text{neut}}$, we may rewrite the state $|\uparrow\rangle$ in the new basis as:

$$|\uparrow\rangle = \cos \frac{\theta_{\downarrow}}{2} |\tilde{\uparrow}\rangle + \sin \frac{\theta_{\downarrow}}{2} |\tilde{\downarrow}\rangle \quad (5.6)$$

This means that the nuclear spin has a probability $p_{\text{flip}} = \sin^2(\theta_{\downarrow}/2)$ of having “flipped” to the $|\tilde{\downarrow}\rangle$ state. The exact dynamics of the nuclear spin can be rather complicated, but the order of magnitude of A_{\perp} can be obtained by identifying p_{flip} with $p/2$, since p represents the nuclear flipping probability for a complete cycle of ionization *plus* neutralization (which cause *two* changes of quantization axis). In summary:

$$p_{\text{flip}} = \frac{p}{2} = \sin^2 \frac{\theta_{\downarrow}}{2} \approx \frac{B_{\text{hf}\perp}^2}{4(B_0 + B_{\text{hf}\parallel})^2}, \quad (5.7)$$

$$A_{\perp} = 2\gamma_n B_{\text{hf}\perp} \approx 2\gamma_n \sqrt{2p}(B_0 + B_{\text{hf}\parallel}). \quad (5.8)$$

With $B_0 \approx 1.8$ T and $p \approx 2 \times 10^{-6}$ we obtain $A_{\perp} \approx 350$ kHz. This is likely to be an upper bound to the value of A_{\perp} necessary to explain the observed magnitude of Γ_{\uparrow} , since the change of quantization axis caused by the tunneling of a $|\uparrow\rangle$ electron is larger than that due to a $|\downarrow\rangle$, and additional nuclear flips may occur upon excitation of the electron spin through ESR pulses.

Given that we can accurately reproduce the nuclear spin flip times observed in the experiment by applying only the isotropic hyperfine terms (Section 5.5.1), we believe that mechanism to be primarily responsible for the $|\uparrow\rangle \rightarrow |\downarrow\rangle$ flips, with the anisotropic mechanism contributing to a lesser extent.

5.6 Single-Spin Nuclear Magnetic Resonance

By exploiting the broadband nature of our on-chip microwave transmission line, we perform a nuclear magnetic resonance experiment on the ^{31}P nuclear spin (Fig. 5.7). We expect two NMR frequencies depending on the state of the electron: $\nu_{n1} = A/2 + \gamma_n B_0$ when the electron spin is $|\downarrow\rangle$; and $\nu_{n2} = A/2\gamma_n B_0$ when the electron spin is $|\uparrow\rangle$ (Section 1.4). The nuclear resonance is detected by measuring the absolute difference in electron spin-up counts between the two ESR frequencies, $|\Delta f_{\uparrow}| = |f_{\uparrow}(\nu_{e2}) - f_{\uparrow}(\nu_{e1})|$, as a function of the NMR frequency ν_{NMR} . Off-resonance, we find the normal value $|\Delta f_{\uparrow}| \approx 0.4$, as observed in the nuclear spin readout experiments (Fig. 5.2b), because the nucleus retains its spin state for a very long time. Conversely, an 8 ms long resonant excitation randomizes the nuclear spin state, causing $|\Delta f_{\uparrow}|$ to drop towards zero. ν_{n1} is found by applying an NMR burst before the ESR excitation (Fig. 5.7a), whereas for ν_{n2} we swap the order of ESR and NMR, to achieve a higher probability of having the electron

5.6. Single-Spin Nuclear Magnetic Resonance

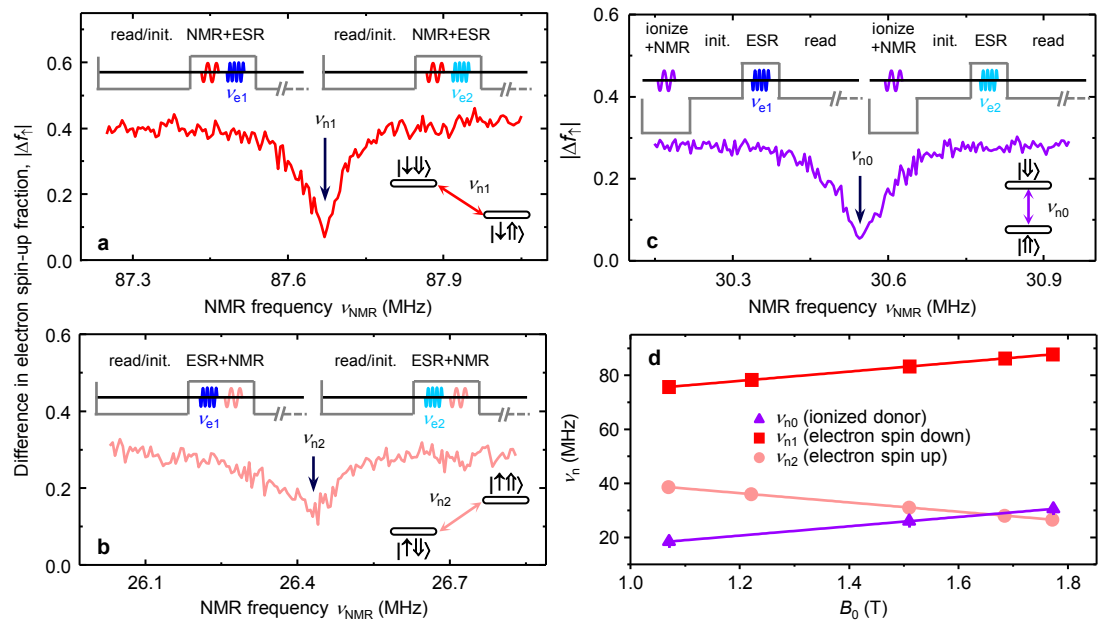


Figure 5.7: Nuclear magnetic resonance of a single ^{31}P nucleus. **a-c**, Observation of nuclear resonances at $B_0 = 1.77 \text{ T}$, while the electron spin is $|\downarrow\downarrow\rangle$ (a), $|\uparrow\uparrow\rangle$ (b), or absent, i.e. ionized donor (c). The resonance condition is obtained when $|\Delta f_\uparrow|$ drops from the unperturbed value ~ 0.4 to near zero, due to the randomization of the nuclear spin state. In each panel, the top inset shows the plunger gate voltage waveform (gray line) plus NMR/ESR pulse sequence, whilst the bottom-right inset shows the energy levels involved in the NMR transition. **d**, Dependence of the NMR resonances on the magnetic field B_0 . Solid lines are the values predicted using the ^{31}P nuclear gyromagnetic ratio $\gamma_n = 17.23 \text{ MHz/T}$.

spin $|\uparrow\rangle$, as required to observe the ν_{n2} resonance (Fig. 5.7b).

Since we have full control over the charge state of the donor, we can also perform an NMR experiment while the donor is ionized (Fig. 5.7c), as recently demonstrated in a bulk Si:P sample [166]. In this case there is only one resonance frequency, $\nu_{n0} = \gamma_n B_0$. The electron is placed back onto the donor after the NMR burst, for the purpose of reading out the nuclear spin state. Fig. 5.7d shows the magnetic field dependence of the three NMR frequencies, which agree with the expected values assuming the bulk ^{31}P gyromagnetic ratio $\gamma_n = 17.23$ MHz/T (Ref. 89). This observation confirms that the system under study is indeed a single ^{31}P phosphorus atom. Furthermore, from these measurements we find that $g = 1.9987(6)$ (see next section), within $\sim 0.01\%$ of the bulk value for Si:P, whereas the hyperfine splitting $A = 114.30(1)$ MHz is close to, but not identical with, the bulk value of 117.52 MHz (Ref. [76]). We interpret this as evidence of a Stark shift of the hyperfine coupling [167], caused by a distortion of the electron wavefunction under the strong electric fields present in the gated nanostructure. This observation is important because the Stark shift of A was proposed by Kane [68] as a mechanism to address individual ^{31}P nuclear spin qubits while applying a global microwave field.

5.7 Calculation of the Electron g -Factor

With the eigenstate energies of the neutral donor system, presented in frequency units in Section 1.4 (Eq. 1.4), we can express the *exact* nuclear spin resonance

frequencies as:

$$\nu_{n1} = E_{\downarrow\downarrow} - E_{\downarrow\uparrow} = \frac{A + \sqrt{(\gamma_+ B_0)^2 + A^2 - \gamma_- B_0}}{2}$$

$$\nu_{n2} = E_{\uparrow\uparrow} - E_{\uparrow\downarrow} = \frac{A - \sqrt{(\gamma_+ B_0)^2 + A^2 + \gamma_- B_0}}{2}$$

Using measured values of the NMR frequencies (ν_{n1} and ν_{n2}), along with the known values of the ^{31}P electron and nuclear gyromagnetic ratios [89], an accurate calibration of the external field B_0 can be made,

$$B_0 = \frac{\Delta\nu_n \gamma_- + \sqrt{\Delta\nu_n^2 \gamma_+^2 - 4\gamma_e \gamma_n A^2}}{4\gamma_e \gamma_n}$$

where $\Delta\nu_n = \nu_{n1} - \nu_{n2}$ and $A = \nu_{n1} + \nu_{n2}$. With the experimentally determined ESR transition frequencies (ν_{e1} and ν_{e2}), we can then calculate the electron g -factor,

$$g = \frac{h\bar{\nu}_e}{\mu_B B_0}$$

where $\bar{\nu}_e = (\nu_{e1} + \nu_{e2})/2$ and h is Planck's constant and μ_B is the Bohr magneton. Of course, the electron gyromagnetic ratio $\gamma_e = g\mu_B/h$, which is used in the calculation of B_0 , itself depends on the electron g -factor. We must therefore calculate B_0 and g recursively. After extracting the g -factor from each data point in Fig. 5.7d using the measured values of ν_{n1} , ν_{n2} , ν_{e1} and ν_{e2} , we find an average value of $g = 1.9987(6)$, within $\sim 0.01\%$ of the bulk value of 1.9985 [76].

5. ^{31}P Nuclear Spin Qubit

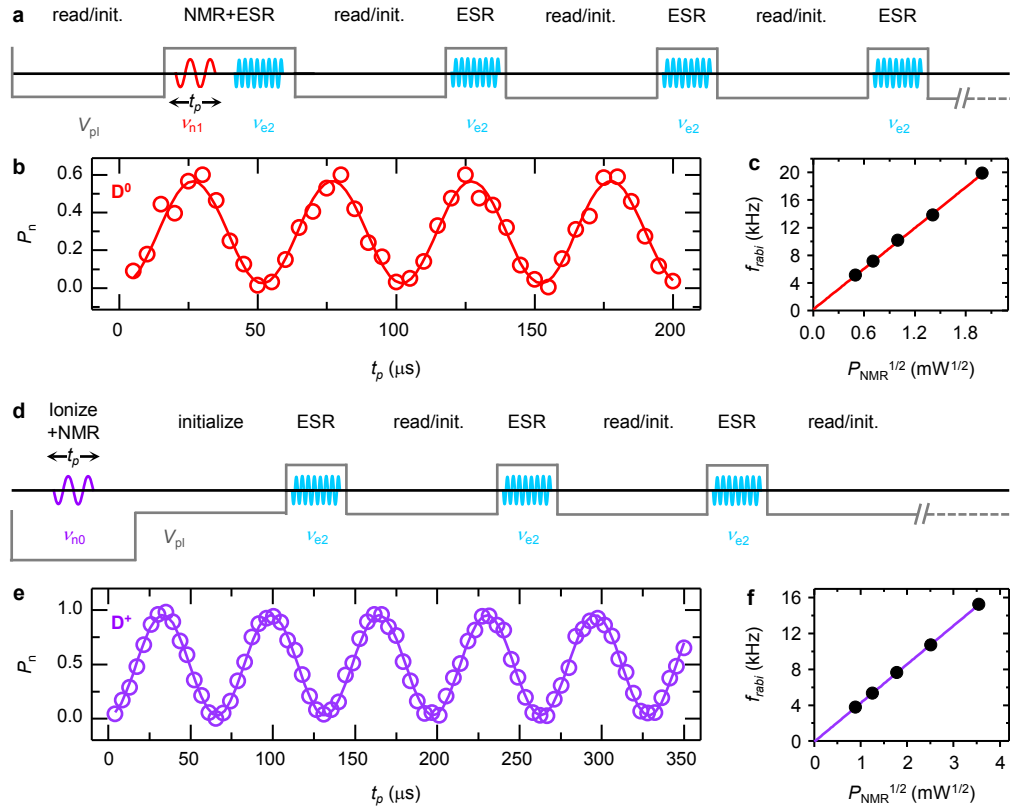


Figure 5.8: Rabi oscillations of a single ^{31}P nuclear spin. **a**, Pulse sequence for the coherent rotation of a ^{31}P nuclear spin with the donor in the neutral D^0 state. Depicted is the plunger gate voltage waveform (gray line) and combined NMR/ESR pulses. After a coherent NMR pulse at $\nu_{\text{n}1}$ of duration t_p , the state of the nuclear spin is read by probing the $\nu_{\text{e}2}$ ESR transition with 300 single-shot adiabatic inversion and electron spin readout measurements, lasting approximately 300 ms. We note that we could have equally chosen to perform the readout at the $\nu_{\text{e}1}$ transition. The resulting electron spin-up fraction $f_{\uparrow}(\nu_{\text{e}2})$ is compared to a threshold, extracted from the quantum jumps experiment (Fig. 5.2a), and a nuclear spin orientation is ascribed to the measurement. **b**, Rabi oscillation of the neutral ^{31}P donor nuclear spin with $P_{\text{NMR}} = 6 \text{ dBm}$, $B_0 = 1.07 \text{ T}$ and $\nu_{\text{n}1} = 75.7261 \text{ MHz}$. The pulse sequence of **a** is repeated 40 times for each Rabi pulse length t_p , with 5 sweeps of t_p performed to give a total of 200 measurements at each t_p . The number of nuclear spin flips is recorded to give the flip probability P_n . The solid line is a fit of the form $P_n = K \sin^2(\pi f_{\text{rabi}} t_p)$, where K and f_{rabi} are free fitting parameters. **c**, Rabi frequency f_{rabi} , extracted from fits of data similar to that in panel **b**, against the square-root of the RF power $P_{\text{NMR}}^{1/2}$. **d**, Modified pulse sequence to perform Rabi oscillations on the ^{31}P nuclear spin with the donor in the ionized D^+ state. The electron is first removed before a coherent NMR burst is applied. The electron is then replaced so that a single-shot measurement can be performed on the nuclear spin. **e**, Sample Rabi oscillation of the ionized donor nuclear spin using $P_{\text{NMR}} = 21 \text{ dBm}$, $B_0 = 1.77 \text{ T}$ and $\nu_{\text{n}0} = 30.5485 \text{ MHz}$, with each data point again comprising 200 nuclear spin state measurements. **f**, Plot showing the linear scaling of the ionized nuclear spin Rabi frequency with the excitation amplitude.

5.8 Coherent Control: Rabi Oscillations

By applying the NMR excitation for a much shorter duration, we are able to produce coherent superpositions of the nuclear spin states [60]. In the Bloch sphere representation, where the states $|\uparrow\rangle$ and $|\downarrow\rangle$ reside at the poles, the short RF excitation produces a controlled rotation about the X or Y axis. These rotations can be observed by varying the length of the RF burst, which produces the Rabi oscillations of Fig. 5.8.

For the neutral (D^0) donor, we first initialize the electron in the $|\downarrow\rangle$ state. A pulse of length t_p and at the ν_{n1} resonance – as determined from the NMR spectroscopy above – is applied immediately after, followed by a single-shot readout of the nuclear spin state (see Fig. 5.8a). A total of 200 measurements are performed at each t_p , and the induced nuclear spin flip probability P_n is found. The result is the coherent Rabi oscillations of Fig. 5.8b, whose frequency f_{rabi} scales linearly with RF excitation amplitude $P_{\text{NMR}}^{1/2}$ (Fig. 5.8c). The visibility of the oscillations in Fig. 5.8b is $\sim 60\%$. Deviations from ideality are most likely due to erroneous initialization in the $|\uparrow\rangle$ state (Section 4.6.1) caused by heating resulting from the train of microwave pulses used during readout. The maximum Rabi frequency attained in our experiments was ~ 20 kHz. Stray electric fields generated by the transmission line interfered with the SET and prevented the application of greater RF powers.

We modified the pulse sequence to remove the electron before applying the RF excitation at the ν_{n0} transition (Fig. 5.8d). This enabled the demonstration of Rabi oscillations on the ionized (D^+) ^{31}P nuclear spin (Figs. 5.8e,f). The Rabi oscillations now have near-unity visibility, because the electron spin state has no bearing on the nuclear resonance frequency while the donor is ionized.

5.9 Nuclear Spin Qubit Coherence: Ramsey Fringes and Hahn Echo

To assess the viability of utilizing the ^{31}P nuclear spin as a quantum bit, it is critical to characterize the duration over which coherence is preserved. The time it takes a coherent superposition of nuclear spin states to evolve into an incoherent mixture, averaged over many experimental runs, is termed T_2^* . This important figure of merit can be found by carrying out a Ramsey fringe measurement, the NMR pulse sequence for which is shown in Fig. 5.9a. An initial $\pi/2$ pulse puts the nuclear spin in an equal superposition of $|\uparrow\rangle$ and $|\downarrow\rangle$, or equivalently, in the XY-plane on the Bloch sphere. We let it evolve for a time τ before executing another $\pi/2$ pulse and performing a measurement on the nuclear spin (see Fig. 5.9b for a Bloch sphere state evolution). We repeat the sequence 200 times and then step τ , with the acquisition of each τ occurring over ~ 3 minutes. The spin is intentionally detuned from resonance so that during the period of free evolution, the spin accumulates a phase with respect to the rotating reference frame defined by the clock of the microwave source. Consequently, interference fringes are observed in the recovered nuclear spin flip probability as a function of τ (Fig. 5.9c). The decay of the fringes in Fig. 5.9c is the result of fluctuations in the local magnetic environment, which cause slight variations in the value of the detuning between runs (see Section 4.4). Fitting the data with a damped cosine function $P_n(\tau) = P_n(0) \cos(2\pi\Delta d\tau) \exp(-\tau/T_2^*)$, where $P_n(0)$ is the amplitude and Δd the average detuning from resonance, reveals a $T_2^*(\text{D}^0) = 0.84(10)$ ms for the neutral donor and a $T_2^*(\text{D}^+) = 3.3(3)$ ms for the ionized donor. These figures are $\sim 10^4$ times longer than those measured for the electron spin [55, 87].

5.9. Nuclear Spin Qubit Coherence: Ramsey Fringes and Hahn Echo

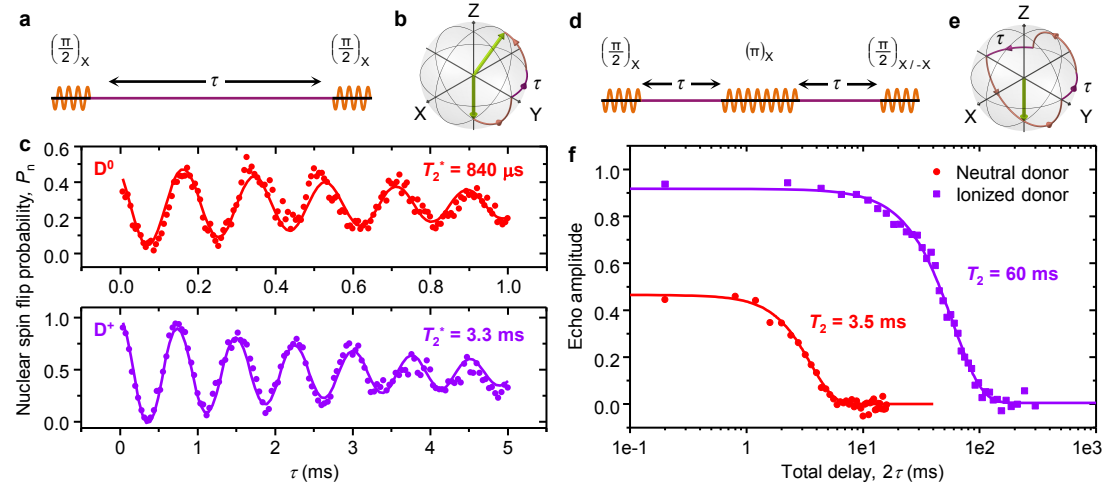


Figure 5.9: Ramsey fringes and spin echo decay. **a**, NMR pulse sequence for the Ramsey fringe experiment. This sequence replaces the single pulse of duration t_p in Fig. 5.8a (Fig. 5.8d) for the neutral (ionized) donor, whereas the nuclear spin is read out in the same way. The phase of both $\pi/2$ pulses is such that rotation is performed about the X axis on the Bloch sphere, as noted in the rotation angle subscript above each pulse. **b**, Bloch sphere representation of the evolution in the rotating frame for the Ramsey fringe measurement. The green arrow represents the nuclear spin. The purple path represents dephasing in between pulses, whilst the orange path represents a rotation about X. **c**, Ramsey interference fringes for the nuclear spin with the donor in the D^0 (top) and D^+ (bottom) charge states, taken at $B_0 = 1.77$ T. Here a $\pi/2$ pulse was $12.5\mu\text{s}$ for the D^0 experiment and $23.5\mu\text{s}$ for the D^+ . We sweep the inter-pulse delay, and repeat the sequence 20 times at each τ . A total of 10 sweeps are performed (200 measurements) and the nuclear spin flip probability P_n is found. Fits to the data are discussed in the main text. **d**, Pulse sequence for the Hahn echo experiment. The full measurement protocol is provided by inserting this sequence in place of the single NMR pulse in Fig. 5.8a (Fig. 5.8d) for the neutral (ionized) donor. Here we also implement phase cycling (Section 4.5.1), where the final $\pi/2$ rotation is first performed about the X axis and then the measurement is repeated with the final $\pi/2$ about the $-X$ axis. Subtracting the two signals ensures a baseline of zero. **e**, Bloch sphere representation for the Hahn echo measurement. Here the final $\pi/2$ pulse is about X ($-X$ is not shown). **f**, Decay of the echo amplitude as the delay τ is increased for the case of a neutral (circles) and ionized (squares) donor. We perform 40 repetitions of the sequence for each τ and 25 sweeps, totalling 1000 measurements at each point. The phase-cycled echo amplitude is given by $[P_n(\nu_n, -X) - P_n(\nu_n, X)]/40$, where $P_n(\nu_n, -X/X)$ represents the nuclear spin flip probability measured at the NMR resonance ν_n with a final $\pi/2$ pulse about the $-X$ or X axis. All other experimental conditions are as in the Ramsey fringe experiment. Fits through the data are discussed in the text.

Many of the magnetic fluctuations that contribute to T_2^* occur on timescales much greater than the typical nuclear spin manipulation time ($\sim 25\mu\text{s}$ for a π pulse). Therefore, a significant portion of the dephasing can be reversed by performing a π rotation in the middle of the free evolution period of Fig. 5.9a. This modified sequence (Fig. 5.9d) is known as a Hahn echo (refer to Fig. 5.9e for a Bloch sphere representation). Observing the echo signal as the delay τ is varied yields the decay curves displayed in Fig. 5.9f. We fit the data with functions of the form $y = y(0) \exp((-2\tau/T_2)^b)$, where $y(0)$ is the amplitude, b is a free exponent and T_2 is the coherence time. For the neutral donor spin, we find $T_2(\text{D}^0) = 3.5(1)$ ms and $b(\text{D}^0) = 2.2(2)$, and for the ionized donor spin we extract $T_2(\text{D}^+) = 60.0(9)$ ms and $b(\text{D}^+) = 1.77(7)$.

The observation that the ratio T_2/T_2^* is not the same for the D^0 and D^+ charge states of the donor nuclear spin (~ 4 for the former and ~ 18 for the latter) suggests that the power spectral density of the decohering noise may have a different form (not just strength) for the two cases [168]. For the ionized donor spin, both the coherence time ($T_2(\text{D}^+) = 60$ ms) and the shape of the echo decay ($b(\text{D}^+) = 1.77$) are fully accounted for by the spectral diffusion caused by dynamics of the ^{29}Si nuclear spin bath, as quantified by recent theory [169]. Accordingly, we expect that removal of ^{29}Si through isotopic purification [149, 157] should yield T_2 values of order minutes, as observed in bulk-doped samples [158].

For the neutral donor spin, one would expect the mechanism of ^{29}Si spectral diffusion to be weaker than in the ionized case, as the hyperfine field gradient provided by the electron should, to some extent, suppress the ^{29}Si dipole flip-flops [141]. The observation that the nuclear spin coherence is worse for the neutral donor suggests that an additional decoherence process occurs there. One

possibility is that charge noise at the Si/SiO₂ interface [166] or electronic gate noise [68] causes a time-dependent Stark shift of the hyperfine coupling, which results in a random modulation of the instantaneous nuclear Larmor frequency. Future work will focus on the identification and mitigation of these additional processes.

5.10 Qubit Readout and Control Fidelities

5.10.1 Nuclear Spin Readout Fidelity

We now turn to an analysis of the fidelity of our solid-state qubit. The single-shot nuclear spin readout can be performed with a very high fidelity, owing to the quantum non-demolition (QND) nature of the measurement. In general, a QND measurement is obtained if the Hamiltonian \mathcal{H}_{int} , describing the interaction between observable and measurement apparatus, commutes with the observable [170]. In our case, the “observable” is the z projection of the nuclear spin state I_z , while the “measurement apparatus” is the electron spin. The QND condition, $[I_z, \mathcal{H}_{\text{int}}] = 0$, would require a hyperfine coupling of the form AS_zI_z . The physical phenomena responsible for the observed nuclear spin quantum jumps originate from the measurement through the electron spin, and can be viewed as a deviation from QND ideality. The isotropic hyperfine coupling contains the terms $A_{\parallel}(S_xI_x + S_yI_y)$, which do not commute with I_z . In addition any anisotropic part of the hyperfine tensor $\underline{\underline{A}}$ (e.g., $A_{\perp}S_zI_x$) also does not commute with I_z . For the nuclear $|\uparrow\uparrow\rangle$ state, this results in a lifetime $T_{\uparrow\uparrow} = 1495(360)$ s (obtained from extended data of the measurement in Fig. 5.2a). For the nuclear $|\downarrow\downarrow\rangle$ state, the cross-relaxation process – caused by phonons modulating the hyperfine cou-

pling – also introduces a term that does not commute with I_z , yielding a lifetime $T_{\Downarrow} = 65(15)$ s (Fig. 5.2a).

These lifetimes must be contrasted with the nuclear spin measurement time T_{meas} , which has been optimized here to maximize the nuclear spin readout fidelity. T_{meas} is given by the number of single-shot electron spin readout events acquired per measurement. The larger the number of electron spin single-shots taken, the lower the SNR-limited readout error will be. However, a trade-off exists in that the longer measurement duration results in a greater chance of a nuclear spin quantum jump occurring during readout. In Figs. 5.2a-e, 250 shots resulted in a 260 ms measurement duration and a SNR-limited readout error of 2×10^{-7} . By decreasing the number of shots to 100, we were able to perform the measurement in less than half of the time ($T_{\text{meas}} = 104$ ms) with an increased, but still relatively low SNR-limited error of 2×10^{-5} . We find that 100 shots provides a near optimal tradeoff between nuclear spin quantum jump occurrence and the SNR-limited readout error.

Combining the optimal measurement time ($T_{\text{meas}} = 104$ ms) with the observed nuclear spin lifetimes yields the QND fidelities: $F_{\text{QND}}(|\uparrow\rangle) = \exp(T_{\text{meas}}/T_{\uparrow}) = 0.99993(2)$; and $F_{\text{QND}}(|\Downarrow\rangle) = \exp(T_{\text{meas}}/T_{\Downarrow}) = 0.9984(4)$. We have therefore obtained readout fidelities between 99.8% and 99.99%, the highest for any solid-state qubit, and comparable with the fidelities observed for qubits in vacuum-based ion-trap systems [151].

5.10.2 Nuclear Spin Control Fidelity

The nuclear spin control fidelity F_C will ultimately be limited by T_2 and the minimum gate operation time achievable. We quantify F_C by directly measuring the

5.10. Qubit Readout and Control Fidelities

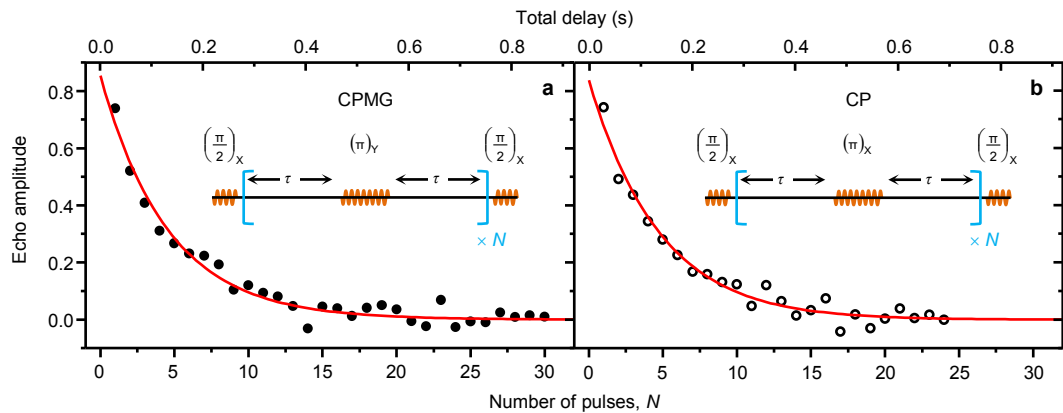


Figure 5.10: Coherence measurements for extracting the rotation angle error. **a**, A Carr-Purcell-Meiboom-Gill (CPMG) experiment where we plot the echo amplitude as a function of the number of π pulses applied N , with a fixed delay τ . We calculate the signal amplitude using the phase cycling formula given in Section 4.5.1). The CPMG sequence is shown as an inset. The fit to the data is a simple exponential decay of the form $y = \exp(-2N\tau/T_{2,CPMG})$ **b**, Echo decay from a Carr-Purcell (CP) sequence (see inset), which differs from the CPMG sequence in the axis about which the π rotations are performed. The fit through the data is discussed in the text. Both the CPMG and CP measurements were obtained over 36 sweeps of N , where in a single sweep we perform 40 repetitions of the pulse sequence for each N . The echo decay amplitudes were ~ 0.85 for both the CPMG and CP experiments, we attribute this reduction to a miscalibration of the $\pi/2$ pulses (which were simply assumed to be half the duration of a π rotation), systematic phase errors producing rotations that were not completely orthogonal and the occurrence of nuclear spin quantum jumps during the measurements.

rotation angle error for the ionized donor nuclear spin using the method outlined in [171]. We employ two different dynamical decoupling sequences to measure the coherence time T_2 ; the Carr-Purcell (CP) sequence and the Carr-Purcell-Meiboom-Gill (CPMG) sequence. The CP protocol is a simple modification on the Hahn echo (Fig. 5.9d), where the single refocusing π pulse is replaced with a series of π rotations separated from one another by a delay 2τ (see inset of Fig. 5.10b). In the CP sequence, all pulses (including the initial and final $\pi/2$ rotations) are about the same axis on the Bloch sphere, and their associated errors are additive. The CPMG sequence remedies the problem of pulse error accumulation by performing the π rotations about an orthogonal axis (inset of Fig. 5.10a), in our case the Y axis.

In order to find the error involved in a single π pulse, we monitor the decay of the CPMG echo signal (Fig. 5.10a) as we increase N , the number of π pulses in the sequence. Here τ is fixed at 14.4 ms, and an exponential fit to the data provides a coherence time of $T_{2,CPMG} = 131(7)$ ms. We repeat the measurement with the CP sequence and observe the decay of Fig. 5.10b. Because the CP sequence accumulates pulse errors, the decay should be attenuated by an additional factor given by $\exp(-\sigma^2 N^2/4)$ [171], where σ is the standard deviation of the error (in radians) for a single π rotation. Here it is assumed that the mean flip angle error is negligible, and we have gone to great lengths to ensure that rotation errors due to systematic off-resonance or pulse timing effects were kept to a minimum. We periodically performed Ramsey fringe measurements to ensure that we were tuned within 100 Hz of the resonance frequency, and Rabi oscillations were regularly taken to calibrate the π pulse duration.

For measurements on bulk-doped samples, σ originates from the inhomogene-

5.11. Conclusion

ity of the RF or microwave field over the sample volume. Because we measure only a single donor, σ here would more likely result from slow fluctuations of the instantaneous ^{31}P NMR frequency due to dynamics of the ^{29}Si spin bath. Fitting the CP data with a function of the form $y = \exp(-2N\tau/T_{2,\text{CPMG}}) \exp(-\sigma^2 N^2/4)$, where $T_{2,\text{CPMG}}$ is the coherence time as extracted from the CPMG measurement, we find by considering the best-case $T_{2,\text{CPMG}}$ of 138 ms a σ of 0.05 radians ($\sim 3^\circ$). Note that by using the standard error in the fitting parameter $T_{2,\text{CPMG}}$ to extract σ , we obtain an uncertainty and can only conclude that the control fidelity $F_C = 1 - \sigma/180^\circ$ is greater than 98%. A more accurate specification of F_C would require the acquisition of many more data sets, which was impractical considering the timescale over which the measurements of Fig. 5.10 were obtained (~ 70 hours).

5.11 Conclusion

The results presented here demonstrate that the nuclear spin of a single ^{31}P donor could constitute a quantum memory in an electron-spin-based quantum computer [87], or a high-fidelity qubit in a quantum processor where the nuclear spin is the primary computational element [68]. Future experiments will therefore focus on demonstrating electron-nuclear entanglement [93, 172] and the coupling of multiple nuclei mediated by hyperfine and exchange interactions [68]. We anticipate that exploiting the ^{31}P nuclear spin qubit will open new avenues for large-scale quantum-computer architectures, where the quantum coherence of well-isolated atomic systems is combined with the manufacturability of silicon nanoelectronic devices.

Chapter 6

^{29}Si Nuclear Spin Qubit

Magnetic fluctuations caused by the nuclear spins of a host crystal is often the leading source of decoherence for many types of solid-state spin qubit. In silicon, the spin-bearing nuclei are sufficiently rare that it is possible to isolate and control individual host nuclear spins. This chapter presents the first experimental detection and manipulation of a single ^{29}Si nuclear spin. The QND single-shot readout is achieved using techniques introduced in Chapter 5, and Hahn echo measurements reveal a coherence time of $T_2 = 6.3(7)$ ms – in excellent agreement with bulk experiments. Atomistic modeling combined with extracted experimental parameters provides possible lattice sites for the ^{29}Si atom under investigation. These results demonstrate that single ^{29}Si nuclear spins could serve as a valuable resource for a ^{31}P donor spin-based quantum computer.

The author acknowledges F. A. Mohiyaddin for work on the atomistic modeling of possible ^{29}Si lattice sites.

This chapter is currently in preparation for peer-reviewed publication.

6.1 Introduction

The presence of non-zero nuclear spins in a host crystal lattice is known to induce decoherence in a central spin qubit through spectral diffusion [72, 137]. This was the suspected primary source of magnetic noise for the ^{31}P electron and nuclear spin qubits presented in Chapters 4 and 5. For electron spins confined in semiconductors, it has been proposed that the nuclear spin bath could potentially be used as a resource for quantum computing. The state of an electron spin qubit could be mapped onto the collective state of the nuclei, raising the prospect of a long-lived quantum memory [173]. In addition, the generation of squeezed and entangled nuclear spin states [174] may permit precise control of the bath dynamics. A recent experiment in diamond [175] demonstrated the ability to suppress dephasing of a single NV spin through coherent control of the surrounding electron spin bath. In GaAs quantum dots [176] polarization of the bath has also enabled control over the nuclear spins, and a coherence time has been measured which exceeds that of the electron spin.

For semiconductors composed of majority spin-zero isotopes (such as silicon and diamond), the rarity of spin bearing nuclei means that it is possible to resolve individual hyperfine couplings with a central electronic spin, permitting the detection and manipulation of single nuclear spins. This has lead to the demonstration of a quantum register for the spin of a NV-center in diamond, where the electronic spin state can be stored in individual nuclei [177] and read out with high fidelity [61]. Similar demonstrations should be possible in silicon, where the ^{29}Si nuclear spin acts as an additional resource for QIP.

In addition to potentially serving as a quantum register for the ^{31}P donor electron spin, the ^{29}Si nuclear spin has itself been advanced as a quantum bit

in an “all-silicon” quantum computer [178, 179]. In this scheme, interactions between ^{29}Si qubits are facilitated by their dipolar coupling. Qubit initialization and readout can be achieved by using single ^{31}P impurities, through exploiting the hyperfine interaction between the ^{29}Si nuclear and donor electron spins. As a result of the potential for the ^{29}Si nuclei to act as valuable resources in donor-based silicon quantum computers, or as qubits in an all-silicon quantum computer, the detection and manipulation of single ^{29}Si nuclear spins is a desirable goal. This chapter presents a series of measurements that demonstrate such abilities, including the QND readout, the coherent control, and the measurement of the coherence times of an individual ^{29}Si nuclear spin.

6.2 Power Dependence of the Electron Spin Resonance Signal

In the previous two chapters of this thesis, techniques were described for measuring and manipulating the electron and nuclear spins of a single ^{31}P donor. High-fidelity ^{31}P nuclear spin detection was possible owing to the QND nature of the measurement, which allowed repeated nuclear spin single-shot readout (Section 5.3). Here we demonstrate that this same sensitive technique can be applied to detect the spin of a single ^{29}Si nucleus, which lies within the extent of the donor electron wavefunction.

We have performed an ESR experiment (see Section 4.2) about a single ^{31}P hyperfine peak. We chose the transition corresponding to the $|\uparrow\rangle$ state, i.e. ν_{e2} , since the nuclear spin is predominantly polarized here as a result of the differing $|\uparrow\rangle$ and $|\downarrow\rangle$ nuclear spin relaxation mechanisms (see Section 5.3). The ESR ex-

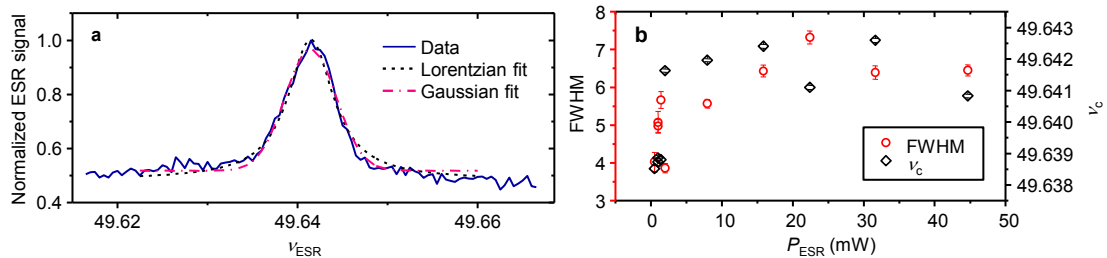


Figure 6.1: ESR peak at the ν_{e2} transition and its corresponding power dependence. **a**, ESR scan at the electron spin transition corresponding to the nuclear $|\uparrow\rangle$ state, performed at $B_0 = 1.77$ T. Data at each frequency represent the average of 75,000 single-shot measurements of the electron spin. Both Gaussian and Lorentzian fits are given. Whilst the Gaussian provides a better overall fit, the resonance displays Lorentzian-like features (such as a long tail). **b**, The resonance FWHM and center frequency ν_c , as a function of the microwave power P_{ESR} . Parameters are extracted from Gaussian fits.

periment involves monitoring the induced electron spin-up fraction f_{\uparrow} in response to a microwave excitation with varying frequency ν_{ESR} – a similar experiment was depicted in Fig. 4.8b. Taking 250 single-shot readouts of the electron spin at each frequency to calculate $f_{\uparrow}(\nu_{\text{ESR}})$ (in ~ 250 ms), and averaging over 300 sweeps of ν_{ESR} , yields the spectrum of Fig. 6.1a. The line-shape is neither Gaussian nor Lorentzian, but contains features of both. The peak has a FWHM of ~ 7 MHz (or 250 μT) at the largest applied ESR power P_{ESR} – which corresponds to the bulk value for the inhomogeneous broadening caused by the nuclear spin bath. As the power is reduced, the line is observed to narrow and shift to a lower frequency (Fig. 6.1b). This is inconsistent with power broadening [180], where the linewidth is $\propto \sqrt{P_{\text{ESR}}}$ but the center frequency should remain unchanged. Furthermore, the measured Rabi frequency (at $B_0 = 1.07$ T) from Section 4.3 implies an upper bound here of $B_1 \leq 0.12$ mT, a value lower than the anticipated inhomogeneous broadening. The inhomogeneous broadening in a bulk-doped sample arises because of the different ^{29}Si configuration at the site of each ^{31}P donor. In our single donor experiment, this inhomogeneous broadening is caused by dif-

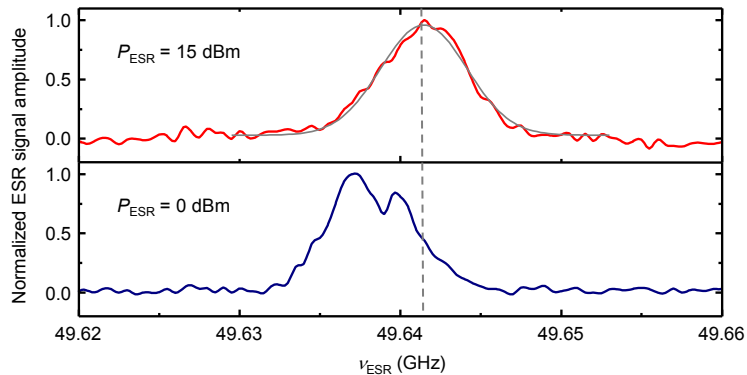


Figure 6.2: ESR peak splitting at low microwave excitation powers. ESR experiments at $\nu_{\text{e}2}$, with the top panel taken using a microwave power $P_{\text{ESR}} = 15$ dBm and the bottom panel using $P_{\text{ESR}} = 0$ dBm. The data in the top panel is fit with a Gaussian (gray line). The low-power peak displays a splitting of ~ 2.2 MHz, which we attribute to a single hyperfine coupled ^{29}Si nuclear spin.

ferent states of the same ^{29}Si bath configuration, which can change throughout the measurement process (Section 4.4). The P_{ESR} dependence of the peak position and width might be explained by a spin-bath narrowing effect, where the measurement process decreases the entropy of the spin bath [181].

6.3 Single-Shot Readout of a ^{29}Si Nuclear Spin

A careful analysis of the low-power resonance peaks reveals that they exhibit a splitting (Fig. 6.2), which is reproducible over several measurements. The low-power shift in center frequency ν_c is also clearly displayed in Fig. 6.2. As we will further substantiate below, the splitting indicates the presence of a strongly hyperfine-coupled ^{29}Si nuclear spin. In the presence of a hyperfine-split ESR peak, we can read the state of the spin by performing a quantum jumps measurement, as described in Section 5.3 for the case of the ^{31}P nucleus. Here we execute 100 adiabatic passages over the first half of the $\nu_{\text{e}2}$ resonance, acquiring single-

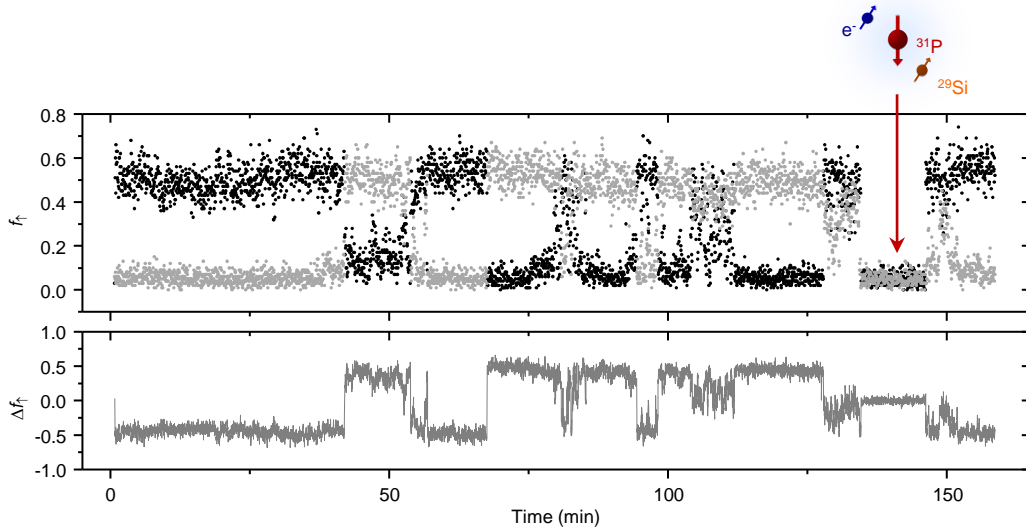


Figure 6.3: Quantum jumps of a single ^{29}Si nuclear spin. Single-shot QND readout of a ^{29}Si nuclear spin at $B_0 = 1.77$ T, with a power $P_{\text{ESR}} = 0$ dBm. Quantum jumps of the nuclear spin can be seen to occur on minute-long timescales, with no clear preference for the orientation. The bottom panel represents the difference in the spin-up fraction Δf_{\uparrow} from measurements on the left and right sides of the split ν_{e2} resonance (shown individually in the top panel). The red arrow marks the off-resonance data, where the ^{31}P nuclear spin has flipped to the state $|\Downarrow\rangle$. Periodic initialization of the donor nuclear spin in the $|\Uparrow\rangle$ state is performed in order to limit the off-resonance duration.

shot measurements of the electron spin to obtain f_{\uparrow} , and then repeating the process on the second half of the hyperfine-split ν_{e2} peak. We observe clear “quantum jumps” (Fig. 6.3), providing strong evidence that the splitting does indeed originate from a single spin coupled to the electron. The jumps occur over minutes-long timescales, representing of order $\sim 100,000$ single-shots. This observation implies that the ^{29}Si nuclear spin detected here must have an almost perfectly isotropic hyperfine coupling to the electron spin (Section 5.5).

Because the ESR line splitting is not fully resolved (Fig. 6.2), we don’t find the well separated bands of the ^{31}P nuclear spin readout (Fig. 5.2) in Section 5.3. Occasionally, measurement on both sides of the split peak produces an off-resonance result, indicating that the ^{31}P nuclear spin has flipped to the $|\Downarrow\rangle$ state. We there-

fore periodically measure the state of the donor nuclear spin and initialize it $|\uparrow\rangle$ if it has flipped (further details are provided in Section 6.4).

6.4 ²⁹Si Spin Control: Nuclear Magnetic Resonance and Coherence Measurements

To verify that the spin belongs to a ²⁹Si nucleus, we perform a NMR experiment to extract the gyromagnetic ratio. The expected transition frequencies for the ²⁹Si nuclear spin can be estimated by considering the spin Hamiltonian [76, 182]:

$$\mathcal{H} = \gamma_e B_0 S_z - \gamma_P B_0 {}^P I_z + A_P S \cdot {}^P I + \gamma_{\text{Si}} B_0 {}^{\text{Si}} I_z + A_{\text{Si}} S \cdot {}^{\text{Si}} I + \frac{\mu_0}{4\pi} \gamma_e \gamma_{\text{Si}} \hbar \left(\frac{{}^{\text{Si}} I \cdot S}{r^3} - \frac{3[{}^{\text{Si}} I \cdot r][S \cdot r]}{r^5} \right) \quad (6.1)$$

where S ($= 1/2$) and ${}^P I$ ($= 1/2$) are the electron and nuclear spins of the ³¹P donor respectively, with previously defined gyromagnetic ratios γ_e and γ_P . ${}^{\text{Si}} I$ ($= 1/2$) is the nuclear spin of a single ²⁹Si atom with gyromagnetic ratio $\gamma_{\text{Si}} = 8.46 \text{ MHz/T}$ [183]. r is a vector connecting the electron and ²⁹Si spins and μ_0 is the permeability of free space. The first, second and third terms of Eq. 6.1 are the familiar ³¹P electron and nuclear Zeeman and hyperfine interactions. The fourth and fifth terms describe the ²⁹Si nuclear spin, i.e. its Zeeman interaction with the external magnetic field B_0 and its contact hyperfine interaction with the electron spin respectively. The final term gives the dipolar interaction between the ²⁹Si nuclear spin and the electron spin. The energies of the eigenstates of this three-spin coupled system can be simplified with a few assumptions. We assume that any non-secular or anisotropic terms in the hyperfine interactions between

the ^{31}P donor nuclear spin and electron spin and between the electron spin and the ^{29}Si nuclear spin are negligible. The same assumption is made for the dipolar interaction between the electron spin and the ^{29}Si nuclear spin. Finally, we assume the high magnetic field limit, where $\gamma_e B_0 \gg A_P, A_{\text{Si}}$ (+ secular dipolar terms). These assumptions are reasonable given the extremely low flipping probability observed for both nuclear spins under measurement of the electron spin. The presence of strong non-secular or anisotropic terms would result in a much shorter nuclear spin flipping time (see Section 5.5). The energies of the three-spin states can then be expressed as [76]:

$$E(m_e, m_P, m_{\text{Si}}) = \gamma_e B_0 m_e + A_P m_e m_P - \gamma_P B_0 m_P + \gamma_{\text{Si}} B_0 m_{\text{Si}} + A_{\text{Si}} m_e m_{\text{Si}} + D_{\text{Si}} m_e m_{\text{Si}} \quad (6.2)$$

with the dipole constant:

$$D_{\text{Si}} = \frac{\mu_0 \gamma_e \gamma_{\text{Si}} \hbar (1 - 3 \cos^2 \theta)}{4\pi r^3} \quad (6.3)$$

where θ is the angle between r and B_0 . Here m_{\diamond} is the quantum number for spin \diamond ($= \text{e, P or Si}$), which is $+1/2$ for spin-up and $-1/2$ for spin-down. Our experiments are performed with the ^{31}P nuclear spin in the $|\uparrow\uparrow\rangle$ state, therefore $m_P = 1/2$. We define $\nu_{\text{Si}1}$ as the the NMR transition frequency for driving the ^{29}Si nuclear spin whilst the electron spin is in the sate $|\downarrow\rangle$ and $\nu_{\text{Si}2}$ the transition when the electron spin is $|\uparrow\rangle$ (Fig. 6.4a). Using Eq. 6.2, we find:

$$\begin{aligned} \nu_{\text{Si}1} &= E\left(-\frac{1}{2}, \frac{1}{2}, \frac{1}{2}\right) - E\left(-\frac{1}{2}, \frac{1}{2}, -\frac{1}{2}\right) = \gamma_{\text{Si}} B_0 - (A_{\text{Si}} + D_{\text{Si}})/2 \\ \nu_{\text{Si}2} &= E\left(\frac{1}{2}, \frac{1}{2}, \frac{1}{2}\right) - E\left(\frac{1}{2}, \frac{1}{2}, -\frac{1}{2}\right) = \gamma_{\text{Si}} B_0 + (A_{\text{Si}} + D_{\text{Si}})/2 \end{aligned} \quad (6.4)$$

The ²⁹Si hyperfine splitting observed in Fig. 6.2 is ~ 2.2 MHz, at a field of $B_0 = 1.77$ T. Therefore the above formulas yield $\nu_{\text{Si}1} \approx 13.88$ MHz and $\nu_{\text{Si}2} \approx 16.08$ MHz. We then perform a NMR experiment where we first initialize the electron spin, for example $|\uparrow\rangle$, and apply a long NMR pulse at a frequency ν_{NMR} before attempting to adiabatically invert and read the electron spin. The sequence is repeated 150 times about each ²⁹Si hyperfine transition, in a manner identical to that of the ³¹P NMR experiments of Section 5.6. The electron spin-up fraction $f_{\uparrow}(\nu_{\text{e2L/R}})$ is then recorded, where ν_{e2L} and ν_{e2R} are the ²⁹Si spin-dependent ESR transition frequencies defined as:

$$\begin{aligned}\nu_{\text{e2L}} &= E\left(\frac{1}{2}, \frac{1}{2}, -\frac{1}{2}\right) - E\left(-\frac{1}{2}, \frac{1}{2}, -\frac{1}{2}\right) = \gamma_e B_0 - (A_{\text{Si}} + D_{\text{Si}})/2 \\ \nu_{\text{e2R}} &= E\left(\frac{1}{2}, \frac{1}{2}, \frac{1}{2}\right) - E\left(-\frac{1}{2}, \frac{1}{2}, \frac{1}{2}\right) = \gamma_e B_0 + (A_{\text{Si}} + D_{\text{Si}})/2\end{aligned}\quad (6.5)$$

We perform 40 sweeps of the NMR frequency, periodically detecting the state of the ³¹P nuclear spin and initializing it $|\uparrow\rangle$ if it flips (see Fig. 6.4b for the measurement sequence). The sweeps are taken over a frequency range of ~ 800 kHz, with a resolution of 5 kHz. We calculate the average absolute difference in the spin-up fraction $|\Delta f_{\uparrow}| = |f_{\uparrow}(\nu_{\text{e2R}}) - f_{\uparrow}(\nu_{\text{e2L}})|$ over all sweeps and plot the result for the $\nu_{\text{Si}2}$ transition in Fig. 6.4c. Off-resonance we find $|\Delta f_{\uparrow}| \approx 0.21$. This value is reduced from the $|\Delta f_{\uparrow}|$ reported in Fig. 6.3 due to quantum jumps of the ³¹P nuclear spin in-between initialization stages and additional heating caused by the long NMR pulse. At resonance, a randomization of the ²⁹Si spin state produces an almost equal probability of having an “active” ν_{e2L} or ν_{e2R} transition. The trough observed at $\nu_{\text{NMR}} = 16.11(2)$ MHz is remarkably close to the estimated value for $\nu_{\text{Si}2}$, providing strong evidence that this is a single ²⁹Si nuclear spin. We were unable to detect the electron $|\downarrow\rangle$ resonance at ~ 13.88 MHz, where

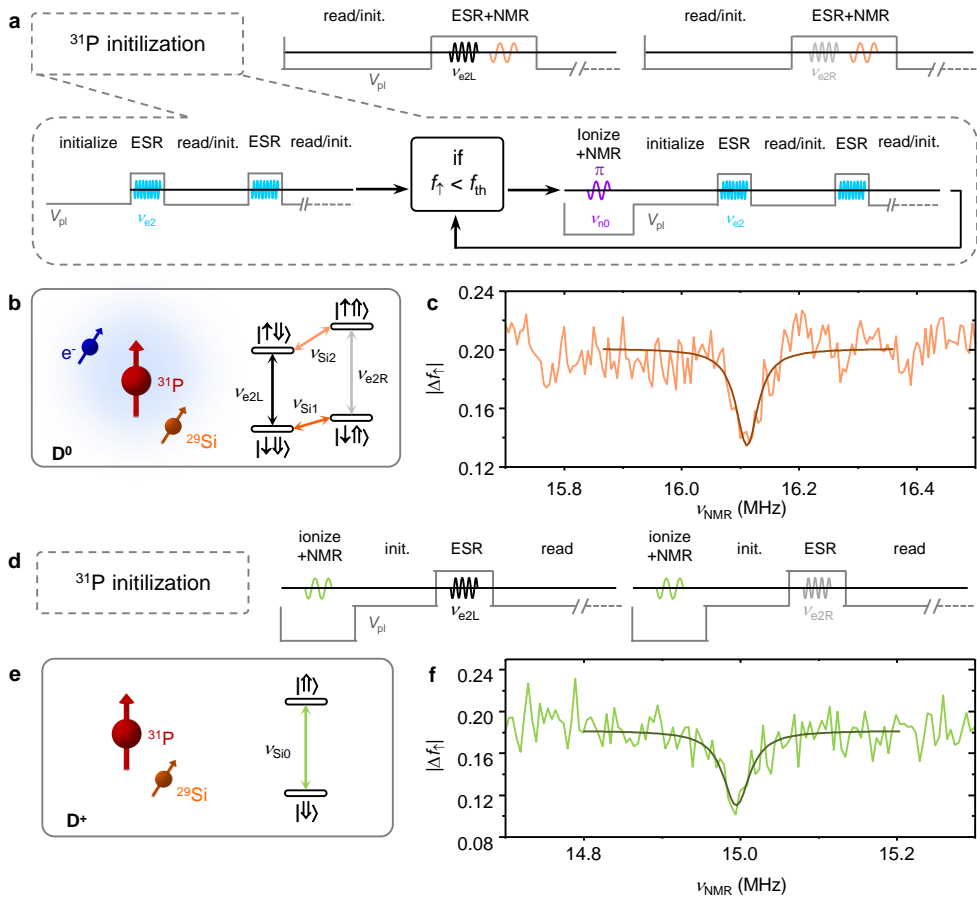


Figure 6.4: NMR experiment on a ^{29}Si nuclear spin. **a**, Pulse sequence, adapted from Section 5.6, for observing the electron $|\uparrow\rangle$ ^{29}Si NMR transition $\nu_{\text{Si}2}$. Preceding the NMR experiment is an initialization of the ^{31}P nuclear spin, the sequence for which is shown here. First, a single-shot measurement of the donor nuclear spin is performed at the ν_{e2} transition through 150 adiabatic inversions and projections of the electron spin. The resulting electron spin-up fraction f_{\uparrow} is compared to a predetermined threshold f_{th} from Section 5.3, and a ^{31}P nuclear spin state is ascribed to the measurement. If the state is $|\Downarrow\rangle$, a π pulse is given at the ionized donor ν_{n0} transition, and the ^{31}P nuclear spin measured again in a repeating process until it is flipped to the $|\uparrow\rangle$ state. **b**, Energy level diagram of the neutral $^{29}\text{Si}:\text{P}^{31}$ system, with corresponding ESR (black) and NMR (orange) transitions. The depicted states are approximately eigenstates of the system in the high magnetic field limit (see main text), and assume a fixed ^{31}P nuclear spin state $|\uparrow\rangle$ (i.e. $m_P = +1/2$). **c**, Absolute electron spin-up fraction difference $|\Delta f_{\uparrow}|$ as a function of the NMR frequency ν_{NMR} , for the ^{29}Si spin with a neutral donor and $m_e = m_P = +1/2$. The resonance is best fit with a Lorentzian (shown in dark orange), indicating possible power broadening. **d**, Pulse sequence for observing the ionized donor ^{29}Si NMR transition $\nu_{\text{Si}0}$. **e**, Energy level diagram for the ^{29}Si nuclear spin with and ionized ^{31}P donor. Here the $|\uparrow\rangle$ state is highest in energy as a result of the negative value of the ^{29}Si nuclear gyromagnetic ratio. **f**, NMR signal for the $\nu_{\text{Si}0}$ transition, with a Lorentzian fit in dark green.

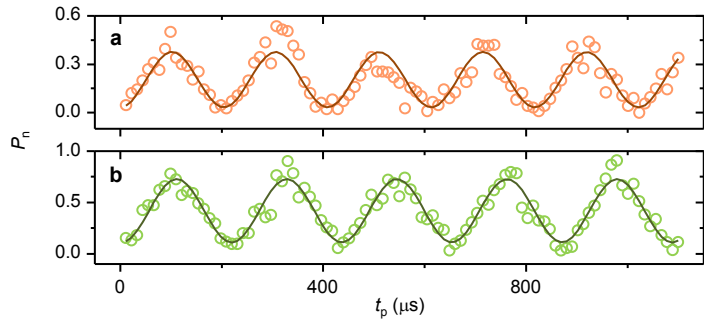


Figure 6.5: Single ^{29}Si nuclear spin Rabi oscillations. **a**, Nuclear spin flip probability P_n as a function of the pulse duration t_p , for the neutral donor $m_e = m_P = +1/2$ ^{29}Si nuclear spin. Measurement performed at $B_0 = 1.77$ T with a RF power $P_{\text{NMR}} = 18$ dBm and a microwave power $P_{\text{ESR}} = 0$ dBm. **b**, Rabi oscillations of the ionized donor ^{29}Si nuclear spin, with the same experimental parameters as in panel **a**. Fits for both curves are of the form $P_n \propto \sin^2(\pi f_{\text{Rabi}} t_p)$, where the Rabi frequency f_{rabi} is a free fitting parameter.

NMR excitations may be attenuated by the 10 MHz low-frequency cutoff of the DC-block employed in our setup (refer to Section 2.2).

An accurate estimation of γ_{Si} from the data in Fig. 6.4b is not possible owing to the uncertainty in the hyperfine splitting extracted from the ESR spectrum (Fig. 6.2). However, we can utilize methods developed in Chapter 5 for the ^{31}P nuclear spin, to ionize the donor and perform NMR on the isolated ^{29}Si nuclear spin (Fig. 6.4d). The frequency of this transition is simply given by $\nu_{\text{Si}0} = \gamma_{\text{Si}} B_0$, providing a clear measure of γ_{Si} . The pulse sequence for such a measurement is shown in Fig. 6.4e with the resulting resonance plot in Fig 6.4f. The trough at $\nu_{\text{NMR}} = 14.99(2)$ MHz, together with the external magnetic field $B_0 = 1.77$ T – calibrated using the ^{31}P NMR frequencies (Section 5.7) – implies a gyromagnetic ratio of $\gamma_{\text{Si}} = 8.47$ MHz/T. This figure is very close to the bulk value (8.56 MHz/T [183]).

We demonstrate the ability to coherently manipulate the ^{29}Si nuclear spin – with both a neutral and ionized phosphorus donor – by observing Rabi oscillations.

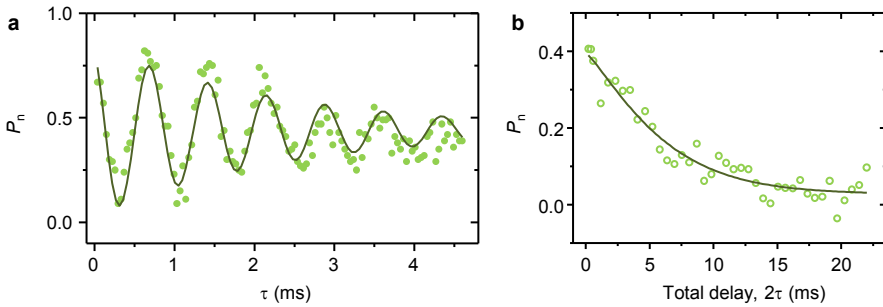


Figure 6.6: Ramsey fringes and Hahn echo decay for the ionized donor ^{29}Si nuclear spin. **a**, Ramsey fringe measurement performed at $B_0 = 1.77$ T, with a π pulse duration of $t_\pi = 110\mu\text{s}$, as calibrated from the Rabi oscillations of Fig. 6.5. **b**, Hahn echo decay measured with phase cycling (between X and $-\text{X}$) of the final $\pi/2$ pulse (see Section 4.5.1). Pulse calibration is as in panel **a**. Fits to both panels are described in the main text.

tions. The protocols for such measurements are illustrated in Figs. 6.5a and c, and are similar to the pulse sequences given for the ^{31}P nuclear spin (Figs. 5.8a,d), with the only significant difference being the addition of the ^{31}P initialization phase. Figure 6.5b portrays the ^{29}Si nuclear spin flip probability P_n as a function of the pulse duration t_p , with the donor in the D^0 charge state. The data was obtained over ~ 7 hours with 10 sweeps of the Rabi pulse length t_p . We performed 20 measurements (Fig. 6.5a) at each t_p to give a total of 200 measurements per point. Figure 6.5d depicts the experimental Rabi oscillations for the ^{29}Si nuclear spin with the donor in the D^+ charge state. The ionized donor data displays higher visibility oscillations than those of the neutral donor case, due to the lack of the requirement to properly initialize the electron spin (Section 5.8).

Next we probe the coherence of the isolated (ionized donor) ^{29}Si nuclear spin by performing Ramsey fringe and Hahn echo experiments. The NMR pulse sequence and accompanying Bloch sphere state evolution are presented in Figs. 5.9a,b for the Ramsey experiment and in Figs. 5.9d,e for the Hahn echo measurement. The damped fringes of Fig. 6.6a represent the average over 5 sweeps of the

inter-pulse delay τ (taken over ~ 4 hours), with a total of 100 measurements at each point. Fitting the data with a damped cosine function of the form $P_n = P_n(0) \cos(2\pi\Delta d\tau) \exp(-\tau/T_2^*)$ yields a dephasing time of $T_2^* = 2.4(3)$ ms. Also from this fit we get Δd , the average detuning from resonance, which enables us to provide a more accurate estimate of the gyromagnetic ratio $\gamma_{\text{Si}} = 8.460(2)$ MHz/T. The echo decay curve of Fig. 6.6b is obtained from 23 sweeps of τ over ~ 28 hours, with each point presenting the average of 920 measurements. Fitting the decay with a free exponential fit $y = y(0) \exp((-2\tau/T_2)^b)$ reveals a coherence time of $T_2 = 6.3(7)$ ms and an exponent $b = 1.2(2)$. The coherence time is in excellent agreement with Hahn echo measurements in bulk [184], where decoherence is caused by the dipole interactions with other ^{29}Si nuclear spins. Accordingly, we expect to be able to significantly improve this figure by using specialized NMR pulse sequences [185] which dynamically decouple the dipole interactions – coherence times as long as 25 seconds have been demonstrated in bulk samples with these techniques [186].

6.5 Single ^{29}Si Nuclear Spin Metrology

In the late 1960’s, Hale and Mieher carried out a series of experiments [183] where they measured the anisotropic and isotropic components of the hyperfine tensor between donor electron spins and the ^{29}Si nuclear spins at surrounding lattice sites. This work was subsequently followed with a detailed theoretical analysis [139, 187–190] which was able to assign all the ^{29}Si experimental data to specific lattice sites. We can utilize this knowledge to define possible locations of the ^{29}Si atom measured here. An accurate measure of the hyperfine splitting can

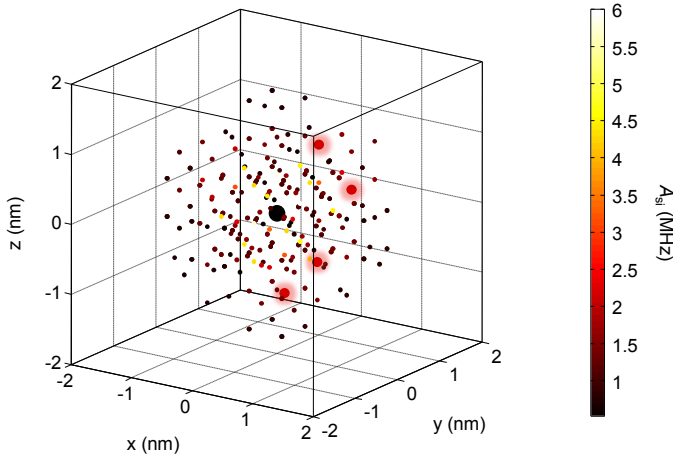


Figure 6.7: Possible lattice sites for the single ^{29}Si atom. The result of atomistic modeling to match the experimentally determined contact hyperfine constant. Plotted are the ^{29}Si nuclear spins with known hyperfine couplings [183]. The color-scale indicates the hyperfine interaction strength for each site, which is rescaled to reflect the distorted donor electron wavefunction in our nanostructure device. The lattice sites which produce contact hyperfine constants within the range 2.15 – 2.25 MHz are shown as larger circles. The author acknowledges F. A. Mohiyaddin for work on the atomistic modeling.

be found from the NMR frequencies used in the Rabi experiments $A_{\text{Si}} + D_{\text{Si}} = 2 \times (\nu_{\text{Si}2} - \nu_{\text{Si}0}) = 2.205(5)$ MHz. However, a direct comparison of this result with the bulk-doped measurements of Hale and Mieher is not possible because of the non-bulk like donor electron wavefunction. The electric fields generated by the nanostructure device distorts the wavefunction, causing a Stark shift of the hyperfine splittings.

We employ metrology techniques described in [111] to generate possible locations of the ^{29}Si atom. Using the software ISE-TCAD, a finite-element Poisson equation solver, we calculate the potential profile surrounding the donor. Following this, we calculate the wavefunction for the potential profile (including the donor Coulombic potential) by solving the full atomistic tight-binding Hamiltonian with the tool Nano Electronic MOdeling 3D (NEMO 3D). Calculating the shift from the bulk value in the probability density of the electron wavefunction

6.6. Conclusion

$|\Psi(r_0)|^2$ at each lattice site, allows us to appropriately scale the Fermi contact hyperfine splittings measured by Hale and Mieher. For simplicity we assume here that $A_{\text{Si}} \gg D_{\text{Si}}$ and our detected splitting is dominated by the contact term. This assumption is validated by the observation that the secular dipole terms in bulk satisfy this relation for all ^{29}Si lattice sites investigated [183]. Figure 6.7 provides a 3D plot of the ^{31}P donor (large black circle) and the surrounding ^{29}Si nuclei with known hyperfine constants. The terms have been scaled from bulk as described above, and the ^{29}Si nuclei with values in the range 2.15 – 2.25 MHz, which covers the splitting A_{Si} observed here, are plot as enlarged circles. We have thus been able to narrow down the location of our ^{29}Si atom to four out of a known ~ 150 possible lattice sites.

6.6 Conclusion

The results reported here further demonstrate the sensitivity of our nuclear spin detection technique. We have performed electrical QND readout on a single ^{29}Si nuclear spin, which displayed flip times of order minutes. Coherent control was obtained over the ^{29}Si nuclear spin with the donor in both the D^0 and D^+ charge states, and spin echo measurements yielded a coherence time in agreement with bulk experiments for the ionized donor. We anticipate that the single-shot QND detection of an individual host nuclear spin, along with the demonstration of coherent control, will open the door to experiments where ^{29}Si spins are utilized as a resource [61] for QIP.

Chapter 7

Conclusion and Future Work

“Theory guides. Experiment decides.”

Izaak Maurits Kolthoff

7.1 Summary of Achievements

The work carried out in this thesis presented a number of significant firsts for silicon quantum information processing. The first single-shot measurement of an individual electron spin was achieved in a silicon nanoelectronic device, made using standard CMOS fabrication processes. The device – consisting of implanted phosphorus donors tunnel-coupled to a single-electron transistor – was then employed to demonstrate the first instance of coherent control of a donor-bound electron spin qubit in silicon. An extension of the electron spin qubit experiments saw the realization of a donor-based nuclear spin qubit, where extraordinary accuracy in measurement and control delivers great promise for future fault-tolerant quantum computing. Finally, these sensitive yet powerful techniques were applied to detect and coherently operate a nearby single ^{29}Si nuclear spin, illustrating its worth as a potential resource for quantum computing.

Over half a century of bulk spin resonance experiments on Si:P has made it one of the most studied and well understood physical systems. The precise detection and manipulation of the spin states of a *single* phosphorus donor, along with the ability to measure and control the environmental nuclei, represents a milestone achievement with broad implications for silicon quantum computing.

7.2 Chapter 3 - Electron Spin Readout

A novel CMOS-compatible silicon nanoelectronic device was measured and used to read the state of an individual electron spin in a single measurement. The electron spin, which was bound to a single phosphorus donor and coupled to the island of a single electron transistor, showed remarkable properties including a

6 second long relaxation time at 1.5 T. Probing the relaxation rate $1/T_1$ at different magnetic fields unveiled a power dependence consistent with the theoretical predictions for phosphorus donors in silicon. Finally, the single-shot measurement fidelities were analyzed, which culminated in the demonstration of a 92% spin readout visibility.

7.3 Chapter 4 - Electron Spin Qubit

The spin readout device architecture of Chapter 3 was adapted for electron spin resonance experiments by including an on-chip broadband transmission line. With the ability to generate high-frequency microwave B_1 fields at the site of the donor, coherent electron spin flips (or Rabi oscillations) were observed in single-shot. A minimum $\pi/2$ gate time of ~ 75 ns was achieved, corresponding to a Rabi frequency of 3.3 MHz. Spin echo techniques were utilized to reveal the coherence time, which was found to be $\sim 200\mu\text{s}$ using a Hahn echo sequence. Dynamical decoupling was then employed to extend the T_2 to $410\mu\text{s}$ and simultaneously demonstrate control about orthogonal axes on the Bloch sphere. Simulations of the Rabi oscillations, taking into account the dominant sources of error, yielded fidelities of 77(2)% for measurement, $> 90\%$ for initialization and 57(2)% for control.

7.4 Chapter 5 - ^{31}P Nuclear Spin Qubit

By utilizing the broadband nature of the transmission line, it was possible to excite the donor with radio-frequency B_1 fields and drive rotations of the nuclear spin. A quantum non-demolition measurement of the nuclear spin state

– through ESR and projective readout of the electron spin – monitored these rotations in single-shot, with extracted readout fidelities ($> 99.8\%$) approaching those in vacuum-based ion trap systems. Ramsey fringe and Hahn echo experiments were performed to probe qubit dephasing. A T_2 of 60 ms was found with the donor ionized, a result in agreement with the expected decoherence via the ^{29}Si nuclear spin bath. The extracted coherence time for the neutral donor nuclear spin was 3.5 ms, possibly limited by electrical noise which is converted into magnetic fluctuations through the hyperfine interaction with the electron spin. Finally, specialized dynamical decoupling sequences were executed to measure the accuracy of the ionized donor nuclear spin control pulses, where a fidelity better than 98% was found.

7.5 Chapter 6 - ^{29}Si Nuclear Spin Qubit

Low-power observation of the electron spin resonance lines revealed a peak splitting, which was demonstrated to be the result of the presence of a single ^{29}Si nuclear spin. Through its hyperfine coupling with the electron spin, it was possible to monitor the state of the ^{29}Si spin by employing the readout techniques developed in Chapter 5. As with the ^{31}P nucleus, coherent control was performed with the donor in both the neutral D^0 charge state as well as the ionized D^+ charge state. A Hahn echo decay yielded a T_2 of 6.3 ms for the ionized donor, in good agreement with experiments performed on large ensembles of ^{29}Si nuclear spins. Metrology techniques were then explored to locate the ^{29}Si atom, and four possible lattice sites were discovered which could account for the experimentally observed hyperfine coupling strength.

7.6 Future Work and Outlook

In Chapter 3 of this thesis, electron spin readout experiments were performed at $B_0 \approx 5$ T, delivering measurement visibilities of up to 92%. At such a large B_0 , the condition $E_Z > 5k_B T_{\text{el}}$ is well satisfied, and T_1 is still sufficiently long (~ 100 ms) to neglect spin relaxation effects. The infidelity is due primarily to electrical detection limitations of the experimental setup – e.g. the measurement noise floor and the bandwidth of the system. In Chapter 4, measurements on a single ^{31}P donor electron spin were performed at a magnetic field of ~ 1 T, this lower value of B_0 was needed for technical reasons relating to the generation of microwave pulses for electron spin control. Here $E_Z \approx 5k_B T_{\text{el}}$, and the thermally induced readout errors – e.g. due to incorrect initialization of the electron spin, or erroneous tunneling of $|\downarrow\rangle$ electrons to the SET island during readout – caused a reduction in the fidelity. Whilst the figures reported here are promising, there is still room for improvement. The thermally-induced readout errors can be minimized by decreasing the electron temperature T_{el} , through improved electrical filtering of the gates connecting the sample to room temperature. Exploiting the CMOS compatibility of the device by fabricating on-chip current comparators could significantly widen the available detection bandwidth, reducing the electrical readout errors.

Fabricating future devices on ^{28}Si enriched substrates should see an instant improvement in electron spin control fidelities, owing to the much longer coherence times possible [83]. Parallel efforts in optimizing the device design – for example, bringing the on-chip transmission line closer to the qubit by writing it on the same side of the SET as the donor – can deliver greater B_1 driving fields. With these simple changes, I anticipate at least an order of magnitude improve-

ment in gate time to coherence ratio (t_π/T_2), and a corresponding increase in the quality of spin rotations. Together with the improvements in the readout fidelity, this would bring the electron spin qubit closer to fault-tolerant levels for quantum computing.

The ^{31}P nuclear spin qubit already demonstrates excellent readout and control capabilities, but will still benefit from the improvements made for electron spin. The lower electron temperature will increase the initialization fidelity of the nuclear spin for the neutral donor, and the ionized donor nuclear spin will see an extended coherence time by moving to an isotopically enriched substrate. An investigation will be carried out on the shorter than expected T_2 in the neutral donor case. This may involve reducing the interface trap density and/or modifying the setup to reduce electrical noise on the gates – which coincidentally would be improved through the steps to lower the electron temperature.

With improved measurement and control fidelities, it will be possible to demonstrate a solid-state single-atom quantum memory [92] and electron-nuclear entanglement [93, 172]. The insufficient fidelity of the electron spin control pulses was the factor that prevented such electron-nuclear entanglement and memory storage experiments being performed in the present setup. Coupling of two ^{31}P donor electron [70] or nuclear [68] spins should also be possible, enabling the demonstration of basic quantum algorithms.

The quest for developing a donor-based quantum computer in silicon has been ongoing for over a decade. Technical challenges involved in the readout and control of the electron and nuclear spins of a single phosphorus donor have now been resolved. The results presented here are the first for ^{31}P spin qubits in silicon, and would be considered respectable in many well-established QIP systems.

7.6. Future Work and Outlook

This technology is still in its infancy, and as such there exist many opportunities to optimize both device design and experimental infrastructure to improve performance. Whilst there still remain some very important technical challenges to overcome, namely coherent spin transport [70] and two-qubit gates, I believe that there are currently no fundamental reasons why donor-based quantum computing in silicon isn't in principle feasible.

References

- [1] Bardeen, J. and Brattain, W. H. *Physical Review* **74**(2), 230 (1948).
- [2] Dacey, G. and Ross, I. *Bell System Technical Journal* **34**(6), 1149–1189 (1955).
- [3] Kahng, D. and Atalla, M. In *IRE Device Research Conference, Pittsburg*, (1960).
- [4] Auth, C. In *Custom Integrated Circuits Conference (CICC), 2012 IEEE*, 1–6. IEEE, (2012).
- [5] Moore, G. E. In *Electron Devices Meeting, 1975 International*, volume 21, 11–13. IEEE, (1975).
- [6] Sze, S. M. and Ng, K. K. *Physics of semiconductor devices*. Wiley-interscience, (2006).
- [7] Asenov, A., Brown, A., Davies, J., Kaya, S., and Slavcheva, G. *Electron Devices, IEEE Transactions on* **50**(9), 1837–1852 (2003).
- [8] Hill, S. and Wootters, W. K. *Physical review letters* **78**(26), 5022–5025 (1997).
- [9] Lloyd, S. *Phys. Rev. A* **61**, 010301 Dec (1999).

REFERENCES

- [10] Meyer, D. A. *Phys. Rev. Lett.* **85**, 2014–2017 Aug (2000).
- [11] Lanyon, B. P., Barbieri, M., Almeida, M. P., and White, A. G. *Phys. Rev. Lett.* **101**, 200501 Nov (2008).
- [12] Shor, P. In *Foundations of Computer Science, 1994 Proceedings., 35th Annual Symposium on*, 124 –134, nov (1994).
- [13] Harrow, A. W., Hassidim, A., and Lloyd, S. *Phys. Rev. Lett.* **103**, 150502 Oct (2009).
- [14] Grover, L. K. *Phys. Rev. Lett.* **79**, 325–328 Jul (1997).
- [15] Lloyd, S. *Science* **273**(5278), 1073–1078 (1996).
- [16] Lanyon, B. P., Whitfield, J. D., Gillett, G., Goggin, M. E., Almeida, M. P., Kassal, I., Biamonte, J. D., Mohseni, M., Powell, B. J., Barbieri, M., et al. *Nature Chemistry* **2**(2), 106–111 (2010).
- [17] Raha, K., Peters, M. B., Wang, B., Yu, N., Wollacott, A. M., Westerhoff, L. M., and Jr, K. M. M. *Drug Discovery Today* **12**(1718), 725 – 731 (2007).
- [18] DiVincenzo, D. P. *Fortschr. der Phys.* **48**, 771–783 (2000).
- [19] Platzman, P. M. and Dykman, M. I. *Science* **284**(5422), 1967–1969 (1999).
- [20] Leuenberger, M. N. and Loss, D. *Nature* **410**(6830), 789–793 (2001).
- [21] Cory, D. G., Fahmy, A. F., and Havel, T. F. *Proceedings of the National Academy of Sciences* **94**(5), 1634–1639 (1997).
- [22] Monroe, C. and Kim, J. *Science* **339**(6124), 1164–1169 (2013).

REFERENCES

- [23] Monz, T., Schindler, P., Barreiro, J. T., Chwalla, M., Nigg, D., Coish, W. A., Harlander, M., Hänsel, W., Hennrich, M., and Blatt, R. *Phys. Rev. Lett.* **106**, 130506 Mar (2011).
- [24] Britton, J. W., Sawyer, B. C., Keith, A. C., Wang, C.-C. J., Freericks, J. K., Uys, H., Biercuk, M. J., and Bollinger, J. J. *Nature* **484**(7395), 489–492 (2012).
- [25] Greenland, P., Lynch, S., Van der Meer, A., Murdin, B., Pidgeon, C., Redlich, B., Vinh, N., and Aeppli, G. *Nature* **465**(7301), 1057–1061 (2010).
- [26] Culcer, D., Cywiński, L., Li, Q., Hu, X., and Das Sarma, S. *Phys. Rev. B* **82**, 155312 Oct (2010).
- [27] Clarke, J. and Wilhelm, F. K. *Nature* **453**(7198), 1031–1042 (2008).
- [28] Devoret, M. H. and Schoelkopf, R. J. *Science* **339**(6124), 1169–1174 (2013).
- [29] Nakamura, Y., Pashkin, Y. A., and Tsai, J. *Nature* **398**(6730), 786–788 (1999).
- [30] Martinis, J. M., Nam, S., Aumentado, J., and Urbina, C. *Physical review letters* **89**(11), 117901 (2002).
- [31] Chiorescu, I., Nakamura, Y., Harmans, C. J. P. M., and Mooij, J. E. *Science* **299**(5614), 1869–1871 (2003).
- [32] Vion, D., Aassime, A., Cottet, A., Joyez, P., Pothier, H., Urbina, C., Esteve, D., and Devoret, M. H. *Science* **296**(5569), 886–889 (2002).

REFERENCES

- [33] Koch, J., Yu, T. M., Gambetta, J., Houck, A. A., Schuster, D. I., Majer, J., Blais, A., Devoret, M. H., Girvin, S. M., and Schoelkopf, R. J. *Phys. Rev. A* **76**, 042319 Oct (2007).
- [34] Schoelkopf, R. and Girvin, S. *Nature* **451**, 664–669 (2008).
- [35] Majer, J., Chow, J., Gambetta, J., Koch, J., Johnson, B., Schreier, J., Frunzio, L., Schuster, D., Houck, A., Wallraff, A., et al. *Nature* **449**(7161), 443–447 (2007).
- [36] Xiang, Z.-L., Ashhab, S., You, J., and Nori, F. *arXiv preprint arXiv:1204.2137* (2012).
- [37] Shinkai, G., Hayashi, T., Ota, T., and Fujisawa, T. *Phys. Rev. Lett.* **103**, 056802 Jul (2009).
- [38] Hollenberg, L. C. L., Dzurak, A. S., Wellard, C., Hamilton, A. R., Reilly, D. J., Milburn, G. J., and Clark, R. G. *Phys. Rev. B* **69**, 113301 Mar (2004).
- [39] Dupont-Ferrier, E., Roche, B., Voisin, B., Jehl, X., Wacquez, R., Vinet, M., Sanquer, M., and De Franceschi, S. *arXiv preprint arXiv:1207.1884* (2012).
- [40] Awschalom, D. D., Bassett, L. C., Dzurak, A. S., Hu, E. L., and Petta, J. R. *Science* **339**(6124), 1174–1179 (2013).
- [41] Thalakulam, M., Simmons, C. B., Van Bael, B. J., Rosemeyer, B. M., Savage, D. E., Lagally, M. G., Friesen, M., Coppersmith, S. N., and Eriksson, M. A. *Phys. Rev. B* **84**, 045307 Jul (2011).

REFERENCES

- [42] Nadj-Perge, S., Frolov, S., Bakkers, E., and Kouwenhoven, L. *Nature* **468**(7327), 1084–1087 (2010).
- [43] Riel, B. J. *American Journal of Physics* **76**(8), 750–757 (2008).
- [44] Balasubramanian, G., Chan, I., Kolesov, R., Al-Hmoud, M., Tisler, J., Shin, C., Kim, C., Wojeik, A., Hemmer, P. R., Krueger, A., et al. *Nature* **455**(7213), 648–651 (2008).
- [45] (Online) Bhadeshia, H. K. D. H. Some Crystal Structures, *University of Cambridge*, accessed February 2013, <<http://www.msm.cam.ac.uk/phase-trans/2003/MP1.crystals/MP1.crystals.html>>.
- [46] Wolf, S. A., Awschalom, D. D., Buhrman, R. A., Daughton, J. M., von Molnr, S., Roukes, M. L., Chtchelkanova, A. Y., and Treger, D. M. *Science* **294**(5546), 1488–1495 (2001).
- [47] Hanson, R. and Awschalom, D. D. *Nature* **453**(7198), 1043–1049 (2008).
- [48] Feher, G. and Gere, E. A. *Phys. Rev.* **114**, 1245–1256 Jun (1959).
- [49] Kouwenhoven, L. P., Markus, C., McEuen, P. L., Tarucha, S., Westervelt, R. M., and Wingreen, N. S. *NATO ASI Series E Applied Sciences-Advanced Study Institute* **345**, 105–214 (1997).
- [50] Tarucha, S., Austing, D. G., Honda, T., van der Hage, R. J., and Kouwenhoven, L. P. *Phys. Rev. Lett.* **77**, 3613–3616 Oct (1996).
- [51] Loss, D. and DiVincenzo, D. P. *Phys. Rev. A* **57**, 120–126 Jan (1998).
- [52] Levy, J. *Phys. Rev. Lett.* **89**, 147902 Sep (2002).

REFERENCES

- [53] Simmons, C. B., Thalakulam, M., Shaji, N., Klein, L. J., Qin, H., Blick, R. H., Savage, D. E., Lagally, M. G., Coppersmith, S. N., and Eriksson, M. A. *Applied Physics Letters* **91**(21), 213103 (2007).
- [54] Lim, W. H., Zwanenburg, F. A., Huebl, H., Mottonen, M., Chan, K. W., Morello, A., and Dzurak, A. S. *Applied Physics Letters* **95**(24), 242102 (2009).
- [55] Maune, B., Borselli, M., Huang, B., Ladd, T., Deelman, P., Holabird, K., Kiselev, A., Alvarado-Rodriguez, I., Ross, R., Schmitz, A., et al. *Nature* **481**(7381), 344–347 (2012).
- [56] Petta, J. R., Johnson, A. C., Taylor, J. M., Laird, E. A., Yacoby, A., Lukin, M. D., Marcus, C. M., Hanson, M. P., and Gossard, A. C. *Science* **309**(5744), 2180–2184 (2005).
- [57] Koppens, F., Buizert, C., Tielrooij, K.-J., Vink, I., Nowack, K., Meunier, T., Kouwenhoven, L., and Vandersypen, L. *Nature* **442**(7104), 766–771 (2006).
- [58] Gruber, A., Drbenstedt, A., Tietz, C., Fleury, L., Wrachtrup, J., and Borczyskowski, C. v. *Science* **276**(5321), 2012–2014 (1997).
- [59] Jelezko, F., Gaebel, T., Popa, I., Gruber, A., and Wrachtrup, J. *Phys. Rev. Lett.* **92**, 076401 Feb (2004).
- [60] Jelezko, F., Gaebel, T., Popa, I., Domhan, M., Gruber, A., and Wrachtrup, J. *Phys. Rev. Lett.* **93**, 130501 Sep (2004).

REFERENCES

- [61] Robledo, L., Childress, L., Bernien, H., Hensen, B., Alkemade, P. F., and Hanson, R. *Nature* **477**(7366), 574–578 (2011).
- [62] Dolde, F., Jakobi, I., Naydenov, B., Zhao, N., Pezzagna, S., Trautmann, C., Meijer, J., Neumann, P., Jelezko, F., and Wrachtrup, J. *arXiv preprint arXiv:1212.2804* (2012).
- [63] Pezzagna, S., Naydenov, B., Jelezko, F., Wrachtrup, J., and Meijer, J. *New Journal of Physics* **12**(6), 065017 (2010).
- [64] Schwartz, J., Aloni, S., Ogletree, D. F., and Schenkel, T. *New Journal of Physics* **14**(4), 043024 (2012).
- [65] Ohno, K., Joseph Heremans, F., Bassett, L. C., Myers, B. A., Toyli, D. M., Bleszynski Jayich, A. C., Palmström, C. J., and Awschalom, D. *Applied Physics Letters* **101**(8), 082413–082413–5 (2012).
- [66] Jamieson, D. N., Yang, C., Hopf, T., Hearne, S. M., Pakes, C. I., Prawer, S., Mitic, M., Gauja, E., Andresen, S. E., Hudson, F. E., Dzurak, A. S., and Clark, R. G. *Applied Physics Letters* **86**(20), 202101 (2005).
- [67] Fuechsle, M., Miwa, J. A., Mahapatra, S., Ryu, H., Lee, S., Warschkow, O., Hollenberg, L. C., Klimeck, G., and Simmons, M. Y. *Nature Nanotechnology* **7**(4), 242–246 (2012).
- [68] Kane, B. E. *Nature* **393**(6681), 133–138 (1998).
- [69] DiVincenzo, D. P. *Nature* **393**(6681), 113–14 (1998).
- [70] Hollenberg, L. C. L., Greentree, A. D., Fowler, A. G., and Wellard, C. J. *Phys. Rev. B* **74**, 045311 Jul (2006).

- [71] Gershenfeld, N. A. and Chuang, I. L. *Science* **275**(5298), 350–356 (1997).
- [72] Klauder, J. R. and Anderson, P. W. *Phys. Rev.* **125**, 912–932 Feb (1962).
- [73] Mohammady, M. H., Morley, G. W., and Monteiro, T. S. *Phys. Rev. Lett.* **105**, 067602 Aug (2010).
- [74] Morley, G. W., Lueders, P., Mohammady, M. H., Balian, S. J., Aeppli, G., Kay, C. W. M., Witzel, W. M., Gunnar, J., and S., M. T. *Nature Materials* **12**, 103107 (2013).
- [75] Wolfowicz, G., Tyryshkin, A. M., George, R. E., Riemann, H., Abrosimov, N. V., Becker, P., Pohl, H.-J., Thewalt, M. L., Lyon, S. A., and Morton, J. J. *arXiv preprint arXiv:1301.6567* (2013).
- [76] Feher, G. *Phys. Rev.* **114**, 1219–1244 Jun (1959).
- [77] Bradbury, F. R., Tyryshkin, A. M., Sabouret, G., Bokor, J., Schenkel, T., and Lyon, S. A. *Phys. Rev. Lett.* **97**, 176404 Oct (2006).
- [78] Ashoori, R. *Nature* **379**(6564), 413–419 (1996).
- [79] Kastner, M. A. *Rev. Mod. Phys.* **64**, 849–858 Jul (1992).
- [80] Shor, P. W. *Phys. Rev. A* **52**, R2493–R2496 Oct (1995).
- [81] Preskill, J. *Proceedings of the Royal Society of London. Series A: Mathematical, Physical and Engineering Sciences* **454**(1969), 385–410 (1998).
- [82] Szkopek, T., Boykin, P. O., Fan, H., Roychowdhury, V. P., Yablonovitch, E., Simms, G., Gyure, M., and Fong, B. *Nanotechnology, IEEE Transactions on* **5**(1), 42–49 (2006).

REFERENCES

- [83] Tyryshkin, A. M., Tojo, S., Morton, J. J., Riemann, H., Abrosimov, N. V., Becker, P., Pohl, H.-J., Schenkel, T., Thewalt, M. L., Itoh, K. M., et al. *Nature Materials* (2011).
- [84] Greentree, A. D., Cole, J. H., Hamilton, A. R., and Hollenberg, L. C. L. *Phys. Rev. B* **70**, 235317 Dec (2004).
- [85] Morello, A., Escott, C. C., Huebl, H., Willems van Beveren, L. H., Hollenberg, L. C. L., Jamieson, D. N., Dzurak, A. S., and Clark, R. G. *Phys. Rev. B* **80**, 081307 Aug (2009).
- [86] Morello, A., Pla, J. J., Zwanenburg, F. A., Chan, K. W., Tan, K. Y., Huebl, H., Möttönen, M., Nugroho, C. D., Yang, C., van Donkelaar, J. A., et al. *Nature* **467**(7316), 687–691 (2010).
- [87] Pla, J. J., Tan, K. Y., Dehollain, J. P., Lim, W. H., Morton, J. J., Jamieson, D. N., Dzurak, A. S., and Morello, A. *Nature* **489**(7417), 541–545 (2012).
- [88] Kohn, W. and Luttinger, J. M. *Phys. Rev.* **98**, 915–922 May (1955).
- [89] Steger, M., Sekiguchi, T., Yang, A., Saeedi, K., Hayden, M. E., Thewalt, M. L. W., Itoh, K. M., Riemann, H., Abrosimov, N. V., Becker, P., and Pohl, H.-J. *Journal of Applied Physics* **109**(10), 102411 (2011).
- [90] Gordon, J. P. and Bowers, K. D. *Phys. Rev. Lett.* **1**, 368–370 Nov (1958).
- [91] Langer, C., Ozeri, R., Jost, J. D., Chiaverini, J., DeMarco, B., Ben-Kish, A., Blakestad, R. B., Britton, J., Hume, D. B., Itano, W. M., Leibfried, D., Reichle, R., Rosenband, T., Schaetz, T., Schmidt, P. O., and Wineland, D. J. *Phys. Rev. Lett.* **95**, 060502 Aug (2005).

REFERENCES

- [92] Morton, J. J., Tyryshkin, A. M., Brown, R. M., Shankar, S., Lovett, B. W., Ardavan, A., Schenkel, T., Haller, E. E., Ager, J. W., and Lyon, S. *Nature* **455**(7216), 1085–1088 (2008).
- [93] Simmons, S., Brown, R. M., Riemann, H., Abrosimov, N. V., Becker, P., Pohl, H.-J., Thewalt, M. L., Itoh, K. M., and Morton, J. J. *Nature* **470**(7332), 69–72 (2011).
- [94] Angus, S. J., Ferguson, A. J., Dzurak, A. S., and Clark, R. G. *Nano Letters* **7**(7), 2051–2055 (2007).
- [95] Johnson, B., McCallum, J., van Beveren, L. W., and Gauja, E. *Thin Solid Films* **518**(9), 2524 – 2527 (2010).
- [96] Bladh, K., Gunnarsson, D., Hurfeld, E., Devi, S., Kristoffersson, C., Smalander, B., Pehrson, S., Claeson, T., Delsing, P., and Taslakov, M. *Review of Scientific Instruments* **74**(3), 1323–1327 (2003).
- [97] Devoret, M. H., Schoelkopf, R. J., et al. *Nature* **406**(6799), 1039–1046 (2000).
- [98] Kouwenhoven, L. P., Austing, D. G., and Tarucha, S. *Reports on Progress in Physics* **64**(6), 701 (2001).
- [99] Hanson, R., Kouwenhoven, L. P., Petta, J. R., Tarucha, S., and Vandersypen, L. M. K. *Rev. Mod. Phys.* **79**, 1217–1265 Oct (2007).
- [100] Angus, S. J., Ferguson, A. J., Dzurak, A. S., and Clark, R. G. *Applied Physics Letters* **92**, 112103 (2008).

REFERENCES

- [101] Aassime, A., Gunnarsson, D., Bladh, K., Delsing, P., and Schoelkopf, R. *Applied physics letters* **79**(24), 4031–4033 (2001).
- [102] Dehollain, J. P., Pla, J. J., Siew, E., Tan, K. Y., Dzurak, A. S., and Morello, A. *Nanotechnology* **24**, 015202 (2013).
- [103] Mao, S.-G., Hwang, C.-T., Wu, R.-B., and Chen, C. H. *Microwave Theory and Techniques, IEEE Transactions on* **48**(1), 23–29 (2000).
- [104] Devitt, S. J., Cole, J. H., and Hollenberg, L. C. L. *Phys. Rev. A* **73**, 052317 May (2006).
- [105] Pla, J. J., Tan, K. Y., Dehollain, J. P., Lim, W. H., Morton, J. J., Zwanenburg, F. A., Jamieson, D. N., Dzurak, A. S., and Morello, A. *arXiv preprint arXiv:1302.0047* (2013).
- [106] Goswami, S., Slinker, K., Friesen, M., McGuire, L., Truitt, J., Tahan, C., Klein, L., Chu, J., Mooney, P., Van Der Weide, D. W., et al. *Nature Physics* **3**(1), 41–45 (2006).
- [107] Elzerman, J., Hanson, R., Van Beveren, L. W., Witkamp, B., Vandersypen, L., and Kouwenhoven, L. P. *Nature* **430**(6998), 431–435 (2004).
- [108] Simmons, C. B., Prance, J. R., Van Bael, B. J., Koh, T. S., Shi, Z., Savage, D. E., Lagally, M. G., Joynt, R., Friesen, M., Coppersmith, S. N., and Eriksson, M. A. *Phys. Rev. Lett.* **106**, 156804 Apr (2011).
- [109] Barthel, C., Reilly, D. J., Marcus, C. M., Hanson, M. P., and Gossard, A. C. *Phys. Rev. Lett.* **103**, 160503 Oct (2009).

REFERENCES

- [110] Hanson, R., van Beveren, L. H. W., Vink, I. T., Elzerman, J. M., Naber, W. J. M., Koppens, F. H. L., Kouwenhoven, L. P., and Vandersypen, L. M. K. *Phys. Rev. Lett.* **94**, 196802 May (2005).
- [111] Mohiyaddin, F. A., Rahman, R., Kalra, R., Klimeck, G., Hollenberg, L. C. L., Pla, J. J., Dzurak, A. S., and Morello, A. *Submitted to Nanoletters* (2013).
- [112] Huebl, H., Nugroho, C. D., Morello, A., Escott, C. C., Eriksson, M. A., Yang, C., Jamieson, D. N., Clark, R. G., and Dzurak, A. S. *Phys. Rev. B* **81**, 235318 Jun (2010).
- [113] Tan, K. Y., Chan, K. W., Mottonen, M., Morello, A., Yang, C., Donkelaar, J. v., Alves, A., Pirkkalainen, J.-M., Jamieson, D. N., Clark, R. G., and Dzurak, A. S. *Nano Letters* **10**(1), 11–15 (2010). PMID: 19950969.
- [114] Möttönen, M., Tan, K. Y., Chan, K. W., Zwanenburg, F. A., Lim, W. H., Escott, C. C., Pirkkalainen, J.-M., Morello, A., Yang, C., van Donkelaar, J. A., Alves, A. D. C., Jamieson, D. N., Hollenberg, L. C. L., and Dzurak, A. S. *Phys. Rev. B* **81**, 161304 Apr (2010).
- [115] Escott, C. C., Zwanenburg, F. A., and Morello, A. *Nanotechnology* **21**(27), 274018 (2010).
- [116] Friesen, M. and Coppersmith, S. N. *Phys. Rev. B* **81**, 115324 Mar (2010).
- [117] Hofmann, F., Heinzel, T., Wharam, D., Kotthaus, J., Böhm, G., Klein, W., Tränkle, G., and Weimann, G. *Phys. Rev. B* **51**, 13872–13875 May (1995).

REFERENCES

- [118] Lim, W. H., Yang, C. H., Zwanenburg, F. A., and Dzurak, A. S. *Nanotechnology* **22**(33), 335704 (2011).
- [119] Yang, C. H., Lim, W. H., Lai, N. S., Rossi, A., Morello, A., and Dzurak, A. S. *Phys. Rev. B* **86**, 115319 Sep (2012).
- [120] Yang, C., Rossi, A., Ruskov, R., Lai, N., Mohiyaddin, F., Lee, S., Tahan, C., Klimeck, G., Morello, A., and Dzurak, A. *arXiv preprint arXiv:1302.0983* (2013).
- [121] Hayes, R. R., Kiselev, A. A., Borselli, M. G., Bui, S. S., Croke III, E. T., Deelman, P. W., Maune, B. M., Milosavljevic, I., Moon, J.-S., Ross, R. S., et al. *arXiv preprint arXiv:0908.0173* (2009).
- [122] Xiao, M., House, M. G., and Jiang, H. W. *Phys. Rev. Lett.* **104**, 096801 Mar (2010).
- [123] Hasegawa, H. *Phys. Rev.* **118**, 1523–1534 Jun (1960).
- [124] Roth, L. M. *Phys. Rev.* **118**, 1534–1540 Jun (1960).
- [125] Tahan, C. and Joynt, R. *arXiv preprint arXiv:1301.0260* (2013).
- [126] Wilson, D. K. and Feher, G. *Phys. Rev.* **124**, 1068–1083 Nov (1961).
- [127] Tahan, C., Friesen, M., and Joynt, R. *Phys. Rev. B* **66**, 035314 Jul (2002).
- [128] Lansbergen, G., Rahman, R., Wellard, C., Woo, I., Caro, J., Collaert, N., Biesemans, S., Klimeck, G., Hollenberg, L., and Rogge, S. *Nature Physics* **4**(8), 656–661 (2008).
- [129] Mims, W. B. *Electron Paramagnetic Resonance*. Plenum, New York, (1972).

- [130] de Sousa, R. *Phys. Rev. B* **76**, 245306 Dec (2007).
- [131] Shankar, S., Tyryshkin, A. M., He, J., and Lyon, S. A. *Phys. Rev. B* **82**, 195323 Nov (2010).
- [132] Calderón, M. J., Saraiva, A., Koiller, B., and Sarma, S. D. *Journal of Applied Physics* **105**(12), 122410 (2009).
- [133] Gurrieri, T., Carroll, M., Lilly, M., and Levy, J. In *Nanotechnology, 2008. NANO '08. 8th IEEE Conference on*, 609–612, (2008).
- [134] Ladd, T., Jelezko, F., Laflamme, R., Nakamura, Y., Monroe, C., and O'Brien, J. *Nature* **464**(7285), 45–53 (2010).
- [135] Morton, J. J., McCamey, D. R., Eriksson, M. A., and Lyon, S. A. *Nature* **479**(7373), 345–353 (2011).
- [136] Xiao, M., Martin, I., Yablonovitch, E., and Jiang, H. *Nature* **430**(6998), 435–439 (2004).
- [137] Khaetskii, A. V., Loss, D., and Glazman, L. *Phys. Rev. Lett.* **88**, 186802 Apr (2002).
- [138] Assali, L. V. C., Petrilli, H. M., Capaz, R. B., Koiller, B., Hu, X., and Das Sarma, S. *Phys. Rev. B* **83**, 165301 Apr (2011).
- [139] Ivey, J. L. and Mieher, R. L. *Phys. Rev. B* **11**, 849–857 Jan (1975).
- [140] Chiba, M. and Hirai, A. *Journal of the Physical Society of Japan* **33**(3), 730–738 (1972).
- [141] Witzel, W. M. and Das Sarma, S. *Phys. Rev. B* **74**, 035322 Jul (2006).

REFERENCES

- [142] Schenkel, T., Liddle, J. A., Persaud, A., Tyryshkin, A. M., Lyon, S. A., de Sousa, R., Whaley, K. B., Bokor, J., Shangkuan, J., and Chakarov, I. *Applied Physics Letters* **88**(11), 112101 (2006).
- [143] Tyryshkin, A., Morton, J., Benjamin, S., Ardavan, A., Briggs, G., Ager, J., and Lyon, S. *Journal of Physics: Condensed Matter* **18**(21), S783 (2006).
- [144] Morello, A., Stamp, P. C. E., and Tupitsyn, I. S. *Phys. Rev. Lett.* **97**, 207206 Nov (2006).
- [145] Witzel, W. M., Carroll, M. S., Morello, A., Cywiński, L., and Das Sarma, S. *Phys. Rev. Lett.* **105**, 187602 Oct (2010).
- [146] Tyryshkin, A., Wang, Z.-H., Zhang, W., Haller, E., Ager, J., Dobrovitski, V., and Lyon, S. *arXiv preprint arXiv:1011.1903* (2010).
- [147] Barenco, A., Bennett, C. H., Cleve, R., DiVincenzo, D. P., Margolus, N., Shor, P., Sleator, T., Smolin, J. A., and Weinfurter, H. *Phys. Rev. A* **52**, 3457–3467 Nov (1995).
- [148] Schweiger, A. and Jeschke, G. *Principles of pulse electron paramagnetic resonance*. Oxford University Press on Demand, (2001).
- [149] Ager, J. W., Beeman, J. W., Hansen, W. L., Haller, E. E., Sharp, I. D., Liao, C., Yang, A., Thewalt, M. L., and Riemann, H. *Journal of The Electrochemical Society* **152**(6), G448–G451 (2005).
- [150] Knill, E. *Nature* **434**(7029), 39–44 (2005).
- [151] Myerson, A. H., Szwer, D. J., Webster, S. C., Allcock, D. T. C., Curtis,

- M. J., Imreh, G., Sherman, J. A., Stacey, D. N., Steane, A. M., and Lucas, D. M. *Phys. Rev. Lett.* **100**, 200502 May (2008).
- [152] Brown, K. R., Wilson, A. C., Colombe, Y., Ospelkaus, C., Meier, A. M., Knill, E., Leibfried, D., and Wineland, D. J. *Phys. Rev. A* **84**, 030303 Sep (2011).
- [153] Abragam, A. *The Principles of Nuclear Magnetism*. Oxford Univ. Press, Oxford, (1961).
- [154] Vincent, R., Klyatskaya, S., Ruben, M., Wernsdorfer, W., and Balestro, F. *Nature* **488**(7411), 357–360 (2012).
- [155] Vlaardingerbroek, M. T. and den Boer, J. A. *Magnetic resonance imaging: theory and practice*. Springer, Berlin, (2003).
- [156] Vandersypen, L. M., Steffen, M., Breyta, G., Yannoni, C. S., Sherwood, M. H., and Chuang, I. L. *Nature* **414**(6866), 883–887 (2001).
- [157] Becker, P., Pohl, H.-J., Riemann, H., and Abrosimov, N. *physica status solidi (a)* **207**(1), 49–66 (2010).
- [158] Steger, M., Saeedi, K., Thewalt, M. L. W., Morton, J. J. L., Riemann, H., Abrosimov, N. V., Becker, P., and Pohl, H.-J. *Science* **336**(6086), 1280–1283 (2012).
- [159] McCamey, D. R., Van Tol, J., Morley, G. W., and Boehme, C. *Science* **330**(6011), 1652–1656 (2010).
- [160] Neumann, P., Beck, J., Steiner, M., Rempp, F., Fedder, H., Hemmer, P. R., Wrachtrup, J., and Jelezko, F. *Science* **329**(5991), 542–544 (2010).

REFERENCES

- [161] Feher, G. *Phys. Rev.* **103**, 834–835 Aug (1956).
- [162] Pines, D., Bardeen, J., and Slichter, C. P. *Phys. Rev.* **106**, 489–498 May (1957).
- [163] Park, S. H., Rahman, R., Klimeck, G., and Hollenberg, L. C. L. *Phys. Rev. Lett.* **103**, 106802 Sep (2009).
- [164] Prokof'ev, N. V. and Stamp, P. C. E. *Reports on Progress in Physics* **63**(4), 669 (2000).
- [165] Morello, A. and de Jongh, L. J. *Phys. Rev. B* **76**, 184425 Nov (2007).
- [166] Dreher, L., Hoehne, F., Stutzmann, M., and Brandt, M. S. *Phys. Rev. Lett.* **108**, 027602 Jan (2012).
- [167] Rahman, R., Wellard, C. J., Bradbury, F. R., Prada, M., Cole, J. H., Klimeck, G., and Hollenberg, L. C. L. *Phys. Rev. Lett.* **99**, 036403 Jul (2007).
- [168] Biercuk, M. J., Uys, H., VanDevender, A. P., Shiga, N., Itano, W. M., and Bollinger, J. J. *Nature* **458**(7241), 996–1000 (2009).
- [169] Witzel, W. M., Carroll, M. S., Cywiński, L., and Das Sarma, S. *Phys. Rev. B* **86**, 035452 Jul (2012).
- [170] Braginsky, V. B. and Khalili, F. Y. *Rev. Mod. Phys.* **68**, 1–11 Jan (1996).
- [171] Morton, J. J. L., Tyryshkin, A. M., Ardavan, A., Porfyrakis, K., Lyon, S. A., and Briggs, G. A. D. *Phys. Rev. A* **71**, 012332 Jan (2005).

REFERENCES

- [172] Mehring, M., Mende, J., and Scherer, W. *Phys. Rev. Lett.* **90**, 153001 Apr (2003).
- [173] Taylor, J. M., Marcus, C. M., and Lukin, M. D. *Phys. Rev. Lett.* **90**, 206803 May (2003).
- [174] Rudner, M. S., Vandersypen, L. M. K., Vuletić, V., and Levitov, L. S. *Phys. Rev. Lett.* **107**, 206806 Nov (2011).
- [175] de Lange, G., van der Sar, T., Blok, M., Wang, Z.-H., Dobrovitski, V., and Hanson, R. *Scientific Reports* **2** (2012).
- [176] Takahashi, R., Kono, K., Tarucha, S., and Ono, K. *Phys. Rev. Lett.* **107**, 026602 Jul (2011).
- [177] Dutt, M. V. G., Childress, L., Jiang, L., Togan, E., Maze, J., Jelezko, F., Zibrov, A. S., Hemmer, P. R., and Lukin, M. D. *Science* **316**(5829), 1312–1316 (2007).
- [178] Ladd, T. D., Goldman, J. R., Yamaguchi, F., Yamamoto, Y., Abe, E., and Itoh, K. M. *Phys. Rev. Lett.* **89**, 017901 Jun (2002).
- [179] Itoh, K. M. *Solid State Communications* **133**(11), 747 – 752 (2005).
- [180] Kawachi, G., Graeff, C. F. O., Brandt, M. S., and Stutzmann, M. *Japanese Journal of Applied Physics* **36**(Part 1, No. 1A), 121–125 (1997).
- [181] Cappellaro, P. *Phys. Rev. A* **85**, 030301 Mar (2012).
- [182] Levitt, M. H. *Spin dynamics: basics of nuclear magnetic resonance*. Wiley, (2008).

REFERENCES

- [183] Hale, E. B. and Mieher, R. L. *Phys. Rev.* **184**, 739–750 Aug (1969).
- [184] Dementyev, A. E., Li, D., MacLean, K., and Barrett, S. E. *Phys. Rev. B* **68**, 153302 Oct (2003).
- [185] Waugh, J. S., Huber, L. M., and Haeberlen, U. *Phys. Rev. Lett.* **20**, 180–182 Jan (1968).
- [186] Ladd, T. D., Maryenko, D., Yamamoto, Y., Abe, E., and Itoh, K. M. *Phys. Rev. B* **71**, 014401 Jan (2005).
- [187] Hale, E. B. and Mieher, R. L. *Phys. Rev.* **184**, 751–759 Aug (1969).
- [188] Hale, E. B. and Mieher, R. L. *Phys. Rev. B* **3**, 1955–1965 Mar (1971).
- [189] Ivey, J. L. and Mieher, R. L. *Phys. Rev. Lett.* **29**, 176–178 Jul (1972).
- [190] Ivey, J. L. and Mieher, R. L. *Phys. Rev. B* **11**, 822–848 Jan (1975).

REFERENCES

Jarryd James Pla April 5, 2013